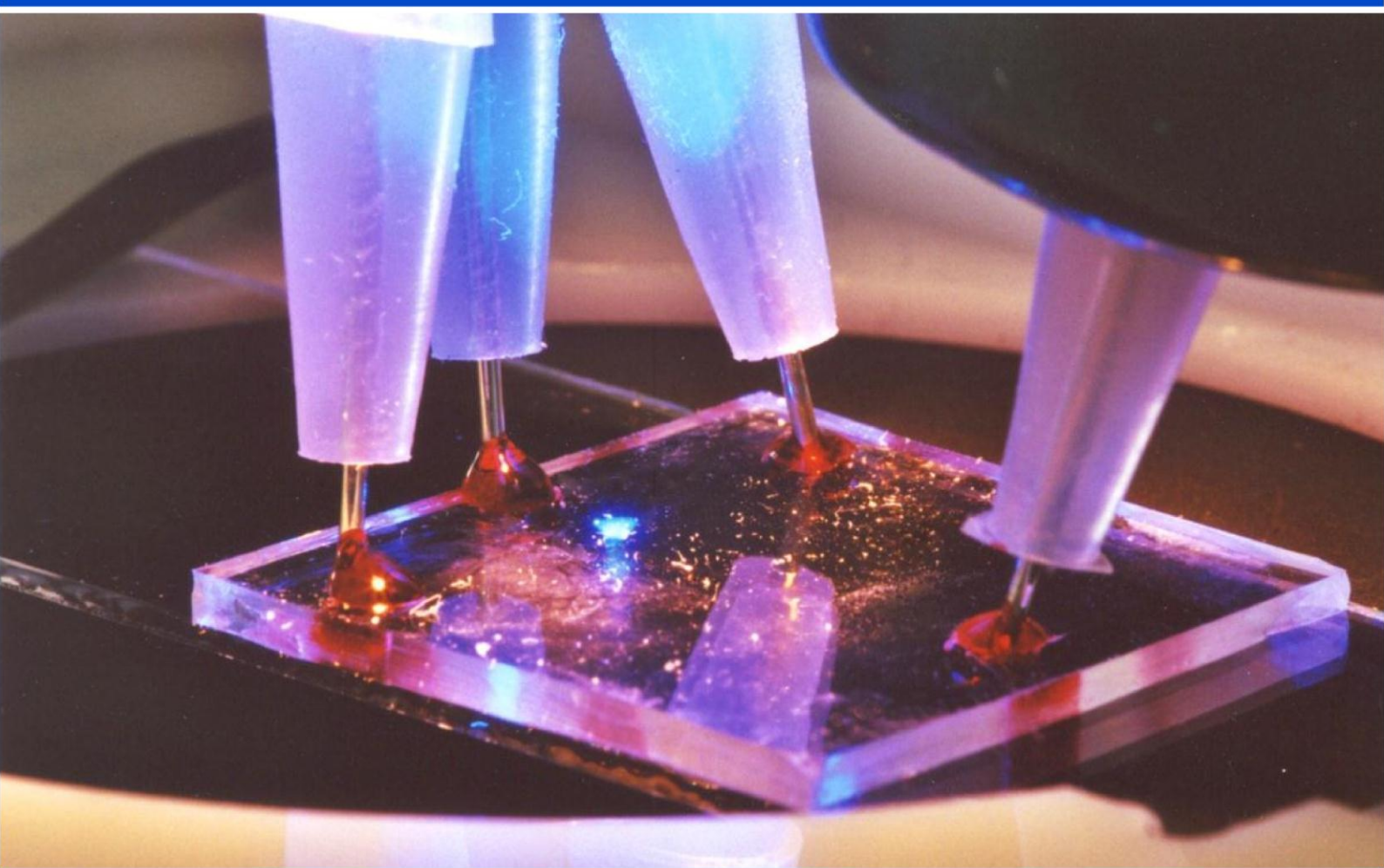


Migration and separation in structured microfluidic systems



Dissertation submitted to the Faculty of Physics
at Bielefeld University by

Lukas Bogunovic

January 2013

ERKLÄRUNG

Ich erkläre hiermit,

1. dass mir die geltende Promotionsordnung der Fakultät für Physik bekannt ist.
2. dass ich die vorliegende Dissertation selbst angefertigt, keine Textabschnitte von Dritten oder eigenen Prüfungsarbeiten ohne Kennzeichnung übernommen und alle von mir benutzten Hilfsmittel und Quellen in der Arbeit angegeben habe.
3. dass Dritte weder unmittelbar noch mittelbar geldwerte Leistungen von mir für Vermittlungstätigkeiten oder für Arbeiten erhalten haben, die im Zusammenhang mit dem Zustandekommen oder dem Inhalt der Dissertation stehen.
4. dass ich diese Dissertation oder wesentliche Teile davon nicht als Prüfungsarbeit für eine staatliche oder andere wissenschaftliche Prüfung eingereicht habe.
5. Dass ich die gleiche, eine in wesentlichen Teilen ähnliche oder eine andere Abhandlung nicht bei einer anderen Hochschule als Dissertation eingereicht habe.

Lukas Bogunovic

Eingereicht am: 17. 01. 2013

Referees

Prof. Dr. Dario Anselmetti

Experimental biophysics and applied nanoscience, Bielefeld University

Prof. Dr. Peter Reimann

Condensed matter theory, Bielefeld University

Faculty of Physics

Bielefeld University

Universitätsstraße 25

D-33501 Bielefeld

<http://www.physik.uni-bielefeld.de/>

Copyright by Lukas Bogunovic. All rights reserved. All trademarks, trade names, and company names mentioned in this work are property of their respective owners. Printed on DIN-ISO 9706 compliant paper.

PREFACE

My thesis covers the results of my work at the chair for Experimental Biophysics and Applied Nanoscience (Prof. Dario Anselmetti) at Bielefeld University. It covers three different projects: A microfluidic ratchet device for separating microparticles with freely tunable selectivity, a structured microfluidic system for the automated quantification of single molecule polarizabilities, and two different generic approaches to separate chiral microobjects only due to their asymmetry without any chiral selector. The main results of the present work have been published in the following articles. A complete list with further peer reviewed publications, conference proceedings, and manuscripts is provided in the appendix.

- J. Regtmeier, R. Eichhorn, **L. Bogunovic**, A. Ros & D. Anselmetti: *Dielectrophoretic Trapping and Polarizability of DNA: The Role of Spatial Conformation*, *Analytical Chemistry* 82 (2010), 7141-7149
- **L. Bogunovic**, D. Anselmetti & J. Regtmeier: *Photolithographic fabrication of arbitrarily shaped SU-8 microparticles without sacrificial release layers*, *Journal of Micromechanics and Microengineering* 21 (2011), 027003
- **L. Bogunovic**, R. Eichhorn, J. Regtmeier, D. Anselmetti & P. Reimann: *Particle sorting by a structured microfluidic ratchet device with tunable selectivity: Theory and Experiment*, *Soft Matter* 8 (2012), 3900-3907
- **L. Bogunovic**, M. Fliedner, R. Eichhorn, S. Wegener, D. Anselmetti, J. Regtmeier & P. Reimann: *Chiral particle separation by a nonchiral micro-lattice*, *Physical Review Letters* 109 (2012), 100603

Science is a team effort. Besides the very fruitful collaboration in Bielefeld with Prof. Peter Reimann as well as Marc Fliedner from the condensed matter theory group and especially my doctoral advisor Prof. Dario Anselmetti, I am very thankful to Prof. Ralf Eichhorn at the Nordic Institute for theoretical physics (NORDITA) at Stockholm, Sweden. The continuously improved theoretical models provided a deep understanding of the experimental facts and allowed for a much more purposive experimental approach. On the other hand, the experimental data helped to improve the theoretical model resulting in even more precise predictions and promising ideas for future experiments. Furthermore the experimental contributions of Sonja Wegener, Florian Lorenz, and Carina Vosskötter to the chiral separation project during their Bachelor theses under my practical supervision are gratefully acknowledged.

CONTENTS

1	Introduction	1
2	Fundamentals	5
2.1	Hydrodynamic effects in microfluidic systems.....	6
2.1.1	Boundary conditions	8
2.1.2	Consequences of the Navier-Stokes-equation	9
2.2	Electrodynamic effects in microfluidic systems	15
2.2.1	Electroosmosis and electrophoresis.....	17
2.2.2	Dielectrophoresis	19
2.3	Brownian motion and the coefficient of diffusion	21
2.4	Statistical mechanics	23
2.4.1	Kramers rate and diffusion in a tilted periodic potential	23
2.4.2	Ratchets and absolute negative mobility	24
2.5	Biological and chemical fundamentals.....	26
2.5.1	Chirality and stereochemistry	26
2.5.2	The DNA-molecule.....	27
3	Materials and methods	31
3.1	List of Chemicals and laboratory equipment	31
3.2	Fabrication procedures	33
3.2.1	Masterwafers	33
3.2.2	Microfluidic chips	35
3.2.3	Chiral microparticles.....	36
3.3	Sample and surface preparation	37
3.4	Experimental setup	38
3.5	Numerical prediction of chiral splitting angles.....	41

4	Results and discussion	43
4.1	Microfluidic ratchets with dynamically changeable selectivity.....	43
4.1.1	The separation concept.....	46
4.1.2	Experimental separation of three particles species	54
4.1.3	Expansion of the principle to more than 3 species	59
4.1.4	Summary.....	62
4.2	Automated quantification of single molecule polarizability	62
4.2.1	Automated analysis of single molecule DNA polarizability	65
4.2.2	Verification: polarizability vs. ionic strength	74
4.2.3	Polarizability in dependence of dye concentration.....	76
4.2.4	Summary.....	78
4.3	Enantioselective separation of microparticles	79
4.3.1	Quick release lithography.....	82
4.3.2	Chiral particle separation with a <i>non</i> -chiral array of posts	86
4.3.3	Chiral Separation with structured sidewalls.....	105
4.3.4	Comparison of the two approaches	112
4.3.5	Summary.....	114
5	Summary and outlook	115
6	References	121
7	Acknowledgements	135
	Appendix	137
A1	Construction of a microfluidic precision pump	137
A2	Sourcecodes	139
A2.1	Evaluation of mean trapping times	139
A2.2	DSP software	143
A3	Publications and conference participations.....	146
A3.1	Peer reviewed publications and manuscripts	146
A3.2	Published conference proceedings	146
A3.3	Contributions to conferences.....	147
A4	Curriculum vitae	149

1 INTRODUCTION

Bioanalytical tools¹ are key technology for the fast growing fields of modern biotechnology such as systems biology²⁻⁶, personalized medicine⁷⁻⁹, or pharmaceutical research and development^{10,11}. Today, researchers from all over the world rely on increasingly effective but also more and more complicated, sensitive and expensive analytic laboratory equipment, limiting its application in resource deprived areas or in the field¹².

Lab on a chip systems, however, are laboratory functions integrated onto a microchip and based on microfluidic technology which has been a very active field of research in the last decade. Because of their high degree of integration these systems offer several advantages over conventional laboratory equipment such as low sample and reagent consumption, portability, separation and detection with high resolution and sensitivity, low costs, or short analysis times¹³⁻²⁰.

Most analytical questions are based upon the need to determine the exact chemical or biological composition of a sample. Typically this problem is reduced to a *separation* task (e.g. via gels, electric and magnetic fields, or molecular interactions with another phase) and an ensuing *detection* of the separated compounds. The same principle usually holds in the world of microfluidics. Besides simple downscaling conventional approaches, the spatial structuring of micro- or nanochannels opens up a rich advanced toolbox for (bio-)analysis down to the single molecule scale such as dielectrophoresis²¹, entropophoresis²², entropic trapping²³, ratchets²⁴, or absolute negative mobility²⁵, just to name a few. Especially the last two effects are made possible by gainfully exploiting the omnipresent thermal motion in such small scale systems and are thus not available in macroscopic laboratory equipment or are being regarded as disturbance.

In the context of this thesis, spatially structured microfluidic channels in a state far from thermal equilibrium have been developed to address three fundamental problems in modern (bio-)analysis:

1. The usually fixed separation criterion (e.g. a gel density is not changeable on the fly)
2. The usually unknown polarizability properties of samples for dielectrophoretic manipulation
3. The requirement of a specifically designed chiral selector for chiral separation.

Project 1: Microfluidic ratchets with dynamically changeable selectivity

Typical biotechnological separation techniques like filters, chromatography, or gel electrophoresis have a fixed implemented separation criterion, e.g. defined by pore size, affinity of the steady phase, or gel density. To overcome this limit, the aim of the first project is the development and functional characterization of a microfluidic ratchet device with a dynamically changeable separation criterion. Depending on the applied voltage scheme, an arbitrarily selectable sub-group of the available species in the analyte solution is forced to migrate into opposite direction than the remaining species. Changing the voltage scheme will immediately switch the separation criterion. The device is based on a sophisticated interplay between electrophoresis and dielectrophoresis and operates with any charged and polarizable material in solution such as e.g. micro- and nanoparticles, cells, or biomolecules. The results of this project are explained in section 4.1 starting on page 43.

Project 2: Automated analysis of single molecule polarizabilities

Many microfluidic systems (such as the device from project 1) rely on dielectrophoresis to immobilize, manipulate, or sort a somehow polarizable sample. However, the actual polarizability value usually remains unknown and appropriate electric fields to trigger dielectrophoresis are found via trial and error. The second project uses dielectrophoretic traps in a tilted potential implemented in a microfluidic channel to automatically quantify single molecule (here DNA) polarizabilities via fluorescence video microscopy. The approach is tested by reproducing a well-known scaling law between the buffer solution's ionic strength and the polarizability for two different DNA types. In a second experiment the influence of the required fluorescence staining on the polarizability is investigated. Besides the pure quantification of polarizability in basic research, this system could be used to automatically tune dielectrophoretic traps in a final product to broaden its range of possible analyte classes. The results of this project are discussed in section 4.2 starting on page 62.

Project 3: Chiral separation without chiral selector

When chiral molecules are about to be separated after synthesis, a chromatography setup is used which typically requires chiral selection or derivatization agents. Usually these chemicals have to be redeveloped for every new analyte. The third project's aim is the implementation of a *generic* and *continuously* operating principle to separate chiral molecules in microfluidic channels *without* the need for any chiral selection or

derivatization agent. Two conceptually different microfluidic approaches with excellent sorting performance were developed and experimentally evaluated. Following Curie's principle²⁶, both approaches rely on microfluidic structures that somehow break the symmetry in the channel in every relevant dimension. Injected model enantiomers are demonstrated to split up according to their chirality and to accumulate near opposite channel walls. The results of this project are explained in section 4.3 starting on page 79.

Besides this first introductory chapter, the present thesis is arranged in four main chapters. Chapter 2 (page 5) recapitulates the required basic physical, chemical, and biological fundamentals for operating the developed microfluidic systems. The third chapter (page 31) discusses specifically the developed experimental methods and fabrication protocols for the investigated microdevices and summarizes the required materials and chemicals. Additionally a short description of the numerical methods, which were employed to theoretically predict the chiral separation angles is provided. The obtained experimental and theoretical results of the three main projects are considered in chapter 4 (page 43) together with a compact literature review for every part. Conclusive statements and outlooks to future projects are presented in chapter 5 (page 115). Finally, a comprehensive appendix (page 137) provides detailed overview over developed software and external control machinery as well as a list of publications, conference participations, proceedings, and the author's curriculum vitae.

2 FUNDAMENTALS

In the last decades, human kind witnessed one of the most rapid and enduring technological developments in history: integrated microelectronics²⁷, enabled by the invention of the transistor by Bardeen, Brattain and Shockley²⁸. A technology that does not only enable more powerful and less energy consuming computations on smaller machines but also revolutionized the way we live, communicate, and the way we do science. Starting from giant slow computation colossi like the first universal Turing complete electric computer ENIAC in the 1940s to modern nanoprocessors with structure dimensions of 22 nanometers, the miniaturization of electronic parts has been the key to massive performance and efficiency boosts in this field.

At the end of the 1970s the already advanced silicon fabrication technology was adapted to fabricate miniaturized mechanical systems²⁹, the so called MEMS (micro electro mechanical systems) such as pressure sensors³⁰, inkjet nozzles³¹, or gyroscopes^{32,33}. Because of their tiny size and the choice of materials, these microsystems could be integrated into existing microelectronic chips and are nowadays employed in many commercially available electronic parts.

The early stage of *microfluidics* was precluded by the first developments of micromechanical pumps, flow sensors, and actuators. This research area was essentially boosted by the work of Andreas Manz and colleagues^{34,35} with the idea of applying microfluidics as basis for so called *micro total analysis systems* to integrate a whole chemical or life science laboratory onto a microchip with integrated sample preparation, handling, and analysis in small micro- or nanometer sized channels. The benefits are analogous to a microprocessor: low sample and reagent consumption, separation and detection with high sensitivity and resolution, low costs, portability, and very short analysis times¹³⁻²⁰.

As the term *microfluidics* suggests, the central challenge in this discipline is the successful handling of smallest amounts of liquid on nano to picoliter scales. The miniaturization of channel structures leads to completely new possibilities of transport and manipulation of liquids but concurrently requires new theoretical and experimental concepts as well³⁵⁻³⁹. For example, one can easily imagine, that physical and chemical surface effects play an increasingly important role in such miniaturized channel systems, because

$$\frac{\text{surface effects}}{\text{volume effects}} \propto \frac{l^2}{l^3} = \frac{1}{l} \xrightarrow{l \rightarrow 0} \infty. \quad [2-1]$$

Furthermore, extremely laminar flows and very small heat capacities are typical features of the physics governing such environments. Properties on the molecular scale, like Brownian motion or electrodynamic interactions between particles become more and more important and can therefore not be neglected anymore as well.

This chapter outlines the underlying physical, chemical, and biological aspects required for understanding the presented experiments and their results. For actuating liquids and samples in the microchannels, an interplay between directed hydrodynamic (section 2.1) or electrodynamic (section 2.2) transport and stochastic motions induced by diffusion (section 2.3) is employed. The consequences are inter alia non-intuitive migration phenomena described in section 2.4. This includes ratchet systems, absolute negative mobility in classical single particle systems, and escape rate theories. A closer consideration of the employed biological and chemical sample classes closes this chapter (section 2.5).

2.1 HYDRODYNAMIC EFFECTS IN MICROFLUIDIC SYSTEMS

In contrast to the established discrete particle mechanics, the physics of fluids (and gases) is based on the continuum hypothesis⁴⁰. The considered fluids with density ρ are regarded as continuous objects, where an infinitesimal volume element dV is large enough, so that a reasonable number of water molecules are included but small compared to the overall Volume V . As a consequence, microscopic effects on the single water molecule level are not accounted for, justified by the micrometer sized channel geometries developed in this work.

The Euler equation

The Euler equation is a model for describing the behavior of ideal (non-viscous) fluids. The first order partial differential equation system can be derived by considering a fixed volume element dV within a streaming fluid. The force acting on its boundaries can be calculated by the divergence theorem and one obtains

$$\vec{F} = - \oint p \, d\vec{\sigma} = - \int_V \nabla p \, dV$$

where p denotes the applied hydrodynamic pressure. This is now used to devise Newton's second law

$$\rho \frac{d\vec{v}}{dt} = -\nabla p + \vec{F}_{\text{ext}}$$

where \vec{F}_{ext} is the sum of all external force densities. By properly decomposing $\frac{d\vec{v}}{dt}$ via

$$\frac{d\vec{v}}{dt} = \partial_t \vec{v} + \left(\frac{d\vec{r}}{dt} \vec{\nabla} \right) \vec{v} = \partial_t \vec{v} + (\vec{v} \vec{\nabla}) \vec{v}$$

one obtains Euler's equation⁴⁰

$$\rho(\partial_t \vec{v} + (\vec{v} \vec{\nabla}) \vec{v}) = -\nabla p + \vec{F}_{\text{ext}} \quad [2-2]$$

which is essentially the adaption of Newton's second law to hydrodynamics. However, especially in microfluidics, the previous assumption of non-viscous fluids is impossible^{36,38}. Therefore, it will now be further modified.

The Navier Stokes Equation

d'Alembert's paradox shows impressively, that assuming non-viscous and hence non-energy dissipating fluids is impossible in most system. It states for example that an obstacle in a non-viscous fluid stream is not subjected to any force. Furthermore, the Euler equation would only generate trivial results if no slip boundary conditions (see paragraph 2.1.1) are applied and energy dissipation as well as thermodynamic irreversibility would not be mathematically ascertainable.

Especially when microfluidic channels are considered, surface effects and the fluid's viscosity are very dominating factors. Hence, the Euler equation has to be further modified which will result into the *Navier Stokes equation*. It includes further additive terms to describe viscous behavior (for a derivation, see e.g.⁴⁰).

$$\rho(\partial_t \vec{v} + (\vec{v} \vec{\nabla}) \vec{v}) = -\nabla p + \eta \Delta \vec{v} + \left(\gamma + \frac{\eta}{3} \right) \nabla (\vec{\nabla} \cdot \vec{v}) + \vec{F}_{\text{ext}} \quad [2-3]$$

The values η and γ represent the *dynamic viscosity* and the so called *second viscosity*. The newly added terms $\eta \Delta \vec{v}$ and $\left(\gamma + \frac{\eta}{3} \right) \nabla (\vec{\nabla} \cdot \vec{v})$ characterize forces having their origin in the fluid's inner friction and its compression respectively. Hence, if the fluid is considered as

being incompressible (which is valid for nearly all subsonic liquids) the equation can be drastically simplified and one obtains

$$\rho(\partial_t \vec{v} + (\vec{v} \cdot \nabla) \vec{v}) = -\nabla p + \eta \Delta \vec{v} + \vec{F}_{\text{ext}}. \quad [2-4]$$

which is solvable, when considering $\nabla \cdot \vec{v} = 0$ as well.

2.1.1 BOUNDARY CONDITIONS

For solving the Navier Stokes equation in a certain region Ω , boundary conditions for the current problem have to be defined. On the macroscopic scale, the most favorite choice is the so called *no-slip boundary condition*^{38,40-42} (Figure 1.a). It essentially states, that the velocity of the fluid element next to a wall is the same as the wall piece, the element is in contact with because of friction effects, hence

$$\vec{v}(\vec{r}) = \vec{v}_{\text{wall}} \quad \text{with } \vec{r} \in \partial\Omega.$$

This term additionally implies that the surface is impermeable, and that the velocity component normal to the surfaces thus vanishes.

While this approach is mostly undoubted on the macroscopic scale, a closer consideration of microscopic boundary conditions seems important as the exact behavior of fluids at the interface can be of significant influence. The first considerations concerning the possibility of *partial slip* were made by Navier himself in 1823, when he introduced the *Navier slip length* l_S (Figure 1.b). This value represents the distance behind a wall at position $= 0$, where the no-slip condition would be reconstituted^{38,43}

$$v_x(0) = l_S \partial_z v_x(0).$$

In this case, fluid elements near the wall are decelerated but not completely stopped. For $l_S \rightarrow \infty$ the *perfect slip regime* is approached (Figure 1.c) with no wall interaction and hence no energy dissipation being observable.

Experimental results show, that choosing the correct boundary condition is delicate when considering micro- or even nanofluidic systems. Pit et al. analyzed the slip behavior of hexadecane on different surfaces via an “internal reflection–fluorescence recovery after photo bleaching” approach. They found no apparent slip on perfluorodecanetrichlorosilane

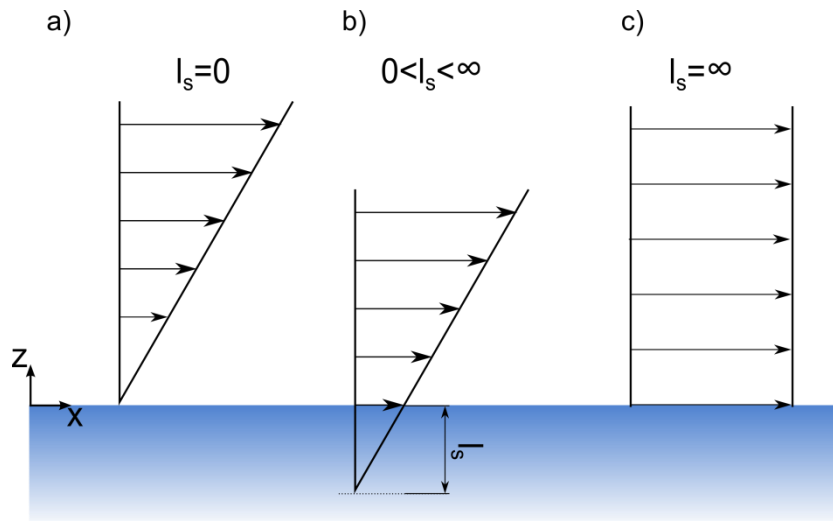


Figure 1: When a fluid is in contact with a non-permeable surface usually a) no-slip boundary conditions, b) partial slip conditions, or c) perfect slip conditions apply. The Value l_s is called *slip length*.

monolayers, $l_s = 100 \text{ nm} \pm 50 \text{ nm}$ on damaged perfluorodecanetrichlorosilane monolayers and $l_s = 400 \text{ nm} \pm 100 \text{ nm}$ on bare sapphire⁴⁴. Joseph and Tabling measured the apparent slip length at a water-glass interface in a $100\mu\text{m}$ wide and $10\mu\text{m}$ high micro channel via particle velocimetry⁴⁵. They obtained a slip length of $50 \text{ nm} \pm 50 \text{ nm}$. The results do not violate the no-slip hypothesis but give a hint that there could be an observable microscopic slip below 100 nm in such systems.

In fact, the actual value of l_s seems to be very sensitive on material properties, chemical surface properties, pressures, surface charges, dissolved gasses, fluid density gradients, surface roughness, and so on^{43,46,47}. Especially the hydrophobicity of a surface has a big influence on slip properties in pneumatically⁴³ as well as in electroosmotically⁴⁶ driven flows. In general, hydrophobic surfaces show a higher slip length than hydrophilic surfaces. With the help of the oxygen plasma chamber used for the experiments in this thesis, this property can be very well controlled^{48,49}. Hence, using no-slip conditions can be justified for the framework of this thesis, which significantly lowers the simulation complexity.

2.1.2 CONSEQUENCES OF THE NAVIER-STOKES-EQUATION

The Reynolds Number

Considering hydrodynamic problems dimensionless is often advantageous, e.g. to rapidly change scales or velocities in experiments and simulations without repeating them⁴⁰. This approach provides a set of characteristic numbers, which are equal when

hydrodynamically equivalent setups are considered. Hence, e.g. engineers can model the behaviour of large systems in smaller windtunnels and rescale their experiment afterwards to the correct order of magnitude of size, velocity, or viscosity.

Using L_0 as a typical lengthscale and v_0 as a typical velocity in the system with

$$\frac{\vec{r}}{L_0} = \vec{r}^* \quad \text{and} \quad \frac{\vec{v}}{v_0} = \vec{v}^*$$

and t_0 as typical timescale and p_0 as typical pressure in the system with

$$t = \frac{L_0}{v_0} t^* =: t_0 t^* \quad \text{and} \quad p = \frac{\eta v_0}{L_0} p^* =: p_0 p^*$$

the Navier Stokes equation for an incompressible fluid [2-4] can be transformed into

$$\begin{aligned} \rho \left(\frac{v_0}{t_0} \partial_t^* \vec{v}^* + \frac{v_0^2}{L_0} (\vec{v}^* \nabla^*) \vec{v}^* \right) &= -\frac{p_0}{L_0} \nabla^* p^* + \frac{\eta v_0}{L_0^2} \Delta^* \vec{v}^* \\ \Leftrightarrow \frac{\rho v_0 L_0}{\eta} (\partial_t^* \vec{v}^* + (\vec{v}^* \nabla^*) \vec{v}^*) &= -\nabla^* p^* + \Delta^* \vec{v}^* \end{aligned}$$

The values marked with an asterisk are dimensionless. The resulting prefactor

$$\frac{\rho v_0 L_0}{\eta} := \text{Re}$$

is one of the most important dimensionless characteristic numbers and is termed *Reynolds number*. It represents the ratio between inertial forces and viscous forces. For a typical microfluidic channel with $L_0 = 40 \mu\text{m}$ filled with water⁵⁰ ($\eta_{H_2O} = 1.00 \cdot 10^{-3} \text{ Pa s}$, $\rho_{H_2O} = 998.2 \text{ kgm}^{-3}$) with a mean flow velocity of $|\vec{v}| = 3 \cdot 10^{-5} \text{ ms}^{-1}$ the corresponding Reynolds number is in the order of

$$\text{Re} = 1.2 \cdot 10^{-3}.$$

It demonstrates that in this regime, viscous forces are clearly dominating inertial forces. In fact, inertial forces play no roll at all in such systems. The behaviour of particles inserted in such a system will only be controlled by the currently applied forces and not by any previously acting effects. This assumption implies, that the particle densities are small compared to the fluid density, which is typically the case. It furthermore means, that flows in this device will be highly laminary with no liability to turbulent behaviour⁵¹. These

findings imply many interesting effects in microfluidic systems, but often require complicated setups to accomplish supposedly easy tasks like mixing of fluids^{36,38,51–53}.

Stokes Friction

According to *Stokes' law*, an arbitrarily shaped object exposed to a streaming fluid will experience a friction force⁴⁰

$$\vec{F}_S = -\beta \vec{v}$$

where β is a proportionality constant, depending on the fluid's composition and the object's geometry. For spheres with radius r_b , like the microbeads used here, β can be calculated analytically

$$\beta = 6\pi\eta r_b.$$

Calculating β for arbitrarily shaped objects is more complex. In this general case, the equation

$$\beta = 6\pi\eta C_p$$

is employed, where C_p is mathematically equivalent to a particle's electrostatic capacitance in units where a sphere's radius equals its capacity. In general this value is easier computable as a hydrodynamic friction tensor⁵⁴.

Pneumatically actuated flows and Hagen-Poiseuille flows

If two fluid reservoirs with different filling levels (Δh) are connected via a microchannel, a pressure difference

$$\Delta p = \rho \cdot \Delta h \cdot g$$

can be measured along the channel, where g is the normal earth acceleration (see Figure 2.a). The resulting pressure difference Δp can also be generated with a pneumatic pumping system (Figure 2.b). Even when there is no external pressure applied, the system itself can generate a pressure difference, e.g. when the reservoirs have different diameters or when there are differently sized water droplets on top of the reservoirs. In this case, the curvature of the fluid surface within the reservoir leads to an internal pressure

$$p_D = \frac{2\sigma}{r_D}$$

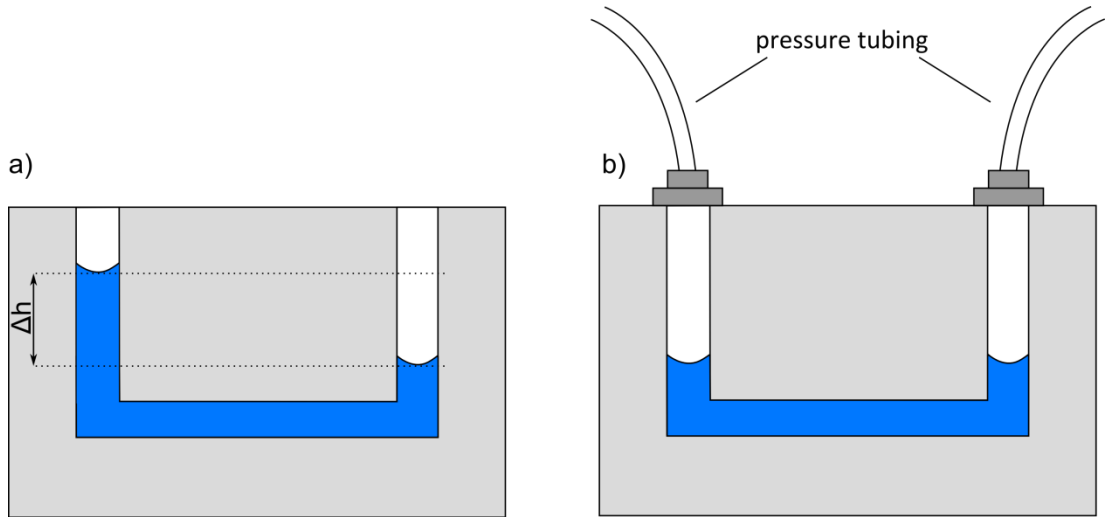


Figure 2: A fluid flow can be generated inside the depicted micro channels by a) a difference Δh in filling levels of the reservoirs or b) by introducing the pressure difference pneumatically with a pump.

where σ represents the fluid's surface tension and r_D the droplet's radius⁵⁵. Typically, p_D has more influence on a microfluidic system than Δp , e.g. $p_D = 145.5$ Pa for a droplet with $r_D = 2$ mm. It would require a 14.9 mm high water column to compensate p_D .

As a result of the pressure gradients applied to a microfluidic channel, a hydrodynamic flow is induced, trying to compensate its reason. The flow profile in the channel $\vec{v}(\vec{r})$, is usually gained by solving the Navier-Stokes equation numerically, although it is analytically solveable in very rare cases (e.g. the flow through a cylindrical tube). Here, rectangular channel geometries are considered. In this case, the explicit analytical solution is impossible, but an approximation with a Fourier-series is provided³⁸.

The considered straight and completely rigid microchannel with length L , width w and height h has a rectangular cross section (see Figure 3). Here only the non-transient solution is of interest, so the Navier-Stokes equation is simplified as follows³⁸:

$$\rho(\partial_x^2 + \partial_z^2)v_x(y, z) = -\frac{\Delta p}{\eta L} \quad [2-5]$$

in the domain $-\frac{1}{2}w < y < \frac{1}{2}w$ and $0 < z < h$. The equation shall be solved by applying no-slip boundary conditions as justified in paragraph 2.1.1 of the form $v_x(y, z) = 0$ for $y = \pm\frac{1}{2}w$ or $z = 0$ or $z = h$. Equation [2-5] is now converted into a Fourier series³⁸.

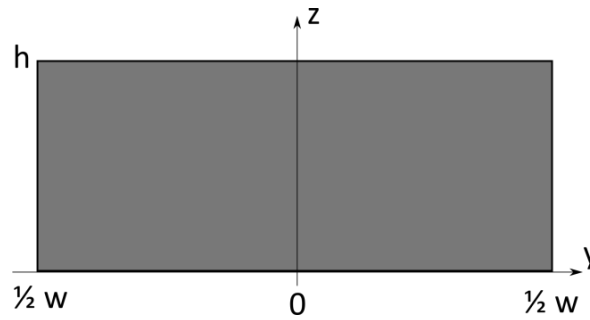


Figure 3: Sketch of the considered rectangular microfluidic channel geometry. Although this problem is highly symmetrical, the solution of the Navier-Stokes equation has to be approximated by a Fourier series.

The right hand side reads

$$-\frac{\Delta p}{\eta L} = -\frac{4 \Delta p}{\pi \eta L} \sum_{n>0, \text{odd}}^{\infty} \frac{1}{n} \sin\left(\frac{n\pi z}{h}\right) \quad [2-6]$$

where $n > 0$ and odd. Here, only terms proportional to $\sin\left(\frac{n\pi z}{h}\right)$ were considered, to maintain the requested boundary conditions. The left hand side of equation [2-5] is reformulated as follows:

$$v_x(y, z) = \sum_{n=1}^{\infty} f_n(y) \sin\left(\frac{n\pi z}{h}\right) \quad [2-7]$$

The Fourier coefficients $f_n(y)$ are a function of y and constant in z . This series is now inserted into equation [2-5]:

$$(\partial_x^2 + \partial_z^2)v_x(y, z) = \sum_{n=1}^{\infty} \left[f_n''(y) - \frac{n^2 \pi^2}{h^2} f_n(y) \right] \sin\left(\frac{n\pi z}{h}\right) \quad [2-8]$$

By equalizing equations [2-6] and [2-8] one obtains the following constraints:

$$f_n''(y) - \frac{n^2 \pi^2}{h^2} f_n(y) = -\frac{4 \Delta p}{\pi \eta L} \frac{1}{n} \quad \text{for odd } n$$

$$f_n(y) = 0 \quad \text{for even } n$$

To find the coefficients $f_n(y)$, the second order differential equation in the first constraint needs to be solved. A general approach to accomplish this is

$$f_n(y) = f_n^{\text{inhom}}(y) + f_n^{\text{hom}}(y)$$

where a particular solution can be found with the probe function $f_n^{\text{inhom}}(y) = \text{const.}$:

$$f_n^{\text{inhom}}(y) = \frac{4h^2\Delta p}{\pi^3\eta Ln^3} \quad \text{for odd } n > 0$$

On the other hand, the general solution for the homogenous part $f_n''(y) - \frac{n^2\pi^2}{h^2}f_n(y) = 0$ is the following linear combination

$$f_n^{\text{hom}} = A \cosh\left(\frac{n\pi}{h}y\right) + B \sinh\left(\frac{n\pi}{h}y\right)$$

The desired no-slip boundary condition $f_n\left(\pm\frac{1}{2}w\right) = 0$ needs to be fulfilled. Hence, the solution is

$$f_n(y) = \frac{4h^2\Delta p}{\pi^3\eta Ln^3} \left[1 - \frac{\cosh\left(\frac{n\pi}{h}y\right)}{\cosh\left(\frac{n\pi}{h}\frac{w}{2}\right)} \right] \quad \text{for odd } n$$

This result is inserted into equation [2-7] which leads to the following result for the velocity field in a micro channel with rectangular cross section under no-slip boundary conditions³⁸.

$$v_x(y, z) = \frac{4h^2\Delta p}{\pi^3\eta L} \sum_{n=1}^{\infty} \frac{1}{n^3} \left[1 - \frac{\cosh\left(\frac{n\pi}{h}y\right)}{\cosh\left(\frac{n\pi}{h}\frac{w}{2}\right)} \right] \sin\left(\frac{n\pi z}{h}\right) \quad [2-9]$$

The result $v_x(y, z)$ is plotted in Figure 4 clearly showing the parabolic characteristics of a hydrodynamic flow profile along the z axis. The maximum of v_x depends quadratically on the channel's height h , linearly on the applied pressure difference Δp and is antiproportional to the length of the channel L and the viscosity η . One of the main tasks during the experiments concerning the separation of chiral microparticles (see paragraph 4.3.3) is further modifying this flow profile to be fully asymmetric.

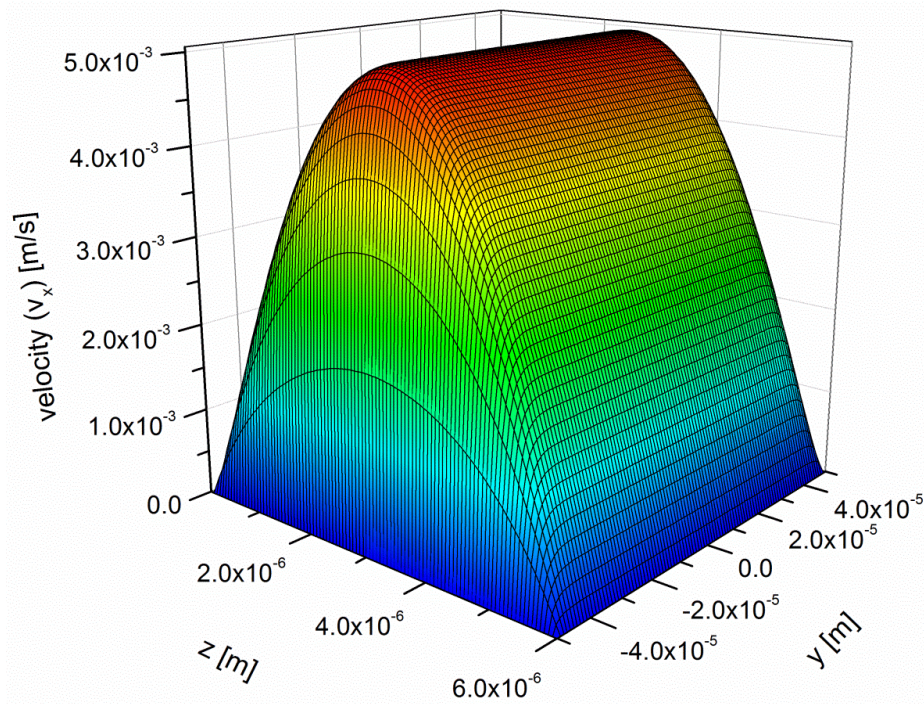


Figure 4: Flow profile in a micro channel with rectangular cross section, as calculated above by solving the non-transient Navier-Stokes equation with no slip boundary conditions via Fourier series for typical microfluidic parameters: $h = 6 \mu\text{m}$, $w = 100 \mu\text{m}$, $\eta = 0,891 \cdot 10^{-3} \text{ Pa s}$, $L = 0,01\text{m}$ und $p=10^4 \text{ Pa}$. For better visibility, the y and the z axis are scaled differently. The limit of both Fourier series was approximated using Wolfram Mathematica®. The result shows the typical parabolic Hagen-Poiseuille flow profile along the z axis.

2.2 ELECTRODYNAMIC EFFECTS IN MICROFLUIDIC SYSTEMS

When a surface is brought into contact with a polar liquid such as water, a charge transfer between the surface and the liquid takes place. The result is a deprotonation of the surface. Hence, it gets negatively charged while the electrolyte gets positively charged. However, the global charge neutrality is maintained. The result is shown in Figure 5. Because of Coulomb interaction the positive counter ions in region A (*Stern layer*) are strongly attracted by the surface and are thus immobile. On the other hand, counter ions are repelled. The electric potential $\Psi(x)$ drops linearly (*Stern potential*) starting from Ψ_0 , the surface potential to a value ζ , the so called *zeta-potential*.

Further away from the surface in region B (*Gouy-Chapman layer*), diffusion plays a more important role as the Coulomb interaction is weaker. In this regime, the potential function drops exponentially

$$\Psi(x) = \zeta \exp\left[-\frac{x}{\lambda_D}\right]$$

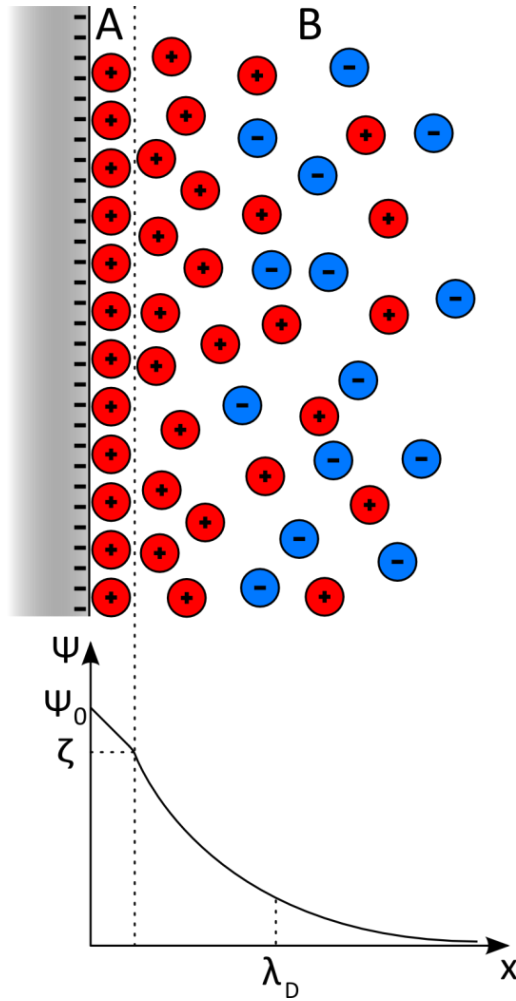


Figure 5: The ionic structure near a deprotonated surface which has been brought into contact with an electrolyte at thermal equilibrium. Because of Coulomb-interaction, an immobile layer of positive counter ions adsorbs to the negatively charged surface, the so called *Stern-Layer* (A) where the potential drops linearly. Further away from the surface, the more diffusive and mobile *Gouy-Chapman layer* (B) follows, where the potential drops exponentially, characterized by the Debye length λ_D .

where

$$\lambda_D := \sqrt{\frac{\epsilon k_B T}{2(Ze)^2 c_0}}$$

is the so called *Debye shielding distance* or more common the *Debye length*. It is a measure for the screening effectiveness of surfaces charges. The term consists of the medium's dielectric permittivity ϵ , the thermal energy $k_B T$, the valence of the ions Z , the elementary charge e and the ion concentration c_0 . Typical Debye lengths are in the order of nanometers. Both layers A and B together are called the *electric double layer*³⁹.

2.2.1 ELECTROOSMOSIS AND ELECTROPHORESIS

Aside from transporting fluids and suspended particles via pressure differences and hydrodynamic flow, the use of electrokinetically induced flow such as electrophoresis and electroosmosis is imaginable. For this to work, an electric field has to be applied along a microchannel, generated here by a general voltage protocol

$$U(t) = U_{DC} + U_{AC} \cdot \sin(\omega t). \quad [2-10]$$

where the frequency $\omega/2\pi$ is always smaller or equal than 100 Hz. The time dependent part $\vec{E}_{AC} \cdot \sin(\omega t)$ of the resulting electric field

$$\vec{E}(t) = \vec{E}_{DC} + \vec{E}_{AC} \cdot \sin(\omega t) \quad [2-11]$$

generates oscillating back and forth movements and no effective migration. It is therefore neglected in the following discussion of electroosmosis and electrophoresis and seized again to describe dielectrophoresis in paragraph 2.2.2.

In 1809, Reuss published an article describing his observation of water flowing through porous clay towards the cathode of an electric field⁵⁶. The same principle can be exploited to transport fluids through micro channels. If such a channel is filled with a neutral electrolyte, an electric double layer will be generated at the channel walls, because silanole groups included in common materials like polydimethylsiloxane will be deprotonated (see introduction to section 2.2). If a voltage is applied along the channel, the loosely bound ions in the Gouy-Chapman layer will be transported due to the electric field. Because of inner friction the remaining fluid is transported as well. This so called *electroosmotic flow* has a non-parabolic flow profile and is characterized by the following modification to the incompressible Navier-Stokes equation³⁸

$$\rho(\partial_t \vec{v} + (\vec{v} \cdot \nabla) \vec{v}) = -\nabla p + \eta \Delta \vec{v} + \rho_{el} \nabla \Psi(z). \quad [2-12]$$

Here, $\rho_{el} = \rho_{el}(\vec{r})$ is the double layer's equilibrium charge density which is assumed to be faster in equilibrium than the typical motion timescale. In the following, ideal electro osmotic flow in a channel with $h \ll w$ is assumed, hence, $\zeta = \text{const.}$, \vec{E} is homogenous, $\lambda_D \ll h$ and the flow is in steady state³⁸. The effect should be purely electroosmotic so $\nabla p = 0$ and only the equation's x-component along the channel is of interest.

$$\begin{aligned}
0 &= \eta \partial_z^2 v_x(z) - [\epsilon \partial_z^2 \Psi(z)] E_x \\
&= \partial_z^2 \left[v_x(z) - \frac{\epsilon E_x}{\eta} \Psi(z) \right]
\end{aligned}$$

Using the boundary condition $v_x(\pm \frac{h}{2})=0$, one obtains the solution

$$v_x(z) = -[\zeta - \Psi(z)] \frac{\epsilon E_x}{\eta}.$$

$\Psi(z)$ vanishes very quickly because $\lambda_D \ll h$ is claimed. Hence, the electro osmotic flow for $\nabla p = 0$ for an electric field applied along the channel in x direction can be calculated by³⁸

$$\begin{aligned}
v_{\text{EOF}} = v_x(z) &= -\frac{\epsilon \zeta}{\eta} E_x \\
&= \mu_{\text{EOF}} \cdot E_x
\end{aligned} \tag{2-13}$$

which is the *Helmholtz-Smoluchowski* equation³⁹. The prefactor $\mu_{\text{EOF}} = -\epsilon \zeta / \eta$ is called *electrophoretic mobility* and is in particular independent of the electric field.

By changing the reference system, a second electromigration mechanism can be identified, known as *electrophoresis*. When a charged particle is immersed into an electrolyte, an electric double layer with a certain constant surface potential $\bar{\zeta}$ will arise as well on the particle surface. When a voltage is applied along the channel, the result is a moving charged surface in a resting fluid. It can be described with the same formalism as above except for a changed presign

$$\begin{aligned}
v_{\text{EP}} &= +\frac{\epsilon \bar{\zeta}}{\eta} E_x \\
&= \mu_{\text{EP}} \cdot E_x
\end{aligned} \tag{2-14}$$

which is independent on the particle's shape, as long as the Debye length is much smaller than the particle diameter and the surface potential is constant.

In many experimentally relevant conditions (steady electric field, uniform fluid with uniform electric properties, constant surface potentials everywhere in the device and Debye lengths much smaller than relevant channel/particle features) v_{EOF} is proportional to the electric field with a locally constant proportionality factor⁵⁷. The constraints mentioned above are

well justified for the experimental environments described in chapter 4. The electric field is steady because it is applied to the channels' ends and varies only in irrelevant temporal orders of magnitude in relation to the effects described above. The devices itself and the particles are fabricated out of a homogenous material, so that ζ and $\bar{\zeta}$ are constant everywhere and λ_D is typically in the order of some nanometers for the given experimental conditions. Hence, it is three orders of magnitude smaller than the smallest channel feature.

As a consequence, electro osmotic flow and electrophoresis can be fused to a single effective force. Combining equations [2-13] and [2-14] leads to the effective particle motion under ideal conditions

$$\vec{v} = \frac{\epsilon(\bar{\zeta} - \zeta)}{\eta} \vec{E}.$$

2.2.2 DIELECTROPHORESIS

The term dielectrophoresis was first defined by Pohl in the 1950s and refers to the motion of a polarizable but effectively uncharged object in an inhomogeneous electric field due to polarization effects⁵⁸. For a particle with polarizability $\alpha_p = \alpha_p(\omega)$ this dielectrophoretic force can be calculated with^{21,59,60}

$$\vec{F}_{\text{DEP}} = \alpha_p (\vec{E} \cdot \nabla) \vec{E}. \quad [2-15]$$

This equation especially expresses the impact of the electric field \vec{E} on the effectively induced dipole moment $\vec{p}_{\text{ind}} = \alpha_p \vec{E}$. Generally, the polarizability α_p is a complex tensor which depends on the applied frequency of the electric field because of dielectric losses. However, in this case, the employed frequencies are chosen below 100 Hz which is, compared to the rearrangement speed of the involved charges very low. Additionally the considered particles are assumed to be spherical without internal structure. This justifies α_p being a real valued scalar and thus independent of ω . The frequency regime, where this assumption is not possible anymore depends on the system's dielectric and geometric properties and lies typically in the order of 10-100 kHz^{61,62}.

However, as demonstrated in the previous paragraph, the polarizability is not a pure particle property but a complex interplay of the bulk material and the surrounding double

layer⁶³. It is well documented that α_p depends e.g. on the ionic strengths and composition of the surrounding solution regarding flow behavior, its pH, or its viscosity^{64–70}.

It is possible to estimate the order or magnitude of α_p by disregarding all the complex effects just mentioned and focusing on a conductive dielectric spherical particle in a conductive dielectric medium. In this case, the effective dipole moment $\alpha_p \vec{E}$ generates a dipole field similar to a point dipole around the particle⁷¹. For low frequencies, conductive effects dominate polarization effects⁶³. If the frequency is increased, conductive and dielectric impact may be witnessed and α_p becomes a frequency dependent function and can be calculated with^{63,71}

$$\alpha_p = 4\pi\epsilon r_b^3 \frac{\chi_p - \chi}{\chi_p + 2\chi} \quad [2-16]$$

for spherical microbeads with radius r_b and conductivity χ_p in a medium with conductivity χ . In most experiments, the particles are non-conducting. Hence, $\chi_p = 0$, resulting in

$$\alpha_p = -2\pi\epsilon r_b^3 \quad [2-17]$$

If the frequency is further increased, the conductivities of particles and fluids are dominated by the contributions of dielectric effects. Hence, equation [2-16] needs to be replaced by

$$\alpha_p = 4\pi\epsilon r_b^3 \frac{\epsilon_p - \epsilon}{\epsilon_p + 2\epsilon} \quad [2-18]$$

where ϵ_p and ϵ are the dielectric permittivity of the particles and of the medium respectively.

The dielectrophoretic force, calculated in equation [2-15] directly corresponds to a dielectrophoretic potential energy

$$\Psi_{\text{DEP}} = -\frac{1}{2} \alpha_p \vec{E}^2 \quad [2-19]$$

or rather with equation [2-11]

$$\Psi_{\text{DEP}} = -\frac{1}{2}\alpha_p \left(\vec{E}_{\text{DC}}^2 + \frac{\vec{E}_{\text{AC}}^2}{2} \right) \quad [2-20]$$

where the factor $\frac{1}{2}$ originates from time averaging \vec{E}_{AC}^2 and where an electrostatic assumption was made. When \vec{E} is inhomogeneous, particles are attracted by regions with high electric field strength ($\alpha > 0$, positive DEP) or low electric field strengths ($\alpha < 0$, negative DEP). The electric field enters quadratically in equations [2-19] and [2-20], in other words, dielectrophoretic effects are observed for both DC and AC voltages unlike electrophoresis or electroosmosis. Consequently, a voltage protocol like [2-10] with $U_{\text{AC}} \gg U_{\text{DC}}$ can be used to specifically address electrophoresis/electroosmosis via U_{DC} on one hand and particle trapping with dielectrophoresis via U_{AC} on the other hand as exploited in sections 4.1 and 4.2.

2.3 BROWNIAN MOTION AND THE COEFFICIENT OF DIFFUSION

In 1828, Robert Brown, a Scottish botanist was engaged in the investigation of the reproduction mechanisms of plants^{72,73}. When he observed micrometer sized particles from the pollen of *Clarkia pulchella* with his microscope, he witnessed an irregular random motion of those objects in a fluid droplet. At first, he thought that the motion resulted from the fact, that he investigated living material. However, in the same publication it was described, that it was observed with fossil particles and even with inorganic minerals as well. Roughly 100 years later, Einstein⁷⁴ and Smoluchowski⁷⁵ refocused on the problem and showed that Brownian motion is a deep physical principle based on the molecular theory of heat⁷⁴. It was derived, that a particle ensemble with density $\rho_P = \rho_P(x, t)$ located at a certain point x at time $t = 0$ diffuses according to the diffusion equation

$$\partial_t \rho_P = D \partial_x^2 \rho_P$$

where D is the *diffusion coefficient* given by the *Einstein-Smoluchowski equation*

$$D = \frac{k_b T}{\beta}.$$

Here β represents the friction coefficient of the particle in the medium. For Stokes friction (see section 2.1.2) the result is the Stokes-Einstein equation

$$D = \frac{k_B T}{6\pi\eta r_b}. \quad [2-21]$$

For a given Brownian trajectory in a two-dimensional space typically considered here, D can be explicitly calculated via

$$D = \lim_{t \rightarrow \infty} \frac{\langle \vec{r}^2(t) \rangle - \langle \vec{r}(t) \rangle^2}{4t}, \quad [2-22]$$

as well and the radius of the observed particle is thus accessible quite precisely. Here \vec{r} is the particle's position and the symbol $\langle \cdot \rangle$ denotes averages over many realizations.

The relation between directed transport and diffusional motion is characterized by the *Péclet number*⁷⁶. This dimensionless quantity is obtained by multiplying the Reynolds number Re (see paragraph 2.1.2) with the *Schmidt number* $Sc = \eta/\rho D$ and thus reads

$$Pe = \frac{v_0 L_0}{D}.$$

Consequently, when e.g. a studied microfluidic system is reduced in size, the rise of diffusion may be compensated by increasing the driving velocity accordingly.

Concerning applications in micro- and nanofluidic devices, the thermal energy at room temperature $k_B T \approx 4\mu\text{m fN} = 4\text{nm pN}$ plays a non-negligible role e.g. when collecting microbeads in dielectrophoretic traps which are usually of comparable order of magnitude. Hence, the thermal fluctuations are usually modeled by introducing a force term into a Langevin equation⁷⁷

$$\vec{F}_D(t) = \beta\sqrt{2D}\vec{\xi}(t).$$

The value $\vec{\xi}(t) = (\xi_x(t) \cdot \vec{e}_x, \xi_y(t) \cdot \vec{e}_y, \xi_z(t) \cdot \vec{e}_z)$ represents the energy input from the surrounding thermal heat bath and consists of three uncorrelated, independent, and Gaussian distributed white noise functions with zero average $\langle \xi_i(t) \rangle = 0$ and the correlation function $\langle \xi_i(s)\xi_j(t) \rangle = \delta_{ij} \delta(t - s)$.

2.4 STATISTICAL MECHANICS

2.4.1 KRAMERS RATE AND DIFFUSION IN A TILTED PERIODIC POTENTIAL

In 1940, Kramers published a theoretical model to describe chemical reactions that require activation energy⁷⁸. He considered a piecewise harmonic metastable potential $\Psi_K(x)$ (Figure 6) and a point particle subjected to Brownian motion therein. The potential function exhibits a potential minimum around x_0 and a potential barrier around x_B with height $\Delta\Psi_K$ which is larger but of comparable order of magnitude than the thermal energy $k_B T$ to obtain well defined states. The piecewise harmonic function is described by

$$\Psi_K(x) - \Psi_K(x_0) = \begin{cases} 1/2 \Omega_0^2 (x - x_0)^2 & \text{near } x = x_0 \\ \Delta\Psi_K - 1/2 \Omega_B^2 (x - x_B)^2 & \text{near } x = x_B \end{cases}$$

where Ω_0 and Ω_B are the potential curvatures at x_0 and x_B respectively⁷⁹. When $\Delta\Psi_K$ is much larger than the thermal energy $k_B T$, a particle located at the metastable potential minimum around x_0 will stay there for a certain time, until it receives a (stochastic) thermal kick providing enough energy for passing the barrier.

This resulting particle flux out of the potential well can be described with the so called *Kramers rate*⁷⁸⁻⁸⁰

$$R_K = \frac{|\Omega_0 \Omega_B|}{2\pi\beta} \exp\left(-\frac{\Delta\Psi_K}{k_B T}\right). \quad [2-23]$$

From this value, it is possible to estimate the *mean first passage time* τ_K , describing the average time interval (over many realizations) after which a single particle located at x_0 at time $t = 0$ escapes out of the potential well due to thermal noise. It can generally be calculated using the inverse Kramers rate⁸¹

$$\tau_K = \frac{1}{R_K} = \frac{2\pi\beta}{|\Omega_0 \Omega_B|} \exp\left(\frac{\Delta\Psi_K}{k_B T}\right) = C_K \exp\left(\frac{\Delta\Psi_K}{k_B T}\right).$$

Kramers' initial intention was the identification of a model system to describe thermally initiated chemical reactions. However, the model can also be directly applied to obtain mean first passage times of a polarizable particle in a local dielectrophoretic potential minimum in combination with a tilting of the potential by a static external force^{81,82}.

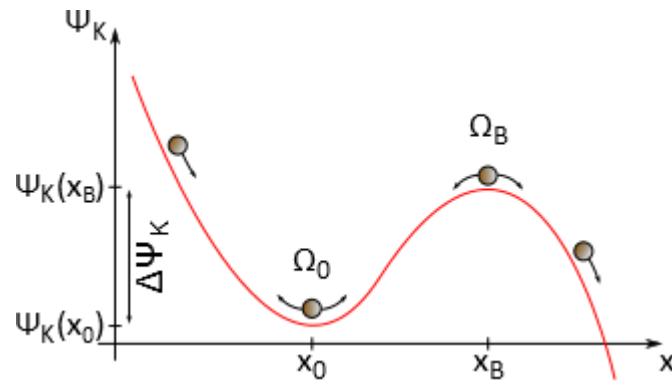


Figure 6: A metastable piecewise harmonic potential where the Kramers rate can be used to describe thermal escape processes.

2.4.2 RATCHETS AND ABSOLUTE NEGATIVE MOBILITY

When a classical system of resting Newtonian particles e.g. suspended in a liquid is not subjected to any external force, Newton's second law states, that there is no acceleration of particles and thus the overall particle speed remains zero. When an external force is applied, it is usually the case, that the particles are transported into the direction of that force and the higher the force, the faster the resulting migration velocity (Figure 7 a).

However, in spatially periodic environments with a nonlinear driving far from thermal equilibrium two other counterintuitive transportation modes can be observed experimentally and theoretically for microscopic classical particles namely a *ratchet response* (Figure 7 b)^{24,83–97} and the so called *absolute negative mobility* (Figure 7 c)^{98–104}.

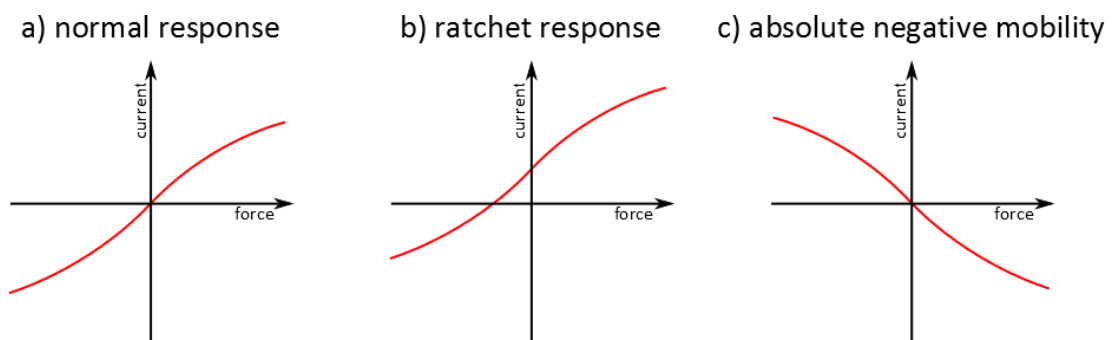


Figure 7: When a particle is subjected to an external force, e.g. hydrodynamic flow (section 2.1) or electrokinetic driving (section 2.2) one would expect, that the direction of that force \vec{F}_p and the resulting speed of the particle \vec{v}_p point into the same direction (a). If a ratchet response (b) is observed, there is effective particle transport although the mean force is zero. It is even possible to steer the particle stream effectively *against* the not too large effective force (c), an effect termed *absolute negative mobility*. In spatially structured systems with nonlinear driving and far from thermal equilibrium, these two effects are in agreement with Newton's second law and the second law of thermodynamics.

In contrast to the usual behavior, *ratchet systems* involve some kind of asymmetry in their structure so that useful work is extracted, although the mean applied force over time is zero (Figure 7 b). A macroscopic example of such a system is the clamping element of a lashing strap. Here an asymmetrically shaped cogwheel is rotated into one direction only by moving a lever back and forth. Thus, the attached webbing is coiled although no effective force into one direction was applied when averaging over time. Implementing such a device on the microscopic scale is a little more complex because now Brownian motion plays a non-negligible role. At first sight, one could think that thermal fluctuations moving the lever randomly with no mean force direction would lead to an extraction of work out of one thermal heat bath and the system would thus be a valid second kind perpetual motion machine. However, this is forbidden by the second law of thermodynamics. In reality, the lever would be moved by the ongoing bombardment of the gas atoms, but the cogwheel would be diffusing as well. As a consequence, no directed motion is extractable. However, the second law of thermodynamics is only applicable to systems in thermodynamic equilibrium. A solution would thus be to move the system away from equilibrium by e.g. introducing temperature gradients or applying strong periodic forces averaging out to zero. Following this approach several work groups proved, that indeed ratchet systems are theoretically and experimentally realizable on the microscopic scale^{86–97,105–119}.

Although the particle current is zero for vanishing driving forces as intuitively expected in systems with *absolute negative mobility*, their behavior is even more counter intuitive when switching on not too strong effective forces. The negative slope in Figure 7 c indicates that particles will move in *opposite* direction and thus *against* the effective force. In contrast to a ratchet system, such absolute negative behavior occurs in periodically *symmetric* structures⁹⁸ with nonlinear driving to overcome Newton's second law¹²⁰. The effect has been studied for several decades now in systems like semiconductors, photovoltaics, and special Josephson contacts (see²⁵ and references therein). However, the observed effects are entirely of quantum mechanical nature and a comparable observation in the classical but still microscopic dimension was not expected. More recent studies showed that even classical systems are able to exhibit absolute negative mobility but only as collective phenomenon. Very recently theoretical⁹⁸ and experimental¹²⁰ evidence was presented that absolute negative mobility is possible on the single microscopic particle scale.

2.5 BIOLOGICAL AND CHEMICAL FUNDAMENTALS

2.5.1 CHIRALITY AND STEREOCHEMISTRY

When Napoleon's soldiers went into war, their field pack contained only one single replacement boot¹²¹. The question whether this boot would fit to the left or to the right foot directly leads to the aspect of *chirality* (greek χείρ: hand). It means, that an object (like our feet or hands) is not superimposable onto its mirror image (see Figure 8)¹²². The term *chirality* has been popularized by Lord Kelvin in his famous Baltimore lectures¹²³. Chirality is a fundamental principle in nature and can be observed in every order of magnitude: From galaxies^{124,125} to human and animal anatomy^{126–128} down to molecules^{129–134} and even in nuclear and particle physics^{135,136}.

One example of chiral organic molecules are amino acids (Figure 8). In both depicted representations, four groups are connected to a central carbon atom (the so called *stereocenter*¹²⁹) in a way, that the two resulting structures cannot be transformed into each other without mirroring. However, both sum formulae and most physical parameters are identical¹³⁰. Such representations of a chiral molecule are called enantiomers¹²⁹. According to the frequently used Cahn-Ingold-Prelog-convention^{137,138} enantiomers are described using the prefix R (lat. rectus: right) and S (lat. sinister: left) and the corresponding molecule's name.

A clean sample of only one enantiomer is commonly called *optically active*, because the chiral molecules rotate the plane of linearly polarized light upon transmission through the sample. From the direction of rotation, one can infer the type of enantiomer. Chemicals resulting into positive direction are being assigned the prefix *Dex-*, because they behave like naturally available dextrose, and chemicals resulting into negative rotation are given the prefix *Lev-* because they behave like natural levulose¹³². A mixture of both enantiomers is called *racemate*¹³⁰. Because the effects of positive as well as negative rotation cancel each other out, a racemate is not optically active, as long as both chiral forms are equally concentrated in the mixture.

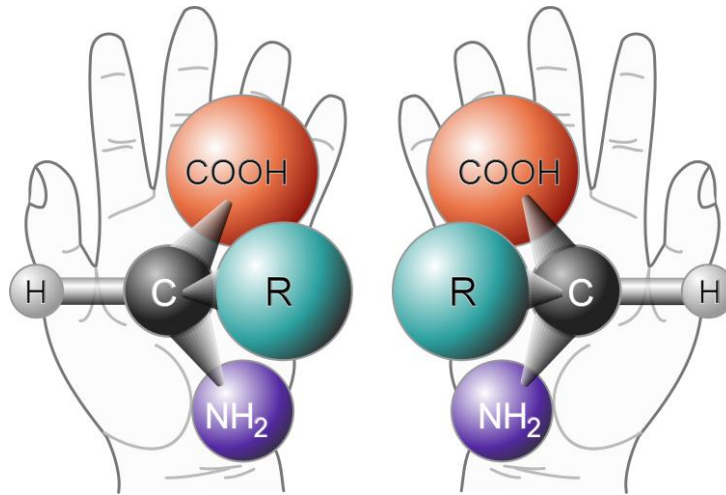


Figure 8: The concept of chirality using the example of our hands and an amino acid prototype. These mirrored images are not superimposable onto each other. Taken with permission from the National Aeronautics and Space Administration (NASA).

2.5.2 THE DNA-MOLECULE

In the winter of 1868/69, Friedrich Miescher, a young swiss scientist discovered a substance produced by lymphocytes in pus samples. Because of its origin, the cell's nuclei, he called it *nuclein* although he was unaware of the exact chemical composition¹³⁹.

Today, we know that the *deoxyribonucleic acid* (DNA) carries the genetic information of living organisms and it is thus of high interest for biotechnological and medical research and development¹⁴⁰⁻¹⁴². It is a filamentary polymer with 2nm diameter and variable length. The basic building blocks that make up the DNA polymer are called *deoxyribonucleotides* (abbr. *nucleotides*) whose sequence encodes the genetic information of an individual. Every nucleotide consists of three components: a nitrogenous base, a 2-deoxyribose molecule, and a phosphate group (Figure 9). The deoxyribose and the phosphate group are common in all nucleotides and form the DNA's backbone via phosphodiester bonds. The only difference between the nucleotides is the choice of the nucleobase attached to the ribose's 1' end, where purine, (adenine and guanine) and pyrimidine (thymine and cytosine) derivatives occur. Each of these four bases can form hydrogen bonds only with a specific partner, namely A-T and G-C or vice versa (Figure 10).

To form a polymer, the desoxyribose molecules are serially attached to each other by binding the phosphate group to the 3' hydroxylgroup of a deoxyribose and to the 5' hydroxylgroup of the next deoxyribose. Hence, one negative charge per phosphate group is

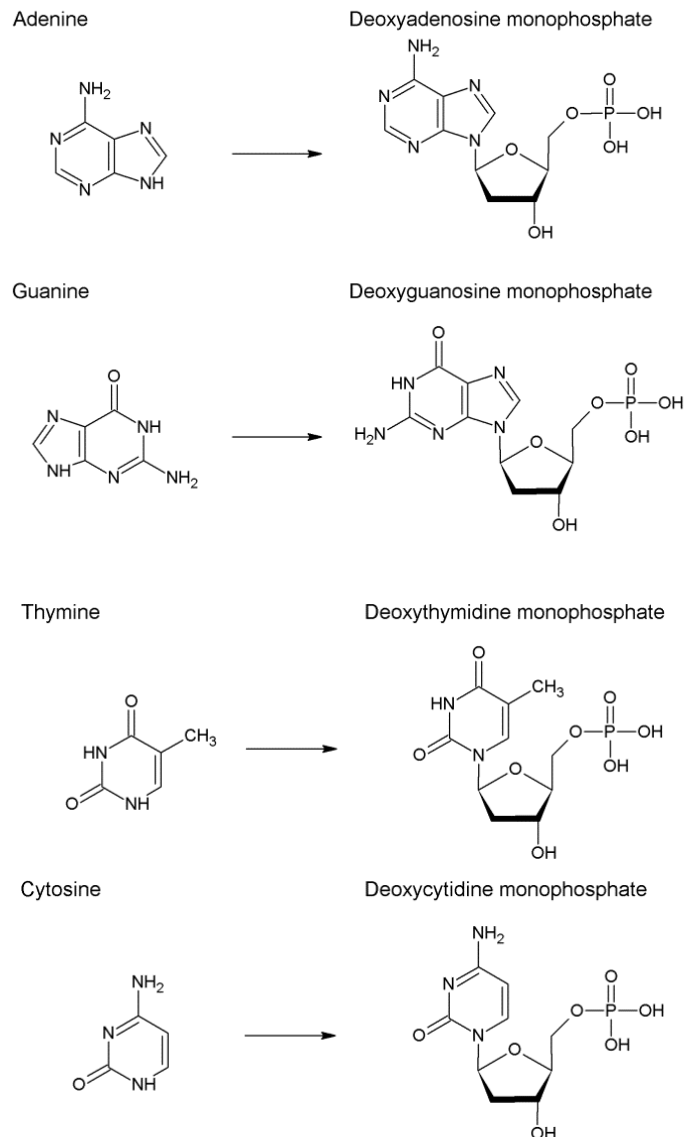


Figure 9: Four basic building blocks, the nucleotides, make up a DNA molecule. They consist of one out of four nucleobases (adenine (A), thymine (T), guanine (G) and cytosine (C)) which are attached with their 1' (for purins) or 9' (for pyrimidines) nitrogen atom to the 1' carbon atom of a deoxyribose molecule which is then bound to a phosphate. The phosphate group is later used to link the nucleotides together and provides the negative charge of the DNA backbone.

produced. To obtain a double stranded DNA molecule, a second nucleotide chain with complementary bases is attached via hydrogen bonds. This complementary arrangement of bases results in the formation of the famous right handed double helix with a diameter between 2.0 nm¹⁴³ up to 2.6 nm in free solution¹⁴⁴ where the two complementary nucleotide chains are wound around each other (roughly one turn every 10 basepairs¹⁴⁵). Hence, the hydrophobic nucleobases are directed towards the center of the helix and the

hydrophilic backbone is located outwards and subsequently screened by positive ions in the surrounding solution (Figure 11). The two nucleotide strands are not enlaced around each other completely uniformly. Because of geometric reasons, so called *minor grooves* and *major grooves* occur^{143,145} with the size relation 7:4 resulting in a length of 2.2 nm and 1.2 nm respectively.

Because living organisms are highly complex systems, the corresponding DNA often contains millions or even billions of basepairs to encode their genetic properties. The human genome for example consists of 2.9 billion basepairs¹⁴⁶ which results in a total length in the order of meters (stored separately in 46 differently sized chromosomes). This value results from the mean distance of 0.34 nm between two basepairs^{147,148}. Compared to binary data this is equivalent to the storage capacity of a compact disc with roughly 700 megabytes because the four possible degrees of freedom for each basepair need to be described by 2 bits.

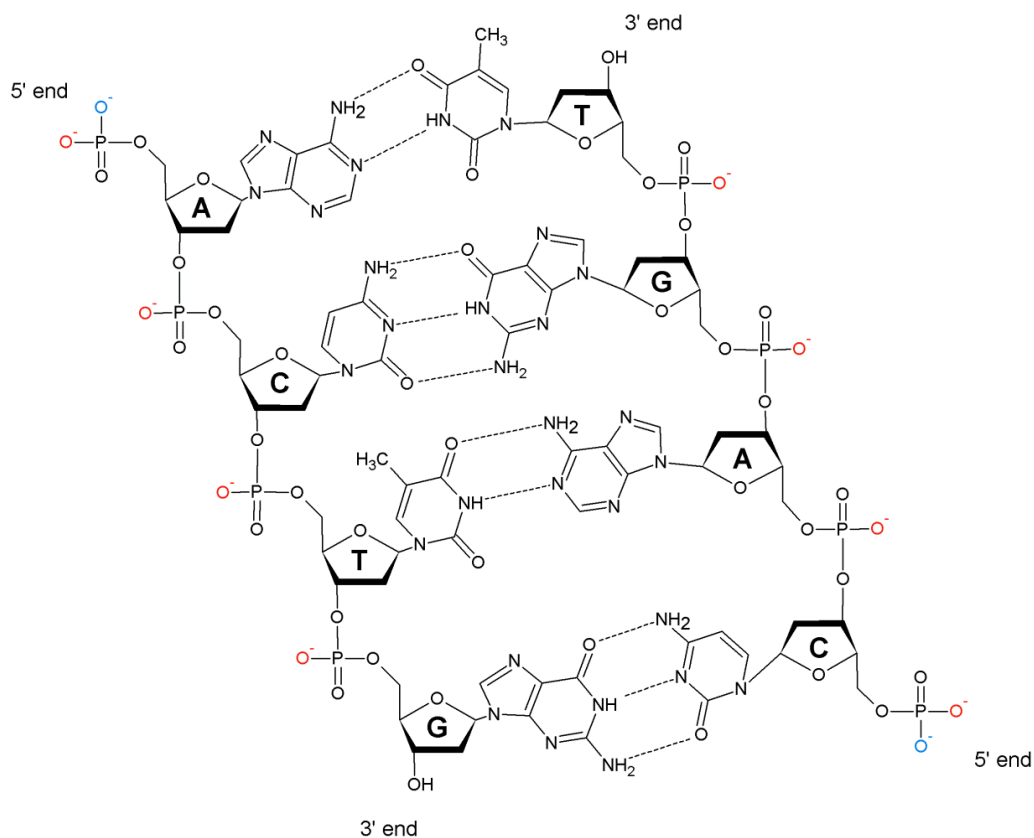


Figure 10: A short sequence (ACTG) of a double stranded DNA molecule. Two nucleotides are attached to each other with a phosphodiester bond where the 3' hydroxyl group of a deoxyribose is connected via a phosphate group to the 5' hydroxyl group of the next deoxyribose. Hence, the DNA's backbone is a negatively charged (red markers). On the opposite site, complementary nucleotides are arranged and hydrogen bonds are formed between two opposite bases. These bonds can only be effectively formed, when adenine and thymine or guanine and cytosine are opposed to each other. Hence, information is stored redundantly.

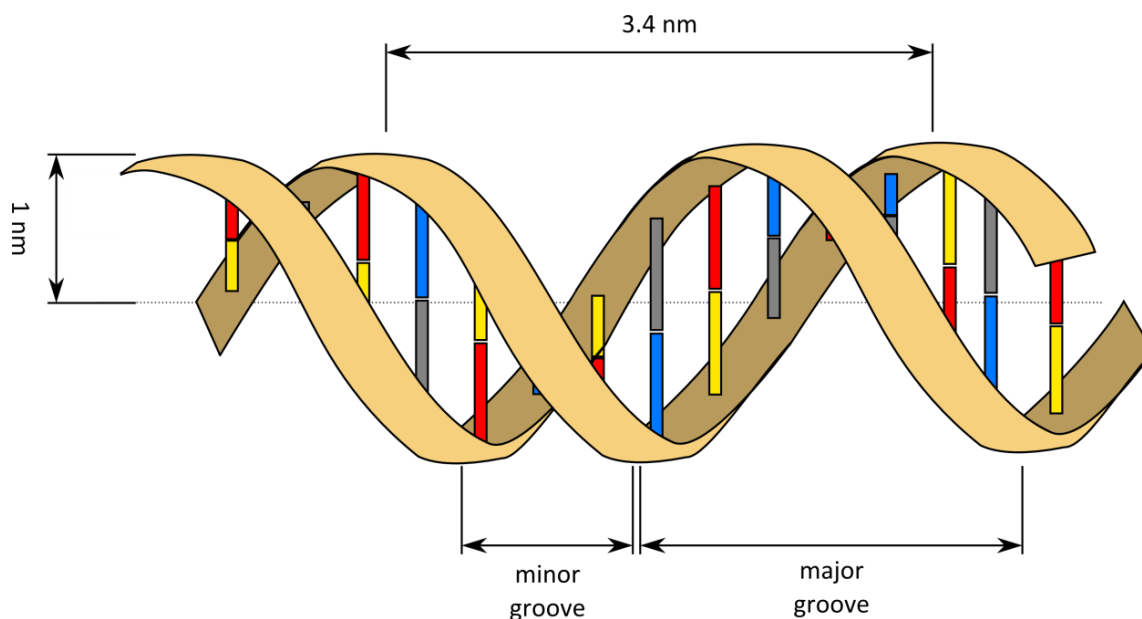


Figure 11: Schematic representation of a typical B-DNA molecule with its four possible nucleotides thymine (red), adenine (yellow), guanine (grey) and cytosine (blue).

Intercalation of planar aromatic molecules into a DNA strand, a term introduced by Lerman in 1961¹⁴⁹, is a process that can alter the physical and physiological properties of DNA, e.g. for fluorescence labeling¹⁵⁰. A molecule, well suited for this purpose is the bisintercalating fluorophore YoYo-1, a homodimer of oxazole yellow (Figure 12) which has an affinity constant of $K_{YOYO} = 6.0 \cdot 10^8 \text{ Mol}^{-1}$ in phosphatebuffer with pH=7, [NaCl]=100mM¹⁵¹. Because of its four positive charges, it is attracted by a DNA strand in free solution. The oxazole yellow monomers are planar structures and can therefore intercalate into the space between two adjacent basepairs^{149,152}. It is possible, that both monomers intercalate into the DNA strand (bisintercalation) leaving one intercalations site free in between or that only one monomer intercalates (monointercalation) with significantly lower affinity constant. During intercalation, the YOYO molecule is deformed in such a way, that fluorescence emission is enabled, while in free solution, YOYO is practically invisible¹⁵².

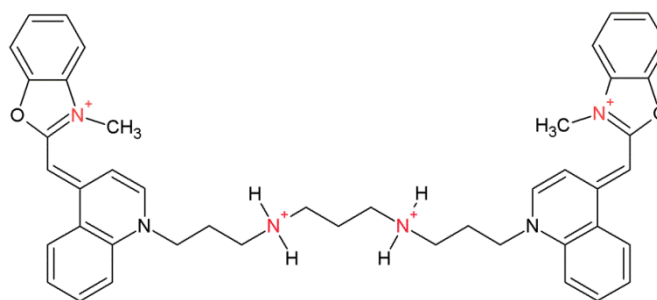


Figure 12: Structure formula of 1,1' - (4,4,7,7 - tetramethyl - 4,7 diazaundecamethylene) - bis - 4 - [3 - methyl - 2,3 - dihydro - (benzo - 1,3 - oxazole) - 2 - methylenidene] - quinolinium tetraiodide (YOYO-1). The four positive charges are marked red^{153,154}.

3 MATERIALS AND METHODS

This chapter gives an overview over the experimental and theoretical procedures, which were employed within the framework of this thesis. The first section 3.1 lists all required chemicals, materials, and laboratory equipment, followed by an explanation of how the masterwafers, the microfluidic chips, and the chiral microparticles were fabricated (section 3.2). The topic of section 3.3 is the preparation of the sample solutions and the treatment of channel surfaces. Section 3.4 deals specifically with the experimental setup whereas section 3.5 highlights the theoretical methods that were used to analyze the chiral separation experiments.

3.1 LIST OF CHEMICALS AND LABORATORY EQUIPMENT

The following two tables list all chemicals, materials, and laboratory equipment required for the experiments in this thesis.

Table 1: Chemicals and Materials required for the experiments in this thesis.

Chemical / Material	Manufacturer
4" Si-Wafer, polished, undoped	CrysTec, Germany
5" Si-Wafer, polished, undoped	CrysTec, Germany
Acetone (p.a.)	VWR, Germany
Deionized water, $\chi=0.3$ mS/cm	Millipore, USA (Equipment manufacturer)
Deoxyribonucleic acid (DNA) 12000 bp	Biotechnologisches Labor Dr. Bartling, Germany
Deoxyribonucleic acid (DNA) 48502 bp	Promega, USA
Ethanol (p.a.)	VWR, Germany
Ethylenediaminetetraacetic acid (EDTA)	Fluka, Germany
Gamma botyrolactone	Roth, Germany
Hydrogenperoxide (H ₂ O ₂), 30%	VWR, Germany
Isopropyl alcohol (p.a.)	VWR, Germany
Microbeads (carboxylated polystyrene) $\phi=1.1$ μm and $\phi=2.9$ μm	Interfacial Dynamics
Microbeads (carboxylated polystyrene), fluorescent $\phi=0.5$ μm and $\phi=1.9$ μm	Interfacial Dynamics
Negative Photoresists SU-8 (2), (5) and (10)	Microchem, USA
Developer MR-DEV 600	Microresist, Germany
Nitrogen (p.a.)	Linde, Germany
Nitrogen (tech.)	Linde, Germany
Oxygen (p.a.)	Linde, Germany
Performance optimized polymer (POP6)	Applied Biosystems, USA
Pluoronic F108	BASF, Germany
Polyethylene glycol PEG3400	Nektar, USA
Polyethyleneglycol PEG3400	Nektar, USA
Soda lye, 1M (tech.)	Merck, Germany
Sulfuric acid (H ₂ SO ₄), 96%	VWR, Germany
Tridecafluor-1,1,2,2-tetra-hydrooctyl-trichlorosilane (TDTS)	ABCR, Germany
Tween® 20	BASF, Germany
YOYO-1, 1mM	Molecular Probes, USA
β -Mercaptoethanol	Fluka, Germany

Table 2: Laboratory equipment required for the experiments in this thesis.

Microscopy equipment and accessoires	Manufacturer
CCD-Camera, model Sencicam qe	PCO, Germany
Computer for image acquisition (PC II)	TICO, Germany
CP-Achromat 10x objective	Zeiss, Germany
Fluorescence filter cube consisting of BP 450-490, BP 515-565, FT-510	Zeiss, Germany
Inverted fluorescence microscope, model Axiovert 200	Zeiss, Germany
LD-Achroplan 20x objective	Zeiss, Germany
LD-Achroplan 60x objective	Zeiss, Germany
Mercury Arc Lamp, model HBO100, P = 100 W	Zeiss, Germany
Motorized microscopy stage, model 99S008	Ludl Electronics, USA
PANdrive stepper motor incl. cabling, model PD-110-42	Trinamic, Germany
Plan-Neofluar 100x objective, Na=1.3	Zeiss, Germany
Scanning electron microscope, model JSM 880	Jeol, Japan

Experimental Setup	Manufacturer
Control computer (PC I)	TICO, Germany
Data acquisition PCI card, model PCI 6704	National Instruments, USA
Digital Signal Processor, model Adwin Gold II	Adwin, Germany
Digital valves MHA2-MS1H3/2GK-2-K-196121 (6 pcs.) incl. tubing	Festo, Germany
Electrometer, model 6517A	Keithley, USA
GPIB interface PCI card, model PCI-GPIB	National Instruments, USA
High Voltage amplifier, model AMS-1B30 incl. cabling	Matusuda Precision, Japan
High Voltage transformers, model FUG HCL 14-12500 (2 pcs.)	FUG Elektronik, Germany
Proportional pressure regulator Airfit Tecno PRE-U	Hoerbiger, Germany
Security Relais Box	Self-constructed
Sidewinder Force Feedback 2	Microsoft, USA

Cleanroom equipment	Manufacturer
Centrifuge, model 5417c	Eppendorf, Deutschland
Centrifuge, model Delta 10	BLE, Germany
Desiccator incl. rotary vane pump	n/a
Fineplacer® Lambda	Finetech, Germany
Glass vials, V = 2 ml	VWR, Germany
Glass-chromium-photomasks	Delta Mask, The Netherlands
Oxygen-plasma device	Self-constructed, see ^{49,155,156}
Profilometer, model DEKTAK 3030 ST	Sloan, USA
Programmeable hot plate, model PR 5 SR	Detlef Gestigkeit, Germany
Spincoater, model ST147	Convac, Germany
Sputterdevice, model MCS 010	BAL-TEC, Liechtenstein
Ultrasonic bath, model T490DA	Elma, Germany
UV-exposer unit, model 8011	Oriel, USA

Microchip fabrication materials	Manufacturer
Acrylic glass, 5mm thickness	Miscellaneous
Connecting piece for silicone tube, ϕ =3mm	Festo, Germany
Microscope slides 24 mm x 60mm	Menzel-Gläser, Germany
Platinum wire, ϕ = 0.4mm	Chempur, Germany
Polydimethylsiloxane Sylgard 184 (PDMS)	Dow Corning, USA
Silicone tube, ϕ =3mm	Festo, Germany

3.2 FABRICATION PROCEDURES

This section deals with procedures to fabricate the three fundamental components for the experiments. The basis for the chip production are masterwafers (paragraph 3.2.1) as a mold for soft lithography with PDMS (paragraph 3.2.2). The fabrication procedure for the chiral test particles is discussed in paragraph 3.2.3.

3.2.1 MASTERWAFERS

The basis for the microfluidic chip fabrication is a 4 inch or 5 inch silicon wafer. Negative reliefs of the desired chip structure are lithographed onto its polished surface using the negative tone photoresists SU-8.

For this purpose, the wafers are cleaned in caroic acid, a 1:3 mixture of hydrogen peroxide and 95% sulfuric acid, for at least 20 minutes and rinsed thoroughly with deionized water afterwards. Centrifugation and heating the wafer up to 200°C for another 20 minutes removes residual water on the surface. Depending on the structure's desired thickness, SU-8 (2), (5), or (10) is now applied to the wafer and spincoated for 5 seconds at 500 rpm and for 30 seconds at a predefined speed between 1500 rpm and 3000 rpm (see Table 3). After the prebake procedure (40°C, 60°C for 5 minutes and 90 °C for 15 minutes, ramp rates: 3 °C/min, 2°C/min, 2 °C/min) a chromium-glass mask is used to control cross linking of the resist with the i-line of a mercury pressure lamp with roughly 140 mJ/cm² (Figure 13 A). The samples are now postbaked with the same parameters as during the prebake and developed in MR-DEV 600 for 30 s, rinsed with acetone and isopropyl alcohol, and dried with nitrogen. After an optical inspection under a microscope the wafer is heated up to 200°C for a few minutes (hard bake) to repair small defects and harden the SU-8 structure (Figure 13 B).

Afterwards, a thin TDS layer is deposited onto the wafer's surface to prevent sticking of PDMS in the following fabrication steps. Therefore, the wafer is placed together with a glass coverslip with a few droplets of TDS into a desiccator which is then evacuated for 15 minutes with a standard rotary vane pump and sealed for further 15 minutes.

Table 3: Parameters for the SU-8 processes employed for the different experiments in this thesis.

Experiment	Section	Height [μm]	Su-8 type	Spin speed [rpm]
Selective Ratchet	4.1	10	10	3000
DNA Microchips	4.2	6	5	2250
Post Array Chip	4.3.2	6	5	2250
Structured 2D sidewalls	4.3.3	6	5	2250
Structured 3D sidewalls	5	10	10	3000

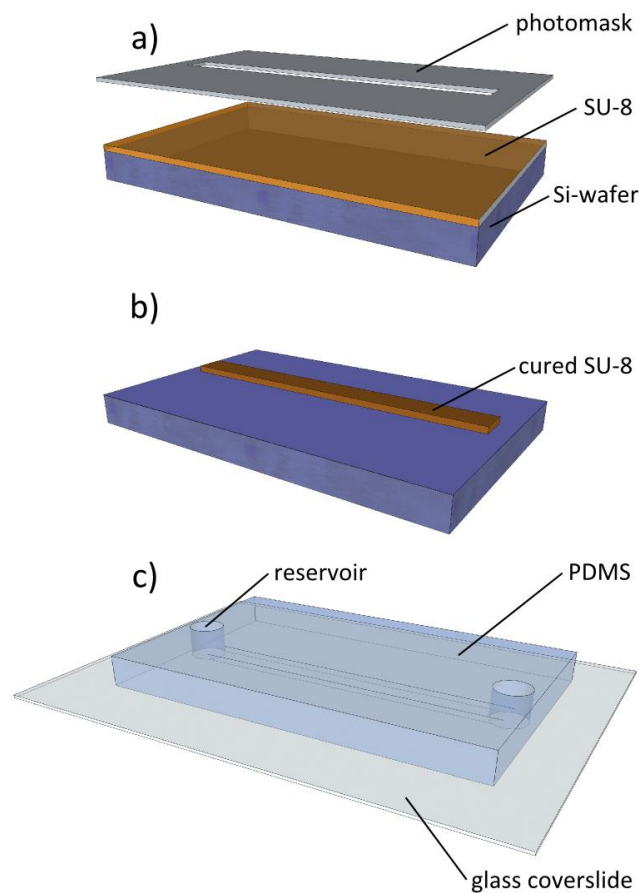


Figure 13: Procedure for fabricating the microfluidic devices that were used in the experiments for this thesis. a): A standard silicon wafer is precleaned with carotic acid and spincoated with the negative tone photoresist SU-8. After a prebake step, a photo mask which is transparent for UV radiation at certain areas is placed on top and irradiated with UV light. b): The photomask is removed and the wafer is developed after the post bake procedure. A negative relief of the desired channel structures resides on the wafer surface and is hardbaked and covered with TDS afterwards. c): PDMS is mixed in a 10:1 ratio with a platinum linker and cured by heating it to 85°C for four hours. It can now be removed from the wafer surface and the channels are cut out and reservoirs are punched. The chip is then covalently bound to a PDMS coated glass coverslide using oxygen plasma.

3.2.2 MICROFLUIDIC CHIPS

The fabricated masterwafer is now ready to use for the following soft lithography procedure^{157,158}. 20 g of the Sylgard® 184 base polymer are mixed with 2 g of the curing agent included in the packaging and thoroughly mixed. The mixture is distributed onto the wafer while being placed in a petri dish. Residual air bubbles from the mixing process are removed subsequently by placing the wafer into a desiccator for a few minutes. The PDMS linking process is initialized by heating the wafer to 85°C for four hours in a dryer oven. After cooling down to room temperature, the cured PDMS can be peeled off the wafer and the regions of interest containing the microchannels are cut out with a scalpel. The Reservoirs are punched into the PDMS using modified punch pliers. Subsequently the chips are cleaned in an ultrasonic bath while immersed in acetone, ethanol, and dionized water in sequence and dried with nitrogen.

To permanently seal the microfluidic chip, the PDMS slips and PDMS coated microscopy cover slides are exposed to an oxygen plasma in a self-developed plasma chamber, based on⁴⁹ with the process parameters given in Table 4. The PDMS coated cover slides for sealing the channels are fabricated in advance by spincoating 1ml of PDMS onto their surface before baking them at 85°C onto a hotplate for 30 minutes. Both plasma treated surfaces are now gently pressed against each other. After approximately 30 minutes, the PDMS slip and the microscopy cover slide are attached to each other by stable covalent bonds (Figure 13 C). The inspection of the microchip designs is performed while being unsealed with a scanning electron microscope after sputtering approximately 10 nm of gold onto their surface. However, those gold-coated chips were not used in the experiment and disposed after inspection.

Table 4: Process parameters for the oxygen plasma to seal the microfluidic devices.

Parameter	Value
Oxygen pressure	10-1 mbar
Operation Voltage	50 kV
Operation Frequency	500 kHz
Distance of electrodes	6.15 cm

3.2.3 CHIRAL MICROPARTICLES

The fabrication procedure of the microparticles is similar to the master wafers. A silicon wafer is cleaned in carotic acid for 20 min and rinsed with deionized Water. Centrifugation and heating up to 200 °C for 20 min on a contact hotplate removes residual water.

SU-8 (2) is applied to the wafer and spincoated at 500 rpm for 5 s and subsequently at 2000rpm for 30s (see Figure 14 a)). After the prebake procedure (40°C, 60°C for 5 minutes and 90 °C for 15 minutes, ramp rates: 3 °C/min, 2°C/min, 2 °C/min) a chromium-glass mask is used to initialize cross linking of the resist with the i-line of a mercury pressure lamp with approximately 140mJ/cm². The samples are postbaked with the same parameters as for prebake and developed in MR-DEV 600 for 30 s, rinsed with acetone and isopropyl alcohol, and dried with nitrogen (see Figure 14 b)). Prior to the particle's characterization via scanning electron microscopy while still attached on the surface, a 20nm layer of gold was sputtered onto them in advance. These gold-coated particles were not used in the experiment and disposed after inspection.

For particle release, the substrate's structured part is cut out of the wafer and dropped into a small vial together with 2 ml deionized water. The vial is subsequently placed in an ultrasonic bath at full power for 10-30 seconds until the particles are fully released (see Figure 14 c)). Afterwards the silicon substrate is removed from the vial.

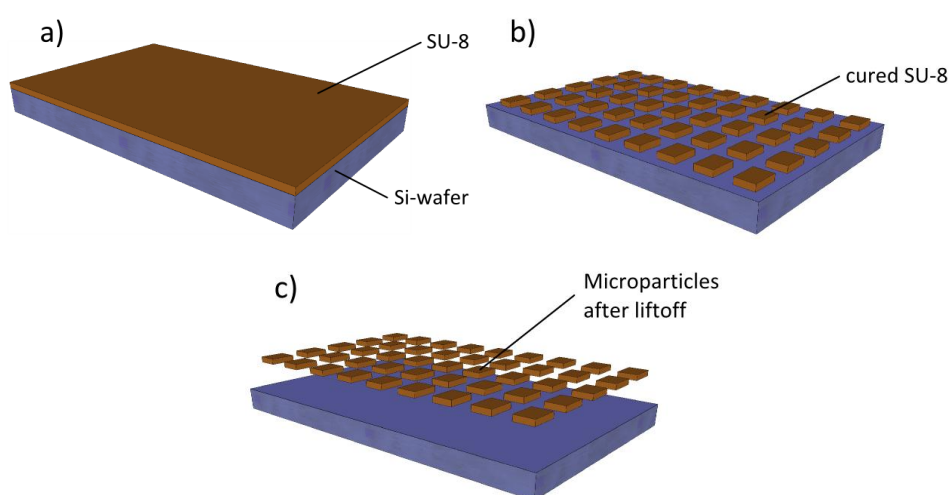


Figure 14: Fabrication procedure of the microparticles that are used for the chiral separation experiments. a): A standard silicon wafer is precleaned with carotic acid and spincoated with the negative tone photoresist SU-8 (2). After a prebake step the wafer is masked and irradiated with UV light. b): The wafer is developed after the post bake procedure. Microparticles reside on the wafer surface which is not hardbaked in this procedure. c): The wafer's structured area is cut out and placed with 2 ml of water in a vial. Sonificating the vial for 10-30 seconds at full power removes the particles from the surface.

3.3 SAMPLE AND SURFACE PREPARATION

The channel surfaces and the considered analytes were pretreated before the experiment according to the following procedures.

Microbeads

Prior to usage (in sections 4.1 and paragraph 4.3.3), approximately 50 μl of the original solution of carboxylated polystyrene microbeads are mixed with 1000 μl of 1 M soda lye and thoroughly mixed. After centrifugation (5 minutes at 10 krpm) the fluid is removed and 1000 μl of new soda lye are added. This process is performed three times. After the last centrifugation step, the particles are resuspended into 1000 μl 10mM phosphate buffer (pH=8.3) containing 200 μM Tween[®] 20.

DNA and DNA Buffer

The basic buffer solution for all DNA experiments (section 4.2) consists of 10 mM phosphate buffer (pH=8.3), 1mM EDTA, and 0.1 % POP-6. The DNA solution is furthermore spiked with 50 pM of the corresponding DNA type, 0.2 % β -Mercaptoethanol, and 1 YoYo-1 molecule per 10 base pairs. All solutions for the measurements concerning the dependence of the ionic strength on the polarizability (paragraph 4.2.2) were adjusted accordingly by adding different amounts of sodium chloride until the desired ionic strength is achieved. The experiments to investigate the dependence of YoYo-1 on the polarizability (paragraph 4.2.3) were carried out with no extra sodium chloride but with different amounts of YOYO-1 which was given enough time to intercalate into the DNA by incubating the freshly generated mixtures of DNA and YoYo at least for 48 hours in a fridge before usage.

Chiral Particles

Directly after sonification and removal of the substrate, 200 μM Tween[®] 20 is added to the deionized water, the particles are suspended in.

Channel Surfaces

The microfluidic chips used for the tunable ratchet experiment (section 4.1) are coated with the commercially available triblock copolymer F108. For that purpose 500 μM of F108 dissolved in deionized water are filled into one of the reservoirs 30 minutes after chip assembly. After the complete channel is filled, the other reservoir is filled as well. The F108 solution is now incubated for at least 3 hours. Subsequently the liquid in the reservoirs is

dumped and refilled with 10 mM phosphate buffer (pH=8.3). Excess F108 is washed out of the channel by applying a water-jet vacuum pump to one of the reservoirs for 20-30 seconds. This reservoir is then filled with the bead solution described above. For the DNA experiments (section 4.2), the channels are covered with 3 μ M PEG-3400 with the same protocol, except that no water-jet pumping was carried out and the solution was incubated only for exactly 20 minutes. The micro channels for the chiral separation experiments (section 4.3) were not pretreated and only filled with deionized water 30 minutes after oxidization, because here, no electrical driving is used.

3.4 EXPERIMENTAL SETUP

The central element of the experimental setup (Figure 15 - Figure 17) is an inverted fluorescence microscope which has been equipped with a 100 W mercury short arc lamp at its backport and a fluorescence filter set consisting of the emission filter BP 515-565, the dichroic mirror FT-510, and the excitation filter BP 450-490 (Figure 15) to enable fluorescent imaging of microbeads and DNA. Non-fluorescent objects are illuminated with the installed halogen white light lamp. For observation, the microfluidic chip is installed onto an automatically moveable stage, which can be controlled via the software micromanager¹⁵⁹ or manually with a joystick. For image acquisition, a CCD camera is attached to the microscope's primary camera port. A computer (PC II, see Figure 16) with installed Sensicam PCI Interface board reads out the camera and visualizes video data using Micromanager¹⁵⁹. The software provides an autofocusing routine as well. Via a self-constructed focus-drive add-on based on a PANdrive PD-110-42 attached to one of the manual focusing handles, the microscope has been upgraded with autofocusing capabilities.

The setup provides hydrodynamic (green box in Figure 16, see section 2.1) and electric (grey box in Figure 16, see section 2.2) flow control for microfluidic chips, operated by PC I. The required voltage protocols are generated by an Adwin Gold II digital signal processor (for source code see appendix A2.2) and amplified 100 fold afterwards by a Matsusada AMS 1B30 HV amplifier.

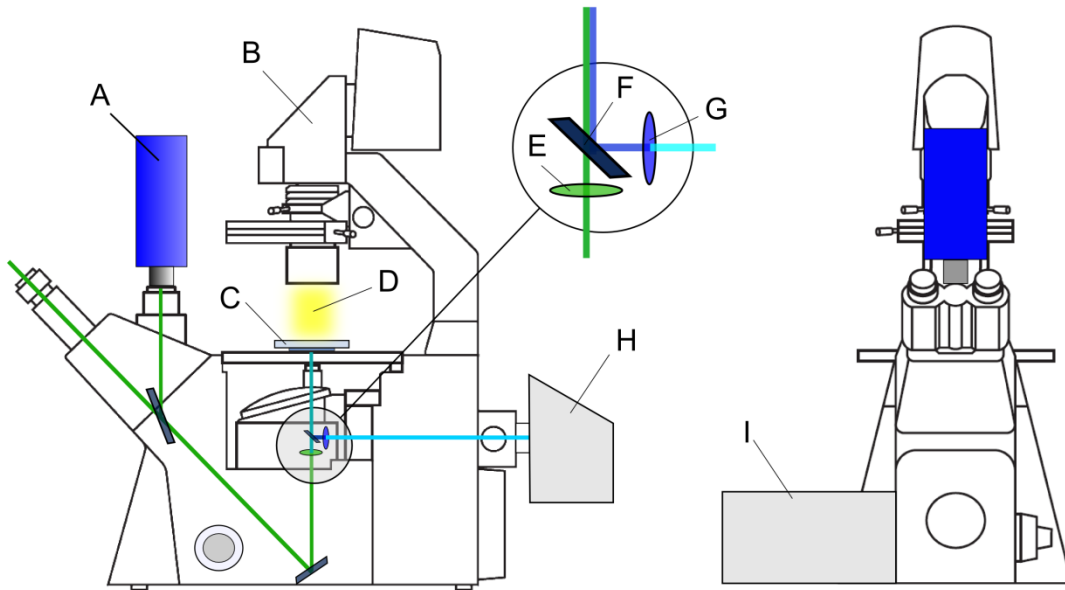


Figure 15: Scheme of the optical components. The inverted optical fluorescence microscope Axiovert 200 is equipped with a sensicam qe CCD camera (A). Besides the illumination of the microfluidic chip (C) with white light (B, D), fluorescence imaging is conducted via Zeiss filter set 10 (see enlargement). It consists of the emission filter BP 515-565 (E), the dichroic mirror FT-510 (F), and the excitation filter BP 450-490 (G). Excitation light is provided by a 100W HBO100 mercury short-arc lamp (H). Automated focusing is enabled with a self-constructed focus drive (I) operated by the software Micromanager¹⁵⁹. Modified with kind permission from¹⁶⁰.

To control signal quality, the amplifier's voltage monitor output (V_{moni}) is looped back to a DSP voltage input. Hence, especially offset correction of sinusoidal alternating voltages up to a peak value of 1 kV with 25 millivolts precision (after amplification) is possible as the DSP continuously monitors, evaluates, and corrects its own output including effects introduced by the amplifier. There are two further voltage sources (FUG HCL 14-12500 HV transformers) with less precision and voltage shifting speed for support purposes. All three voltage sources are connected to a self-constructed relay box for security reasons which can either be operated manually or via PC II while manual operation strictly overrides automated operation. A fourth connector provides ground potential. Hydrodynamic flow control is provided by a very precise self-constructed pneumatic pumping device basically consisting of two linear pressure regulators Airfit Tecno PRE-U (for detailed information consult appendix A1) which are controlled by PC II as well.

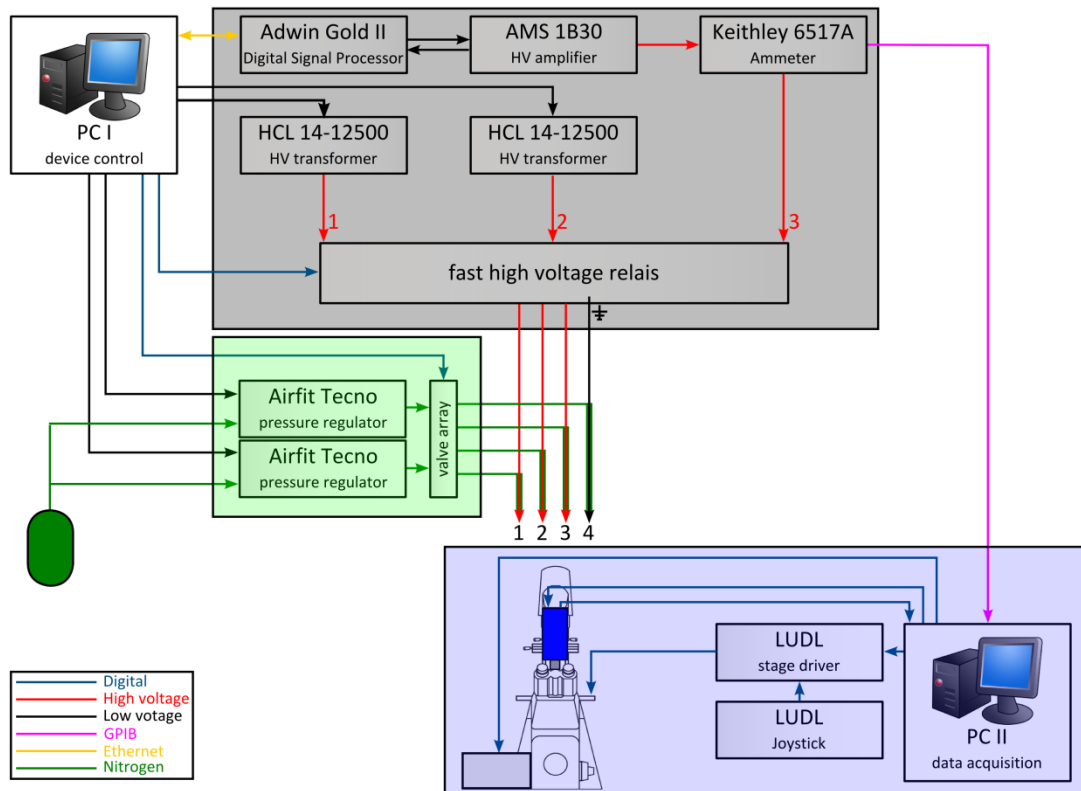


Figure 16: Schematic of the electronic and pneumatic setup. The basic component of the arrangement is a fluorescence microscope for observation and video microscopy of the microfluidic chips (blue box). During the experiment, the chips are operated by either electrical potentials (grey box) or hydrodynamic pressure differences (green box) or both, provided by the four chip connectors 1,2,3,4. The desired voltage protocols are generated by an Adwin Gold II DSP and 100 fold amplified with an AMS 1B30 HV amplifier. The voltage monitor-port V_{moni} of the amplifier is reconnected to one of the DSP voltage input ports to setup a feedback loop. All high voltage lines are secured with an emergency relay switch, operated either manually or by PC I. Hydrodynamic control is provided by a self-constructed pneumatic pressure pump, described in detail in appendix A1. The schematic of the microscope is taken with kind permission from¹⁶⁰.



Figure 17: Photograph of the experimental setup.

3.5 NUMERICAL PREDICTION OF CHIRAL SPLITTING ANGLES

To effectively identify a design parameter set for the separation of chiral microparticles (paragraph 4.3.2) extensive numerical simulations were conducted before. The underlying model is depicted in Figure 18 b). 240 tightly packed and rigidly connected “monomers” with diameter d_m are arranged in a way, that they imitate the experimental microparticle in Figure 18 a) with a length of the long axis a as good as possible¹⁶¹. The behavior of this construct while traveling through the post lattice is described by three degrees of freedom: x and y coordinate as well as the current rotation angle φ in the x y plane. The movement in z direction as well as rotations in the x-z and y-z plane are omitted because the experiment is considered to be quasi two dimensional (see paragraph 4.3.2). Hence, the remaining core problem of the applied numerical calculation is solving the stochastic differential equation

$$\beta_i[\vec{v}(\vec{r}_i(t)) - \dot{\vec{r}}_i(t)] - \nabla W_{\text{Wall}}(\vec{r}) + \sum_{i \neq j} \vec{S}_{ij}(\vec{r}_i(t), \vec{r}_j(t)) + \sqrt{2\beta_i k_B T} \vec{\xi}_i(t) = 0$$

for each monomer i . This so called Langevin equation describes dynamics in an overdamped limit. It consists of β_i , the friction coefficient between fluid and particle i (see paragraph 2.1.2), W_{Wall} a linear periodic potential (4 pN/ μm and zero outside the post), used to model particle-wall collisions, \vec{v} the velocity of the fluid, $\sqrt{2\beta_i k_B T} \vec{\xi}_i(t)$, a stochastic force acting on the particle resulting from Brownian motion at room temperature where $k_B T \approx 4\text{fN } \mu\text{m}$ (see section 2.3), and \vec{S}_{ij} , the forces exerted by another monomer j due to their rigid connection. The hydrodynamic field $\vec{v}(x, y)$ is obtained before by solving the Navier-Stokes-equation (see section 2.1) via Comsol Multiphysics® (version 3.5a) on a regular spatial grid with $dx = dy = 50\text{nm}$, where no slip boundary conditions were assumed on all surfaces (as justified in paragraph 2.1.1). The impact of the chiral particle on the fluid flow however has been neglected. For the computation of the actual particle trajectories an Euler algorithm with dynamically adjusted time steps between 1 ps and 50 ms implemented by M. Fliedner was used.

Each data point in the overview plots in Figure 46, Figure 47, and Figure 48 consists of 50 single trajectories for each chiral flavor. The results for the migration angles were obtained by computing the average displacement vector between the first and the last point of each trajectory together with the appropriate standard deviation. To generate Figure 49 a set of 100 single trajectories for each chiral flavor per value of α , the array tilting angle, were simulated and processed in the same way.

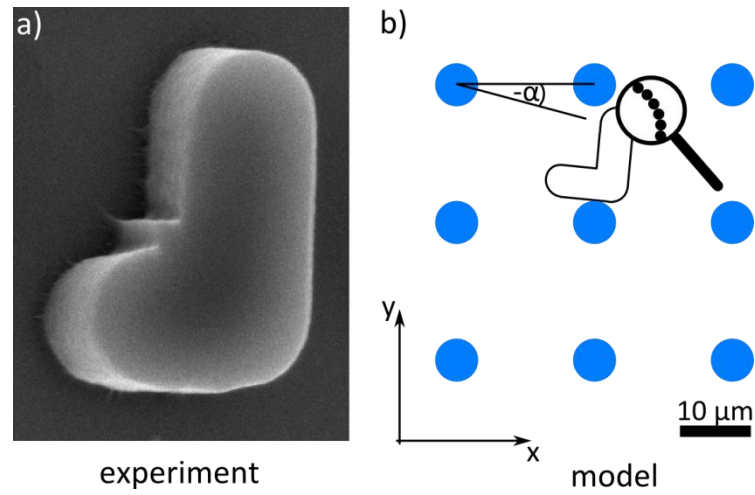


Figure 18: a) Electron microscope image of a chiral particle that was used in the experiments. Note that no scale bar is provided, because the image has been taken slightly from the side. b) Theoretical model for a chiral particle traveling through an elementary cell of the post array (blue, with periodicity l_p) with posts of diameter d_p . The particle with long axis a is mimed by a densely packed and rigidly connected shell of 240 beads with diameter d_m (see magnification). A constant force that will drive the particle is applied to the elementary cell under an angle of $-\alpha$. The resulting force field is given by the Navier Stokes equation and solved with Comsol Multiphysics® before.

4 RESULTS AND DISCUSSION

The main theme of the present work is the use of spatially structured microfluidic channels for separating and analyzing different (bio-) particle species. The three main projects are represented by the three sections in this chapter.

With a new generic ratchet concept implemented in a microfluidic channel, a device is engineered, which is able to sort (bio-) particles with a freely and instantly tunable selectivity criterion (see section 4.1). As a result, a subset of particle species (arbitrarily chosen by applying specific voltage pulses to the device) is made to migrate into opposite direction than the remaining species. However, a different series of voltage pulses will instantly select other species to be extracted.

Many microfluidic systems rely on dielectrophoresis to sort or manipulate a polarizable sample^{60,63,162–164} in microfluidic environments. Unfortunately the polarizability of the considered single objects usually remains unknown. Appropriate electric fields are chosen via trial and error methods because so far, quantitative values of the polarizability α_p are only addressable via macroscopic ensemble methods. Section 4.2 discusses a method to automatically obtain single molecule polarizabilities, based on a structured microfluidic system⁸². The technique is applied to investigate the influence of intercalating dyes on the DNA's polarizability.

Chiral separation remains a challenge in analytical organic chemistry because a suitable chiral selector or derivatization chemical needs to be specially developed for every new analyte to perform chromatography. Section 4.3 deals with two different generic approaches to *continuously* separate chiral objects from each other via physical symmetry breaking and thus *without* the need for any selector.

4.1 MICROFLUIDIC RATCHETS WITH DYNAMICALLY CHANGEABLE SELECTIVITY

Standard biotechnological separation techniques hold the disadvantage, that the separation criterion is usually unchangeably implemented during fabrication. Gel electrophoresis^{165–167} is such a technique, where the order of resulting

Results discussed in this section have been published in: L. Bogunovic, R. Eichhorn, J. Regtmeier, D. Anselmetti & P. Reimann: *Particle sorting by a structured microfluidic ratchet device with tunable selectivity: theory and experiment*, *Soft Matter* 8 (2012), 3900–3907

bands is unchangeable and where the predefined and therefore fixed gel density dictates the selectivity range. Additionally, such techniques usually require huge amounts of sample material compared to microfluidic devices being able to operate on single molecule scales.

The aim of the present project is the development of a microfluidic device for the extraction of any desired subset of particle species out of a mixture of N different species. Additionally the particles to extract should effectively migrate into the opposite direction with respect to the remaining species (for a schematic example with $N = 3$, see Figure 19). This separation criterion should only be implemented by instantly changeable electrokinetic driving applied to the system and not by any fixed geometric feature in the channel.

A microfluidic channel is structured with non-conducting posts with inherent broken symmetry in x -direction, the relevant transport direction. Together with the applied electric voltage scheme $U(t)$, furnishing sufficient tilting of the potential acting on the particles, the microfluidic device shows features of a ratchet characteristic^{24,83–85} (see paragraph 2.4.2).

So far, such ratchet systems have been studied and widely used for different sorting purposes. In 1994 Rousselet et al. presented the first realization of a Brownian ratchet on the microfluidic scale⁸⁶. They used an asymmetric microelectrode array driven with a symmetric AC voltage to transport microparticles through a microchannel with no effective bias force. Here the effective particle transport is carried out by Brownian motion rectified by an asymmetric dielectrophoretic potential. Based on that design, Faucheux and Libchaber separated two different types of microspheres according to their diffusion coefficients¹⁰⁸. A quite similar system has been studied in more detail by Gorre-Talini et al.

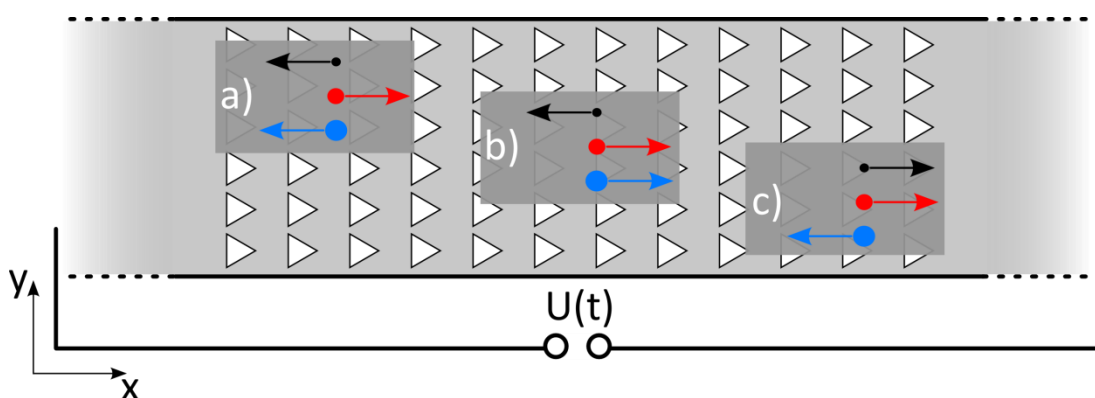


Figure 19: Schematic representation of the underlying separation principle (not to scale) using an extended ratchet mechanism for three different exemplary particle species (black, red, and blue). An applied voltage protocol $U(t)$ is applied to a periodically structured microfluidic channel. Using a sophisticated interplay between electrophoretic forces and dielectrophoretic forces, the system is capable of extracting a freely choosable particle species out of the mixture by moving it to the opposite direction according to a), b), or c). The voltage protocol is instantly changeable resulting in considerable dynamic selectivity of the device.

some years later^{111,112}. With an alternative approach based on free standing asymmetric posts, Duke et al.¹⁶⁸ as well as Ertaş¹⁶⁹ introduced a second dimension for particle separation. In their studies, the authors independently realized continuous separation of particles based on their diffusion coefficients by exploiting the induced transverse drift with respect to the applied forces. Ten months later, this idea was improved by Derényi and coworkers¹⁰⁵. Mostly based on these studies, a huge variety of different ratchet systems in microfluidic devices were developed in the last two decades e.g.^{106,107,109,110,113–116,118,119,170–174}.

By combining all possible ways of symmetry breaking concerning ratchet effects (spatial, temporal/dynamical, and bias forces) the present approach addresses the next natural challenge – a device being able to extract an anytime freely selectable subset of the N introduced particle species out of the mixture by moving it into opposite direction.

The microfluidic system which has been developed in this context is depicted in Figure 20 and was fabricated as described in paragraph 3.2.2. The structure consists of a straight 1 cm long (x direction) and 300 μm wide (y direction) microchannel with 10 μm height (z direction), located between two fluid reservoirs with 2 mm diameter (see Figure 20 a)). The channel is structured with triangular posts (structured region drawn in grey) with lattice constants of 20 μm in x direction and 14 μm in y direction. The triangles have a length and

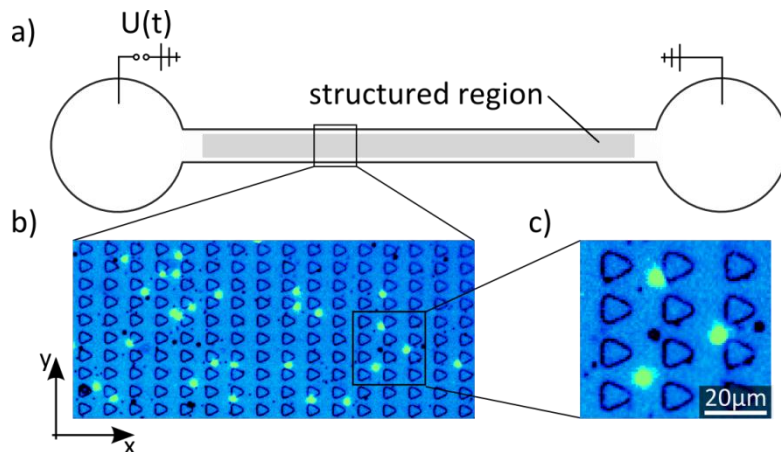


Figure 20: a) Schematic representation of the experimental setup. A 10 μm high (z direction) and 300 μm wide (y direction) microfluidic channel connects two reservoirs with immersed electrodes. It is structured with triangular obstacles to form dielectrophoretic traps for selectively manipulating a certain particle species. b) Optical micrograph of the post array. This structured region extends over 1cm in x direction (lattice constant 20 μm) and 300 μm in y direction (lattice constant 14 μm). Each post extends over 10 μm in x as well as in y direction. The gaps are 10 μm wide in x direction and 4 μm wide in y direction. c) Magnification of the framed region in b). The channel is filled with an emulsion containing particles with a diameter of 1.1 μm , 1.9 μm (fluorescent), and 2.9 μm respectively. These three species can easily be distinguished by their size and fluorescence under a microscope.

width of 10 μm and are completely extended from the channel bottom to the ceiling (see Figure 20 b and c). For the experimental realization, three different particle species with diameters of 1.1 μm (small black spots in Figure 20 c), 1.9 μm (fluorescent), and 2.9 μm (big black spots) are immersed into a buffer solution (see section 3.3) and filled into the device. Because of the specific fluorescent labeling and the different diameters, the particles can be easily distinguished visually under the microscope.

In this section the proposed idea of the dynamically changeable separation device based on an extended ratchet concept with built in arbitrary extraction of any particle subset is described and discussed in detail. The basic idea behind the separation scheme is theoretically devised in paragraph 4.1.1 and the special case of three different particle species, later considered in the experiment is discussed in more detail. The experimental results are presented in paragraph 4.1.2. The option to further increase the number of particles is evaluated theoretically in paragraph 4.1.3 followed by concluding remarks in paragraph 4.1.4.

4.1.1 THE SEPARATION CONCEPT

The main purpose of the developed device is the extraction of an arbitrary subset of certain particle species out of a mixture by forcing it/them to move in the opposite direction with respect to all remaining particles. This paragraph describes how the claimed task can be accomplished by applying a time dependent voltage protocol to the chip.

When a time dependent signal

$$U(t) = U_{DC} + U_{AC} \cdot \sin(\omega t)$$

with $\omega/2\pi = 100\text{Hz}$ is applied to the terminals of the microfluidic channel, an electric field

$$\vec{E}(\vec{r}, t) = \vec{E}_{DC}(\vec{r}) + \vec{E}_{AC}(\vec{r}) \cdot \sin(\omega t)$$

results in the device (see Figure 21). Consequently a charged and polarizable particle like the carboxy-terminated polystyrene particles and most biological macromolecules will be subjected to three different kinds of forces (see paragraphs 2.2.1, 2.2.2, and section 2.3 for details):

- The *electrophoretic* force $\vec{F}_{EP}(\vec{r}, t) = q^* \cdot \vec{E}(\vec{r}, t)$, where q^* is the effective charge of the particle system
- The *dielectrophoretic* force $\vec{F}_{DEP}(\vec{r}, t) = \alpha_p \vec{\nabla} \vec{E}^2(\vec{r}, t)$, which is dependent on the field gradient caused by the non-conducting triangular structures
- The *stochastic* forces, induced by the omnipresent thermal fluctuations $\vec{F}_D(t) = \beta \sqrt{2D} \vec{\xi}(t)$.

While the only (unpractical) option to control \vec{F}_D in the present device is changing the temperature, the remaining forces \vec{F}_{EP} and \vec{F}_{DEP} depend on the actual space and time dependent electric field $\vec{E}(\vec{r}, t)$ which can be easily adjusted. For $|U_{DC}| \ll |U_{AC}|$ and sufficiently large U_{AC} one can safely argue, that $\vec{E}_{AC} \cdot \sin(\omega t)$ is only responsible for dielectrophoretic forces and that only \vec{E}_{DC} contributes to the electrophoretic motion only. Because of the involved strictly symmetric sine function, all effects induced by $\vec{E}_{AC} \cdot \sin(\omega t)$ are symmetric as well and thus average out on a timescale much larger than the period length. Because of the relatively high frequency $\omega/2\pi = 100$ Hz, one

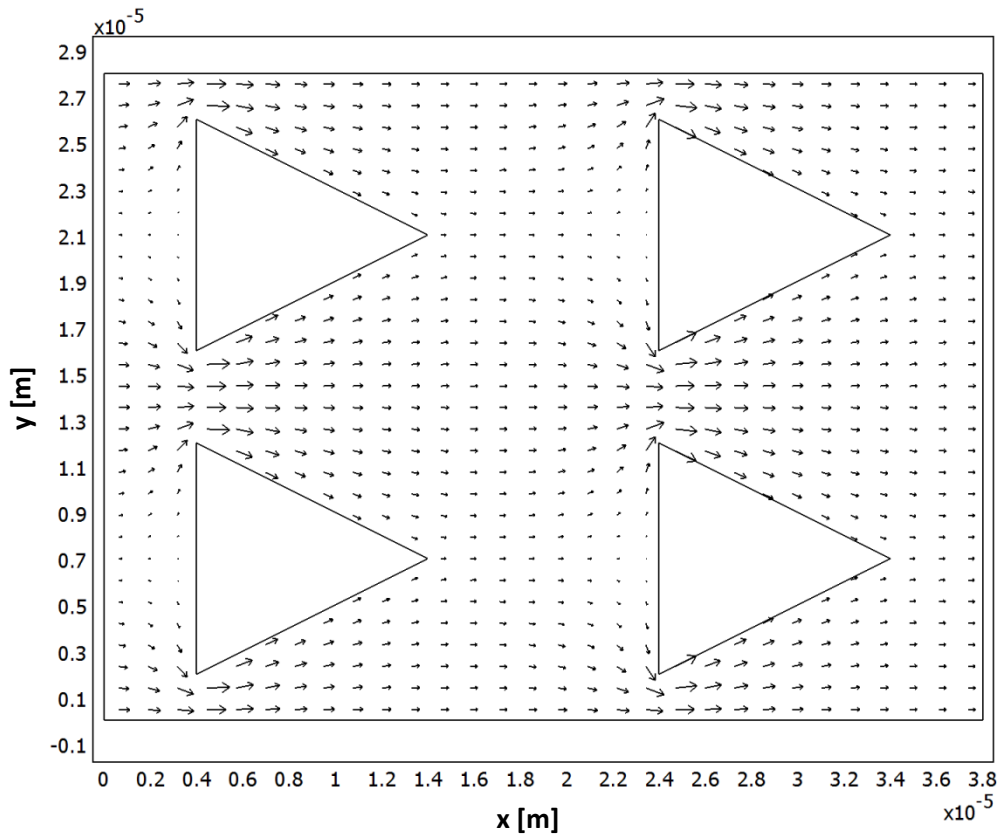


Figure 21: Electric field \vec{E}_U generated by U_U between the triangular posts structured in the microfluidic channel. Because the structures are non-conducting, the electric field lines are deformed and thus electric field gradients emerge which are required for dielectrophoretic forces.

can thus safely argue that the AC component of the electric field does not play a significant role when considering electrophoretic effects on the relevant timescale of several minutes. On the other hand, the time averaged dielectrophoretic force $\vec{F}_{DEP} = \frac{1}{2} \alpha \vec{\nabla} \vec{E}^2(\vec{r}, t)$ is proportional to

$$\alpha \vec{\nabla} \vec{E}_U^2(\vec{r}) \cdot \frac{U_{DC}^2 + U_{AC}^2}{U_U^2} = \alpha_p \vec{\nabla} \vec{E}_U^2(\vec{r}) \cdot \left(1 + \frac{U_{DC}^2}{U_{AC}^2} \right) \left(\frac{U_{AC}^2}{U_U^2} \right) \quad [4-1]$$

where $\vec{E}_U(\vec{r})$ is the electric field resulting from applying the unit voltage $U_U := 1V$ with valid electrostatic approximation which can be calculated via

$$\vec{E}(\vec{r}, t) = U(t) \frac{\vec{E}_u(\vec{r})}{U_U}.$$

For small U_{DC} compared to U_{AC} in equation [4-1], the impact of U_{DC} on the overall dielectrophoretic forces is evanescent as long as U_{AC} is high enough. During the experiments, this is the case, as U_{DC} is typically in the order of some volts while U_{AC} is chosen between 300 and 400 Volts. This justifies, that U_{DC} can be used to selectively control the electrophoretic motion and that U_{AC} controls the strength of dielectrophoretic traps.

The two induced forces $\vec{F}_{EP}(\vec{r}, t)$ and \vec{F}_{DEP} result in a combined potential landscape between the structured posts, theoretically evaluated in Figure 22 for the case of negative dielectrophoresis. The color coded potential function is characterized by several local minima and maxima which occur at locations where the electric field has an extremal value as well (cf. equation [2-19]). The polystyrene microspheres are attracted by the potential minima near the sharp tip on the right side of each post and by the flat wall on the left (marked as red circles). The tips on the upper side and on the lower side are potential maxima and thus repel the particles. The higher U_{AC} , the stronger are the field gradients and thus \vec{F}_{DEP} . In contrast, the higher U_{DC} , the stronger \vec{F}_{EP} , which helps the particles to escape from the dielectrophoretically created potential minima together with the stochastic forces (see paragraph 2.4.1.). In other words, it is possible to adjust the relation between U_{DC} and U_{AC} in a way, that the system is transporting microparticles (when U_{DC} is relatively high and U_{AC} is relatively low) or trapping microparticles (when U_{DC} is relatively low and U_{AC} is relatively high).

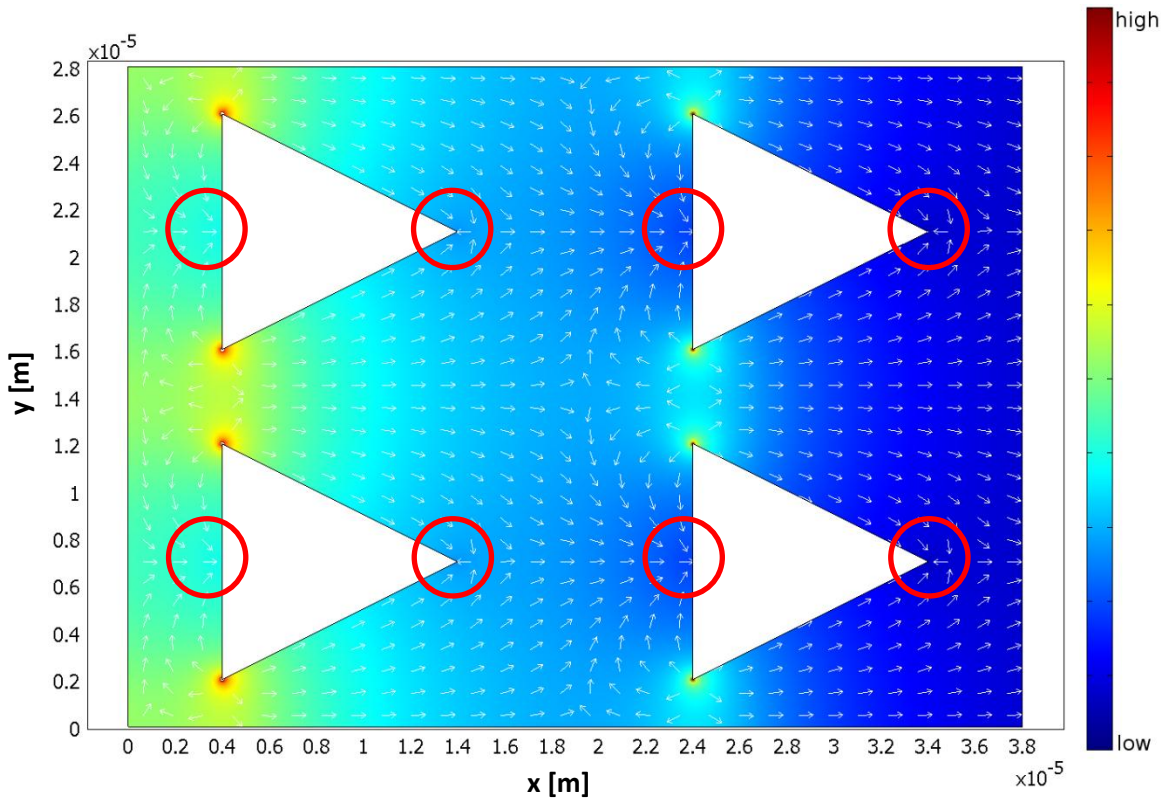


Figure 22: Effective potential (color code in arbitrary units) and resulting force exerted on a polystyrene particle (normalized vectors) flowing through the structured part of the microfluidic device. For the used polystyrene particles (negative dielectrophoresis) potential minima (marked red) can be found near the triangle's left flat wall and near the sharp tip on the right because here, the electric field strength has a minimum as well. Regions of high field strength on the other hand are potential maxima because the particles are repelled from such regions. When the relation between U_{AC} and U_{DC} is properly tuned, one can transport the microparticles through the post array or trap them at the potential minima as desired.

In general, the balance of U_{DC} and U_{AC} is dependent on the exact α_p and q^* values of the considered particles, because the dielectrophoretic force \vec{F}_{DEP} is proportional to α_p and the electrophoretic force \vec{F}_{EP} is proportional to the effective particle charge q^* . Consequently when multiple particle species with e.g. different diameters and hence different q^*/α_p are introduced into the system, the exact relation between U_{AC} and U_{DC} that traps or transports a certain particle species, is different (see Figure 23 showing the case $N = 3$ that was considered in the experiment). In the given parameter space spanned by U_{AC} and U_{DC} one can identify four different regimes A, B, C, and D. These regions represent four different states of the device concerning which particle species is trapped and which species migrates through the structure.

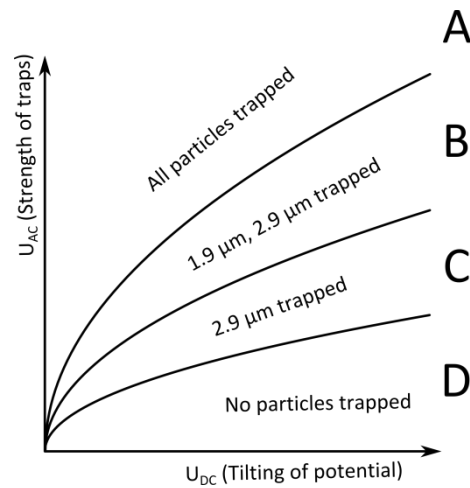


Figure 23: Parameter space spanned by U_{DC} which corresponds to the strength of the electrophoretic forces resulting in a tilting of the potential landscape and U_{AC} which corresponds to the strength of the dielectrophoretic traps. When U_{DC} is increased while U_{AC} is kept constant (horizontal movement to the right in the diagram), more and more different particle species start to escape from the traps and are transported. On the other hand, when U_{AC} is increased with constant U_{DC} (movement upwards in the diagram) more and more particle species are trapped. The letters A, B, C, and D mark regions where certain particle species in the experiment will be trapped or transported. The black lines (here for the exemplary case $N = 3$ particles realized in the experiment) mark those relations between U_{AC} and U_{DC} where the traps for some particles barely vanish. Thermal noise is not considered in this picture. If considered, the trapping times would be finite and approach zero exponentially when approaching a border. The plot is symmetric for negative U_{DC} and is thus not presented here. However, due to the asymmetric posts structured in the microchannel, there are slight deviations in the proportionality factor λ .

- A) All three particle species are trapped
- B) Only the two largest species ($\phi = 2.9 \mu\text{m}$ and $\phi = 1.9 \mu\text{m}$) are trapped. The smallest particles ($\phi = 1.1 \mu\text{m}$) are moving through the structure.
- C) Only the largest particle is trapped due to increasing U_{DC} . All other particles are moving through the structure.
- D) U_{DC} is so strong, that no particle species is trapped and all species are moving through the structure.

For increasing U_{DC} and constant U_{AC} more and more particle species are able to escape out of the traps in a short time and follow the electric field because the electrophoretic force is increased and the dielectrophoretic force generating the traps is kept constant. If U_{AC} is increased and U_{DC} is kept constant, the situation is vice versa.

Keeping in mind, that the dielectrophoretic force is proportional to $\alpha_p U_{AC}^2$ and that the electrophoretic force is proportional to $q^* U_{DC}$ the borderlines in Figure 23 are described by

$$U_{AC}^2 = \lambda \left| \frac{q^* U_{DC}}{\alpha_p} \right|.$$

λ is a proportionality constant depending e.g. on the exact shape of the microstructure, the sign of α_p , or the sign of U_{DC} in the case of asymmetric structures like here. Otherwise, λ is independent of q^* , α_p , U_{DC} , and U_{AC} . The equation further reveals that the relation q^*/α_p is the important separation criterion in this microfluidic device. Hence, only particles with different q^*/α_p can be separated. However, thermal effects are not accounted for in this equation.

With this framework being developed, it is now possible to envision a voltage protocol to induce separation that serially addresses the different system states where m particles are moving and $N - m$ particles are trapped for a certain period Δt_m . Before a special protocol for the case $N = 3$ species (considered in the experiment) is developed, a general case of arbitrary N is investigated.

As already mentioned, the main separation goal is to move every particle species $k \in \{1, \dots, N\}$ a certain and unrivaled effective multiple Δx_k of the lattice constant in (positive or negative) x direction. The voltage protocol generally requires not more than $N + 1$ time intervals of length Δt_m with properly tuned and during one timestep constant U_{AC}^m and U_{DC}^m . As a result, the average species specific migration velocity is

$$v_x^k = \frac{x(t=0) - x(t=t_s)}{t_s} \quad [4-2]$$

where $t_s = \sum_{m=0}^N \Delta t_m$ is the duration of one realization of the complete voltage protocol. The species index k is now chosen (without loss of generality) in a way that the particles with $k \leq m$ are moving during the time interval m and those with $k > m$ are trapped. In other words, a certain particle species k is moving whenever $m \geq k$ and trapped whenever $m < k$. As a consequence k increases with decreasing q^*/α_p (and thus better polarizable particles).

At first, the best polarizable particle species $k = N$ is considered and the voltage protocol is thus constructed backwards in time. It is only moving during the last time interval $m = N$. During this interval $U_{AC}^{(N)}$ and $U_{DC}^{(N)}$ must be chosen in a way, that this species $k = N$ is able to move and cover the distance Δx_N . However, all the other particle species $k < N$ are moving as well during this time step because they have a higher q^*/α_p and thus cover the

distances δx_k . After Δt_N the voltages $U_{DC}^{(N-1)}$ and $U_{AC}^{(N-1)}$ are set for a new time interval with Δt_{N-1} . Now $U_{AC}^{(N-1)}$ is chosen a little higher than $U_{AC}^{(N)}$ to keep particle $k = N$ trapped but still allowing all the other particles to move and $U_{DC}^{(N-1)}$ is reversed. The total displacement of particle N is thus only Δx_N . In this next step, the particles $k \in \{1, \dots, N - 1\}$ have to exhibit displacements of $\Delta x'_m = \Delta x_m - \delta_m$. In the same way, the parameters for $m = N - 2, N - 3, \dots, 1$ can be set.

Note that when a separation task with sieving characteristic is desired (particles with adjacent k values are grouped and thus urged to move into the same direction) the required protocol may be simplified. Thus, fewer steps are needed than required by the theoretically introduced prototype because the relevant particles species can be considered as one. N is therefore decimated accordingly. The timestep Δt_0 where all particles are trapped and no species is moving seems to be a theoretical artifact without use in the experiment. However, it turned out, that it is helpful to include this timestep into the final protocol. It guarantees that the system is in a well-defined state because all particles are trapped when the procedure is repeated. After the whole set of time steps Δt_m for all m is completed, the protocol may be repeated for further spatial separation. In practice, there are various deviations from this optimal scheme because of disturbing influences. It is e.g. unavoidable, that different particle species and even sometimes particles from the same type show slightly different electrophoretic mobilities.

The experimental proof of this separation principle is carried out with $N = 3$ different particles ($\phi=2.9 \mu\text{m}$, $\phi=1.9 \mu\text{m}$, and $\phi=1.1 \mu\text{m}$). The required protocol is illustrated in Figure 24 and explicitly formulated in terms of the required voltage arrangements in Table 5 for the three possible scenarios. Protocol a) is the exact reproduction of the theoretically proposed principle. In a first step, U_{AC} is set to a high value and U_{DC} is switched off to set the system to a well-defined state for 10 seconds where all particles are trapped. Now U_{DC} is switched on to 15 V while U_{AC} is kept constant and only the smallest 1.1 μm particles (black) are moved by electrophoresis in negative x direction. After 90 seconds, U_{AC} is lowered to 320 V to additionally release the middle-sized 1.9 μm particles (red). The polarity of U_{DC} is reversed, because the 1.9 μm particles must be transported to the opposite direction than the 1.1 μm particles. The last step transports all particles back to the left as the sign of U_{DC} is changed again and U_{AC} is switched off. The result is, that the smallest and the largest particles were transported to the left while the remaining middle sized particles were transported to the right (see last row of Figure 24).

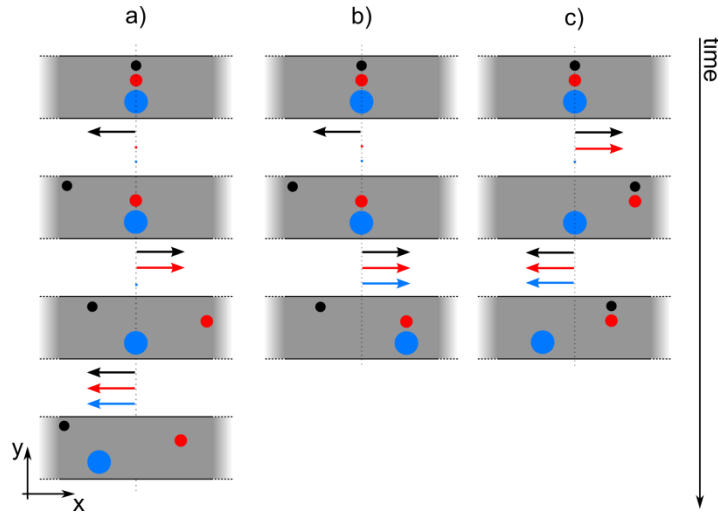


Figure 24: Scheme of the separation protocol for $N = 3$ different particle species with diameters of $1.1 \mu\text{m}$ (black), $1.9 \mu\text{m}$ (red), and $2.9 \mu\text{m}$ (blue). Protocol a) separates the $1.9 \mu\text{m}$ particles from the remaining particles. Protocol b) isolates the smallest particles from the other two species and protocol c) is used to move the biggest particles into opposite directions than the remaining two species. Case a) is the most complicated case because it does not introduce a sieving characteristic like b) and c) but extracts particles that are centrally located in the q^*/α space out of the mixture. Therefore, all theoretically recommended $N + 1$ protocol steps are required. When applying protocols b) or c) it is possible to treat two particle species as one which are the two largest particles in b) and the two smallest particle species in c). Hence, protocols b) and c) are one step shorter than a).

Protocol b) is used to consider a simpler case. Here the system operates with sieving characteristics as it lets the smallest $1.1 \mu\text{m}$ particles move to the left and the remaining species to the right. Again, the first step is a 10 second phase of high U_{AC} without U_{DC} to set the system to a defined state. Now the smallest particles are being transported to the right. Subsequently all particles are released and transported into the opposite direction. Protocol c) operates analogous to b) with the exception that the two smallest particle species with $1.1 \mu\text{m}$ and $1.9 \mu\text{m}$ diameters are transported together in the first step.

Table 5: Voltage protocols for the experimental separation of three different particle species. While protocol a) extracts the medium-sized $1.9 \mu\text{m}$ particles from the other species, the protocols b) and c) have sieving characteristics and extract the smallest $1.1 \mu\text{m}$ particles (b) and the largest $2.9 \mu\text{m}$ particles (c) from the remaining species. The values were roughly prospected theoretically but fine-tuned in the experiment. The protocol may be repeated several times for a better result.

a)			b)			c)		
Δt_m	U_{DC}	U_{AC}	Δt_m	U_{DC}	U_{AC}	Δt_m	U_{DC}	U_{AC}
10	0	400	10	0	400	10	0	400
90	15	400	40	15	360	50	-15	320
25	-16	330	12	-10	0	12	10	0
10	10	0						

Several mechanisms that induce peak broadening and thus lower the separation resolution are present. First of all, thermal fluctuations are prominent at the given order of magnitude. They play an important role during the particle transportation as they intrinsically induce peak broadening according to the diffusion equation.

Secondly, they influence the escape process of particles out of dielectrophoretic traps as well. While for low temperatures, U_{AC}^m could be sufficient to safely trap a certain particle species for a certain amount of time, thermal noise will support the (unwanted) escape process during the same amount of time for larger temperatures. This behavior is the key ingredient for an effect termed *diffusion enhancement* so far observed theoretically and in experiments¹⁷⁵⁻¹⁷⁷. A periodic potential (created here by the dielectrophoretic traps) has to be tilted (done here via electrophoretic forces). At some point the tilting becomes critical. In other words thermal escape processes out of the traps are supported by the tilting of the potential in a way, that the slightest thermal kick is sufficient for a successful surmounting of the potential barriers. This effectively leads to a (quite convincing) increase of the effective diffusion coefficients and thus the peak broadening is increased. Slight imperfections in the regularity of the potential periodicity (like typical imperfections due to soft lithography) may further boost the effect¹⁷⁸. On the other hand, Brownian motion enables the functionality of the device. Without diffusion, particles that are located exactly at a triangle's right tip would in theory hit the flat wall of the next triangle when transported in positive x direction. Consequently, as there is no force acting in y-direction, the particles would be trapped there forever.

A third reason for undesired band broadening corresponds to the previously mentioned diffusion enhancement. Although the particles can be regarded as massless and therefore inertia free, there are sometimes certain transition times before a particle adapts to the updated voltages. This is sometimes the case when switched from trapped to moving because it might still collide with a post's wall before it is migrating freely due to the finite size of the traps.

4.1.2 EXPERIMENTAL SEPARATION OF THREE PARTICLES SPECIES

The voltage protocol that is defined in Table 5 is now used to experimentally test the proposed separation principle in detail. The objective is to separate $N = 3$ species of polystyrene particles with different diameters (2.9 μm , 1.9 μm , and 1.1 μm) and thus

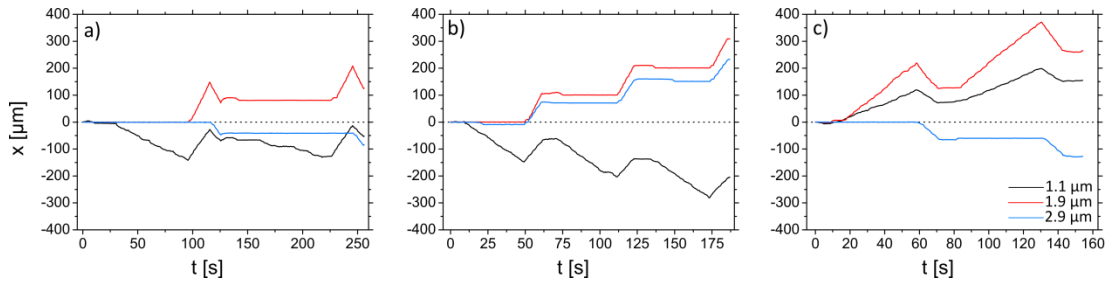


Figure 25: The experimental trajectories of three different polystyrene beads (1.1 μm black, 1.9 μm red, and 2.9 μm blue) for at least two periods the corresponding separation protocol a), b), or c). In a), the middle-sized 1.9 μm particles are effectively moving into positive x direction while the remaining 1.1 μm and 2.9 μm move with negative effective velocity in x direction. Further repetitions of the protocol will further separate the particles. In b) the system has been set to sieving mode and the smallest 1.1 μm particles are separated from the middle-sized 1.9 μm particles and the largest 2.9 μm particles. The third trajectory set in c) illustrates how the microfluidic device separates the largest 2.9 μm particles from the remaining 1.9 μm and 1.1 μm beads. Note that only a change in the applied voltage protocol (see Table 5) is sufficient to radically change the separation behavior.

different q^*/α_p values and to realize all three imaginable separation modes (see Figure 24). As already stated, no change to the system itself with the exception of the applied voltage protocol is required to change the selectivity.

In Figure 25, exemplary experimental single particle trajectories are presented with at least two periods of the voltage protocol for all three possible separation modes. As prospected, applying protocol a) (see Table 5) causes the middle-sized 1.9 μm bead (red) to effectively migrate with a positive velocity in x direction while the remaining 1.1 μm (black) and 2.9 μm particles (blue) show a negative effective velocity in that direction. A quick change to protocol b) modifies the separation behavior instantly. Now the device operates in sieving mode and isolates the smallest 1.1 μm particle which migrates with effective negative velocity through the structure. The 1.9 μm and the 2.9 μm particle travel with positive effective velocity. Finally protocol c) separates the largest 2.9 μm particle from the other two by letting it move with negative velocity in x direction while the other two species migrate with positive velocity.

As already mentioned, once in a while slight imperfections can be observed in some trajectories, e.g. in the behavior of the 1.1 μm particles (black) in Figure 25 a) and b). For example around $t = 100$ s in Figure 25 b) the 1.1 μm particle heavily interacted with one of the posts and got stuck for a moment because of geometric reasons. Hence, the trajectory proceeds horizontally for an instance ($v_x = 0$ $\mu\text{m}/\text{s}$) which leads to deviations in the mean particle velocities. Figure 25 a) shows quite similar disturbances of the 1.1 μm particle between 125 s $< t < 200$ s. Here the mean velocity in x direction is smaller than in the driving period before (10 s $< t < 100$ s) because of undesired interactions with the

Table 6: Mean velocities and standard deviations of an ensemble of 100 particles per species for the three separation protocols a), b), and c).

Protocol	a)	b)	c)
1.1 μm	$-0.27 \pm 0.26 \mu\text{m/s}$	$-1.28 \pm 0.27 \mu\text{m/s}$	$+1.10 \pm 0.20 \mu\text{m/s}$
1.9 μm	$+0.45 \pm 0.24 \mu\text{m/s}$	$+1.51 \pm 0.83 \mu\text{m/s}$	$+1.69 \pm 0.41 \mu\text{m/s}$
2.9 μm	$-0.24 \pm 0.17 \mu\text{m/s}$	$+1.21 \pm 0.38 \mu\text{m/s}$	$-0.68 \pm 0.20 \mu\text{m/s}$

structure. Transient effects can be observed as well, e.g. in Figure 25 c). Here, the 2.9 μm particle (blue) needs some additional time after the driving direction changed to adapt to the new conditions.

All these effects broaden the statistic distributions for the mean velocities of a reference ensemble for each driving protocol which are illustrated in Figure 26 and summed up in Table 6. To generate the histograms, trajectories of 100 particles per species and protocol were considered by evaluating their mean experimental velocities over one driving period according to equation [4-2]. Figure 26 a) depicts the results for the isolation of the middle-sized 1.9 μm particles. As one could already suspect from the single particle trajectories in Figure 25, the 1.9 μm particle ensemble is migrating on average with positive velocity while the distributions for the remaining species have their center in the region of negative velocities. However, very few particles were transported in the wrong direction although with quite low speeds. This could be an artifact, because the peak broadening (proportional to \sqrt{t}) dominates over the covered transport distance (proportional to t) for short running times. The velocity distributions in Figure 26 b) are considerably better distinguishable although there are still very few particles that travel in the wrong direction. The best result

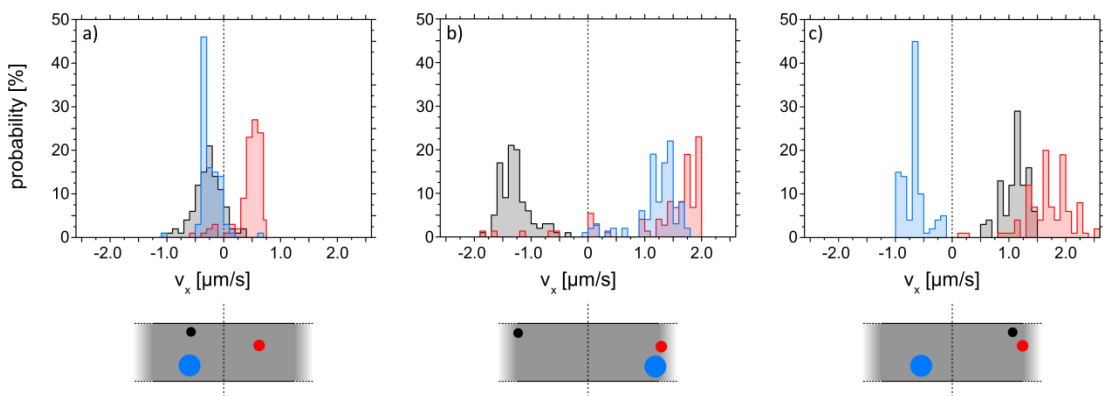


Figure 26: Experimental ensemble mean velocities of the three different modes of separation discussed in Figure 25. 100 trajectories of each species per case were analyzed after one period of the corresponding voltage protocol (see Table 5). The sketches in the lower part illustrate schematically the desired outcome of the separation procedure for clarification.

is obtained for the isolation of the 2.9 μm particles in Figure 26 c) because not a single particle is transported in the wrong direction and hence no wrong particle classification was observed.

The field of view of the available microscopy equipment is limited. Consequently a simultaneous observation of all particles for more than one or two periods of the driving protocol is impossible which is, however, required to investigate the possibly time dependent spatial resolution of the separations, defined here as

$$R = \left(\frac{\bar{x}_a - \bar{x}_b}{\sigma_a + \sigma_b} \right). \quad [4-3]$$

\bar{x}_a and \bar{x}_b are the mean positions for the two considered particle distributions and σ_a and σ_b represent the corresponding standard deviations. Nevertheless it is possible to extract the required data of a long time observation of up to 100 driving periods out of the experimental velocity histograms. For this purpose, random velocities with the same distributions as printed in Figure 26 were generated. With this data, 100 trajectories per species were calculated by repeatedly assigning a random velocity out of the distribution to a particle and calculating its new position. With this data at hand, spatial distributions that represent particle positions after 1, 3, 5, and 100 driving periods for all three separation protocols a), b), and c) are extrapolated (see Figure 27).

While only the isolation of the 2.9 μm particles in c) leads to baseline resolution after just one single period, the other two results are distinguishable but not well resolved. However, the separation performance increases when the protocol is repeated. After only five realizations all three separation schemes show baseline resolution regarding the isolated species and the nearest remaining particle type. After 100 repetitions of the voltage protocol the three particle types are macroscopically separated from each other and at least two separation schemes (b and c) lead to a splitting of the remaining two species.

The data presented in Figure 27 suggests that the spatial resolution of the separation is time dependent. If the protocol is repeated more often, the achieved resolution seems to increase. This hypothesis is supported by Figure 28. Spatial resolutions between the three possible combinations of particle types were calculated according to equation [4-3] from the extrapolated datasets which are partially illustrated in Figure 27. All results in the double logarithmic plots are highly proportional to \sqrt{t} which seems plausible with the

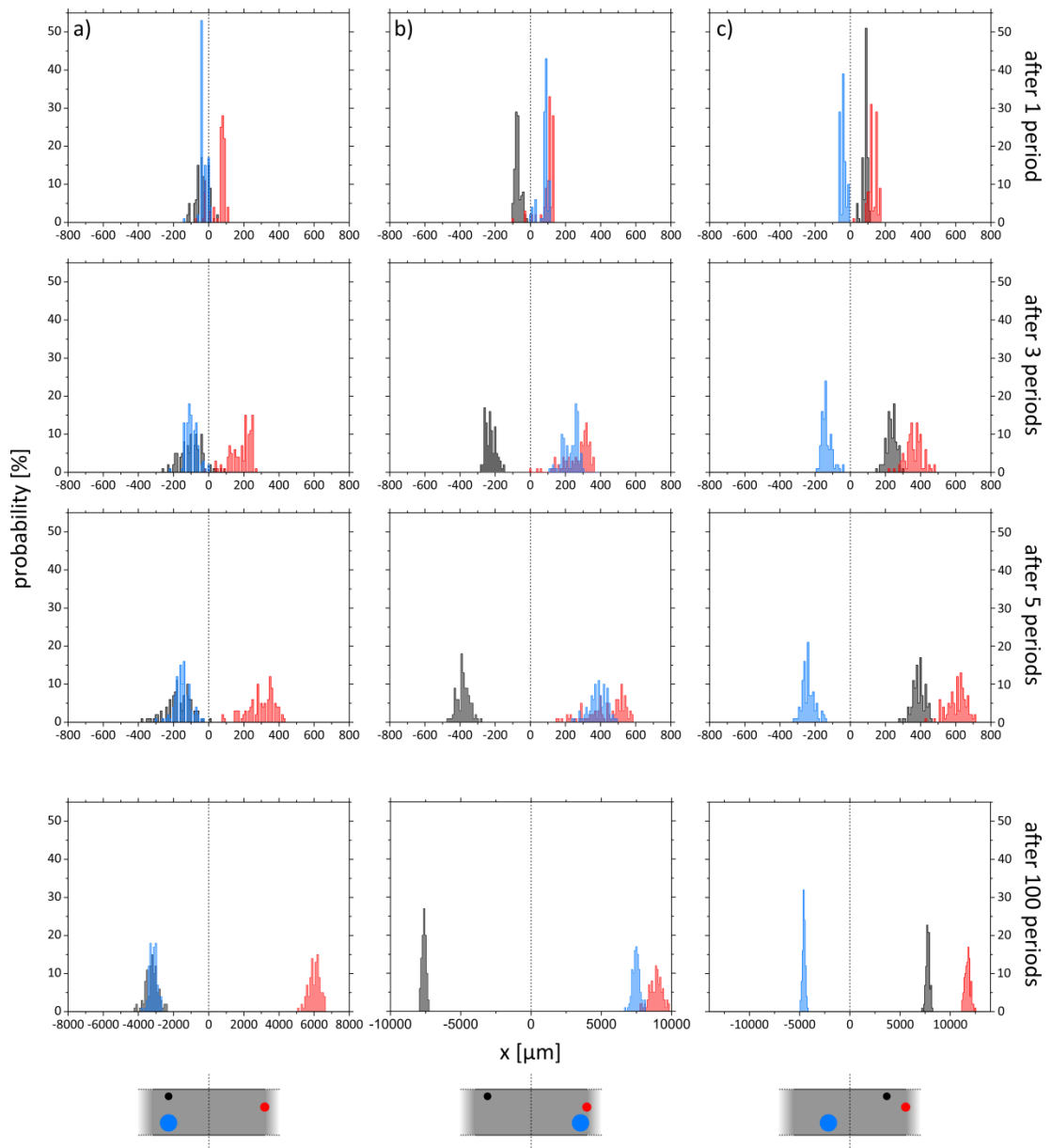


Figure 27: Extrapolated spatial distributions of an ensemble of 100 microparticles after 1, 3, 5, and 100 driving periods for all three separation protocols a), b), and c). In general, it can be observed, that the sometimes occurring wrong classifications of some microparticles does not play a significant role when more than five driving periods of the separation protocols are performed. After 100 periods, the particles are macroscopically well distinguishable as well. In two cases, even the two species that travel into the same direction are resolvable. Note the different scaling of the x axis in the plots that illustrate the particle distributions after 100 driving periods.

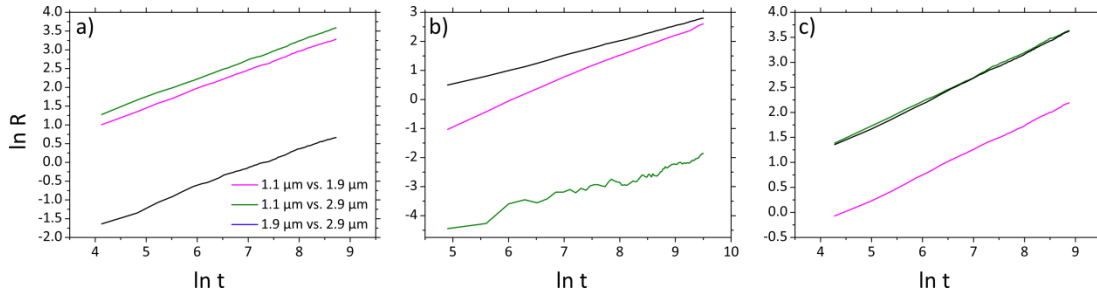


Figure 28: Temporal characteristics of the achieved spatial resolution with the discussed voltage protocols a), b) and c) plotted double logarithmic and averaged over 1000 trajectories. The three curves in each diagram represent the three possible particle combinations between which the resolutions were calculated according to equation [4-3]. A time dependence of the resolution which is proportional to \sqrt{t} is notable.

following consideration. The numerator $\bar{x}_a - \bar{x}_b$ in equation [4-3] is proportional to t . Further assuming, that the observed peak broadening represented by $\sigma_a + \sigma_b$ is of diffusive nature and thus proportional to \sqrt{t} leads to

$$R = \left(\frac{\bar{x}_a - \bar{x}_b}{\sigma_a + \sigma_b} \right) \propto \frac{t}{\sqrt{t}} = \sqrt{t}$$

which reproduces the character of the resolution functions in Figure 28. The discussed disturbing effects (Brownian motion, diffusion enhancement and transient effects, see paragraph 4.1.1) dominate for short running times as they are proportional to \sqrt{t} in comparison to the transportation of particles being proportional to t . The comparison furthermore shows, that different electrophoretic mobilities of particles belonging to the same species do not significantly broaden the peaks, as such effects would be proportional to t and not to \sqrt{t} .

4.1.3 EXPANSION OF THE PRINCIPLE TO MORE THAN 3 SPECIES

It has been stated in paragraph 4.1.1, that the separation principle behind the just discussed experiment with three particle species can be extended to N different particle types. A theoretical example with exemplary single particle trajectories and ensemble results for 100 particles per species for the case $N = 5$ is illustrated in Figure 29. These simulations are a generous contribution from Dr. Ralf Eichhorn (Nordic Institute for Theoretical Physics (NORDITA)) at the Royal Institute of Technology and Stockholm University, Sweden) and based on the experimental findings from the previous chapter. The numerical procedure is analogous to the approach in paragraph 3.5 and technical details can be found in¹⁷⁹. The most difficult three separation modes a), b), and c) are

demonstrated. At first, in a) it is validated, that the middle sized $2.0\ \mu\text{m}$ particles can be efficiently extracted out of the remaining species and consequently move into the opposite direction. In b) the largest and the smallest species ($1.0\ \mu\text{m}$ and $3.0\ \mu\text{m}$) are isolated from the other particles and effectively travel with negative velocity in x direction while the other particles move into the opposite direction. Finally the separation protocol c) lets the particles alternatingly move to the left and to the right so that the $1.0\ \mu\text{m}$, the $2.0\ \mu\text{m}$, and the $3.0\ \mu\text{m}$ particles effectively move to the left and the $1.5\ \mu\text{m}$ and the $2.5\ \mu\text{m}$ beads are finally transported to the right. This separation mode is exactly derived according to the original full protocol proposed in paragraph 4.1.1. The appropriate voltage protocols to achieve the illustrated results are provided in Table 7.

The key parameters for the simulations are suitable particle diffusion coefficients which are calculated using equation [2-21] and polarizabilities obtained via equation [2-17]. The effective particle charge is assumed to be proportional to their size because the overall electrophoretic velocity of all particles should be identically $6\ \mu\text{m/s}$ at $U_{DC} = 10\ \text{V}$. The

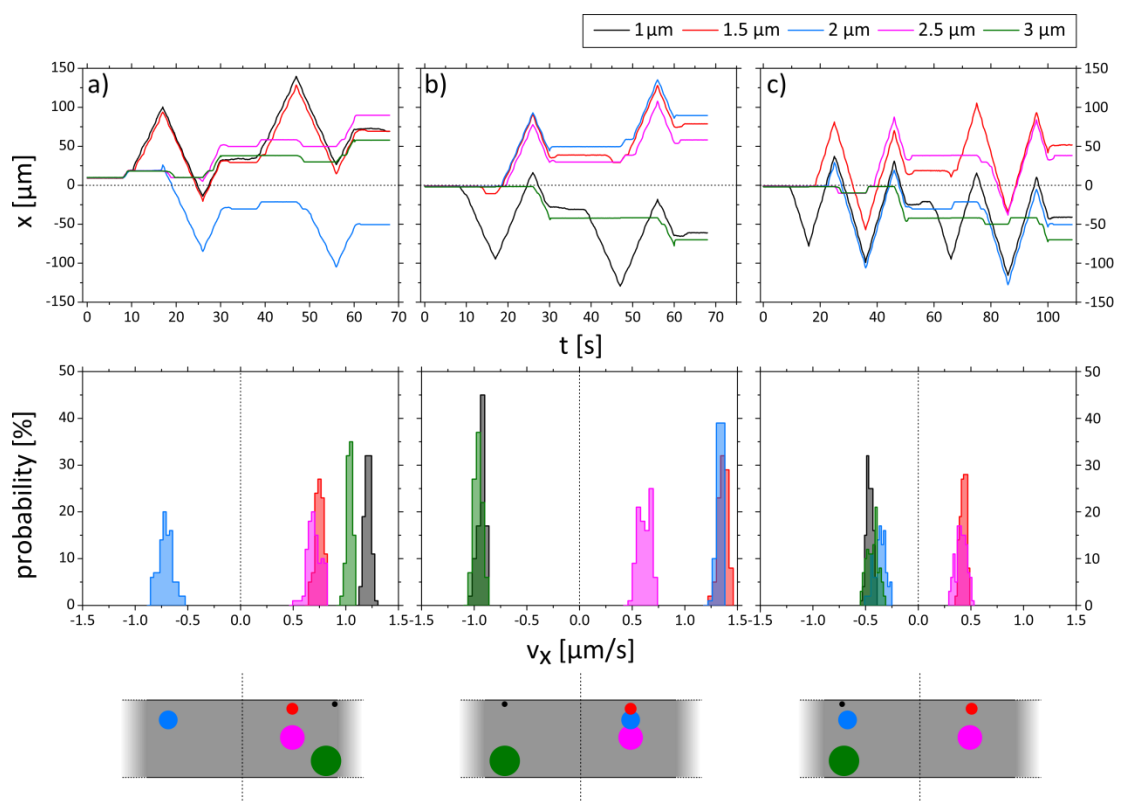


Figure 29: Exemplary single particle trajectories and ensemble velocity results for 100 particles per particle species and separation mode after one period. Here, five different particle species ($1.0\ \mu\text{m}$ (black), $1.5\ \mu\text{m}$ (red), $2.0\ \mu\text{m}$ (blue), $2.5\ \mu\text{m}$ (magenta), and $3.0\ \mu\text{m}$ (green)) in three different modes were considered: a) extraction of the middle sized blue $2.0\ \mu\text{m}$ particles, b) moving the largest green $3.0\ \mu\text{m}$ particles into opposite direction than the remaining species and c) the migration of every second particle species ($1\ \mu\text{m}$, $2\ \mu\text{m}$, and $3\ \mu\text{m}$) to the left while the $1.5\ \mu\text{m}$ and the $2.5\ \mu\text{m}$ particles move to the right.

Table 7: Voltage protocols a) b), and c) for the simulated separation of five different particle species as shown in Figure 29. Protocols a) and b) have less steps than protocol c) because some particles were again grouped together (sieving characteristics).

a)			b)			c)		
Δt_m	U_{DC}	U_{AC}	Δt_m	U_{DC}	U_{AC}	Δt_m	U_{DC}	U_{AC}
8	0	1000	8	0	1000	8.5	0	1000
9	20	530	9	-20	910	7.5	-20	910
9	-20	490	9	+20	350	9	+20	530
4	+19	0	4	-20	0	11	-20	490
						10	+20	350
						4	-20	0

resulting parameters are summarized in Table 7. The data in Figure 29 impressively shows, that it is generally possible to expand the experimentally demonstrated separation principle to higher N as not a single particle has ever been effectively transported into the wrong direction and all the relevant distributions are well baseline separated.

As motivated in paragraph 4.1.1 the underlying generic principle can be extended to arbitrary N with different q^*/α_p values. However, when the involved particles exhibit too small $\Delta(q^*/\alpha_p) = \left| q_i^*/\alpha_{p_i} - q_{i+1}^*/\alpha_{p_{i+1}} \right|$, the resolution of the separation will suffer as well. Critical $\Delta(q^*/\alpha_p)$ in particular compete with the already mentioned disturbing effects. This is especially the case when the difference between the dielectrophoretic energy barrier that holds particle species i trapped and the energy barrier that holds particle species $i + 1$ trapped is comparable to the thermal energy $k_B T$, hence $|\Delta\Psi_{K_i} - \Delta\Psi_{K_{i+1}}| \approx k_B T$.

Table 8: Particle parameters used for the theoretical consideration of the separation of $N = 5$ particles discussed in Figure 29.

Particle Diameter [μm]	Charge q^* [10^{-15} C]	Polarizability α_p [10^{-28} Fm ²]	Diffusion coefficient D [$\mu\text{m}^2/\text{s}$]
1	-0.22	-5.6	0.25
1.5	-0.33	-18.8	0.16
2	-0.44	-44.5	0.12
2.5	-0.55	-86.9	0.099
3	-0.66	-150	0.082

4.1.4 SUMMARY

In summary, a microfluidic ratchet device has been developed that is able to separate N different particle species with an elaborate scheme of dynamically changeable voltage protocols triggering trapping as well as transportation of the analyte particles. The utilized subtle competition between electrophoretic and dielectrophoretic forces does not only lead to spatial particle separation but also effectively steers the desired particle classes to extract into opposite direction than the remaining species. Unlike standard biotechnological separation equipment like e.g. gel electrophoresis, the separation criterion is not statically implemented in the system. Consequently the choice of the particles to extract can be easily changed instantly just by applying a different voltage pulse scheme.

This generic principle has been experimentally demonstrated for $N = 3$ particles types with different q^*/α_p values and expanded theoretically to $N = 5$ based on the experimentally gained data. Although slight modifications to the microfluidic structure design might be required to tune the dielectrophoretic traps, the separation concept itself is generically applicable to any charged and polarizable (bio-) particle class, like DNA, cells, or proteins. Their dielectrophoretic addressability was proven in various experimental studies (for a review see e.g.⁶⁰).

4.2 AUTOMATED QUANTIFICATION OF SINGLE MOLECULE POLARIZABILITY

The term *dielectrophoresis* was first defined by Pohl in the 1950s and refers to the motion of a polarizable but effectively uncharged object in an inhomogeneous electric field due to polarization effects⁵⁸. Many microfluidic devices (like the one

Results discussed in this section have been published in: J. Regtmeier, R. Eichhorn, L. Bogunovic, A. Ros & D. Anselmetti: *Dielectrophoretic trapping and polarizability of DNA: The role of spatial conformation*, *Analytical Chemistry* 82 (2010), 7141-7149

developed in section 4.1) are based on dielectrophoresis, which can nowadays be considered as a very well established standard technology to immobilize, sort, or manipulate a given sample without any labeling. For this purpose the required electric field gradient is typically either induced by metallic electrodes (electrode based dielectrophoresis) or by obstacles, posts or constrictions made from an insulating material with external electrodes (electrode less dielectrophoresis) inside a microfluidic device^{21,60,63,162-164}.

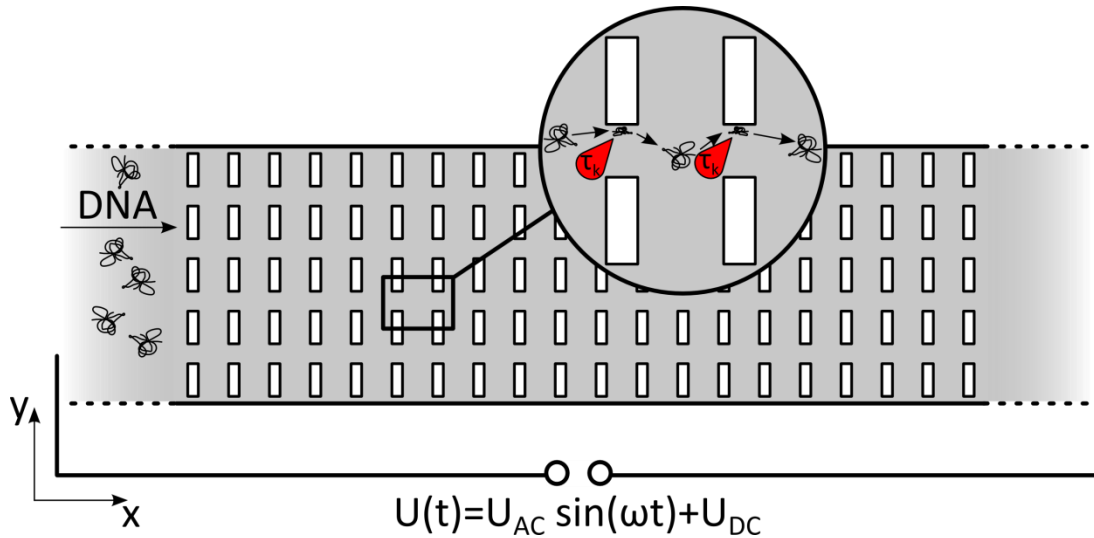


Figure 30: Schematic operation principle of the microfluidic approach (not to scale) to measure the polarizability of large macromolecules via dielectrophoretic trapping^{177,82}. A small ensemble of analyte molecules (here DNA) is injected into a microfluidic channel with an inherent regular array of rectangular posts and an alternating voltage $U_{AC} \sin(\omega t)$ biased by U_{DC} is applied. Because the posts are non-conducting, electric field gradients are generated in between resulting in dielectrophoretic traps and thus local potential minima induced mainly by U_{AC} . Consequently DNA molecules transported by U_{DC} will be trapped between the posts for a certain time τ_K until they are able to escape due to the random influence of thermal motion. Because the strength of the dielectrophoretic traps depends on the molecules' polarizabilities.

The key parameter for dielectrophoretic experiments is the single molecule polarizability α_p of a given sample which is typically only addressable via macroscopic ensemble methods like transient electric birefringence^{180,181}, conductivity dispersion¹⁸², or time domain reflectometry¹⁸³ measurements. Therefore, it usually remains unknown and appropriate electric fields have to be chosen via trial and error methods. However, automated, fast and high throughput methods for polarizability measurements of small molecular ensembles would be a very helpful tool not solely for basic researchers but also in commercially available microfluidic products e.g. for automated flexible adaption of DEP-devices (like the one described in section 4.1) to a given sample class.

In the present section, a very versatile microfluidic approach whose basic features were developed by Jan Regtmeier, Thanh Tu Duong, and Ralf Eichhorn in our workgroup before, is extended to be a fully automated and large throughput method to estimate the polarizability of very small DNA molecule ensembles^{177,82}. The very basic experimental principle is illustrated in Figure 30. A small ensemble of DNA molecules is injected into a channel structured with an array of rectangular non-conducting posts. Upon applying an electric voltage $U(t) = U_{DC} + U_{AC} \sin(\omega t)$, the DNA molecules are transported by electrophoresis due to U_{DC} and potential wells between the posts are caused by dielectro-

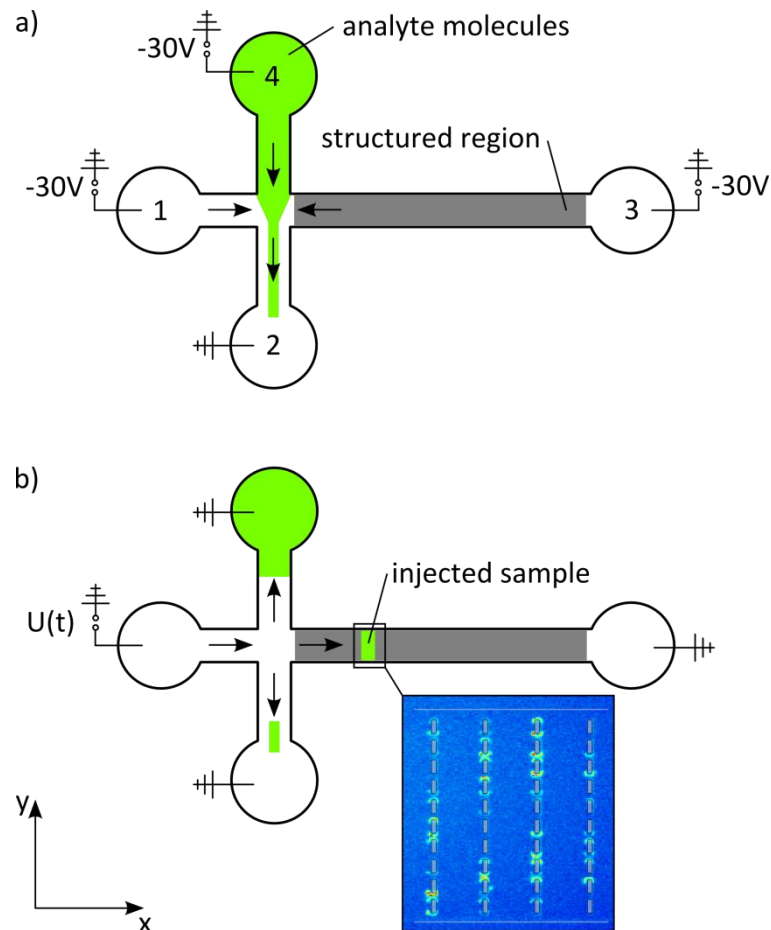


Figure 31: Schematic of the microfluidic device for polarizability quantification (not to scale). A typical cross injector is connected to the structured analysis channel (grey area) and fluid reservoirs are located at every channel inlet. All four channels are $6\ \mu\text{m}$ high. The injector channels 1, 2, and 4 are each 2mm long and $95\ \mu\text{m}$ wide except channel 1 which is $100\ \mu\text{m}$ wide. The analysis channel 3, where the actual experiment is carried out is 5mm long and $100\ \mu\text{m}$ wide as well. It is structured with 180 columns (lattice constant in x direction: $21\ \mu\text{m}$) of $2.2\ \mu\text{m} \times 7.4\ \mu\text{m}$ sized non-conducting posts reaching over the whole range of $6\ \mu\text{m}$ in z direction. The gap in y direction between these posts, where the dielectrophoretic traps are generated, is $2.3\ \mu\text{m}$ wide. The structured area starts $100\ \mu\text{m}$ away from the channel cross. The system can be set to two modes of operation for the pinched injection of the analyte molecules (marked in green). In a), constant voltages are applied to the reservoirs via platinum electrodes to let the sample flow through the injector channel to the waste reservoir 2. During this process, the stream is focused at the channel crossing. After some time, the system is set to b). Now all reservoirs are grounded except for channel 1. Here $U(t)$ is applied, injecting a small DNA ensemble into the analysis channel and providing the electric fields for dielectrophoretic trapping.

phoresis mainly triggered by U_{AC} . After a molecule was trapped in such a local potential minimum, whose depth is dependent on the particle's polarizability, it is on average able to escape again due to thermal noise after some time τ_K (see paragraph 2.4.1). Somehow measuring this average trapping time τ_K thus yields single molecule polarizabilities, as explained in paragraph 4.2.1.

The corresponding microfluidic device is illustrated in Figure 31, consisting of a standard cross injector to perform pinched injection (channels 1, 2, and 4) and an analysis channel 3

containing the required structured post array. The reservoirs at the end of each channel are equipped with platinum electrodes to apply a certain voltage protocol to the system to achieve injection and analysis in two subsequent steps. Figure 31 a) shows the system in its initial state. Analyte molecules (here DNA, illustrated in green) are filled into reservoir 4 while the remaining reservoirs are filled with the corresponding buffer solution (see section 3.3). While the waste reservoir 2 is grounded, all remaining reservoirs are set to -30V. Consequently, the negatively charged DNA is transported towards the waste reservoir and focused at the intersection. The experiment is commenced by grounding reservoirs 2, 3, and 4 and applying $U(t)$ to reservoir 1 (see Figure 31 b) and thus injecting a small DNA portion into the analysis channel and recording its behavior via video fluorescence microscopy.

The present section deals with a method to obtain single molecule polarizabilities in an automated way. Paragraph 4.2.1 describes the developed experimental procedure in detail. To evaluate this method, the scaling of the polarizability in dependence of the ionic surrounding is quantified for 12.2 kbp and 48.5 kbp double stranded DNA and compared to the known scaling behavior in paragraph 4.2.2. A potential drawback of the presented method might be the constraint to employ fluorescent straining. Therefore, its influence on the polarizability measurements of DNA is investigated in paragraph 4.2.3 followed by concluding remarks in paragraph 4.2.4.

4.2.1 AUTOMATED ANALYSIS OF SINGLE MOLECULE DNA POLARIZABILITY

When an electric voltage signal

$$U(t) = U_{AC} \cdot \sin(\omega t) + U_{DC}$$

with $\omega/2\pi = 60\text{Hz}$ and $U_{DC} = 12\text{V}$ is applied to the considered microfluidic system (see Figure 31) an electric field distribution

$$\vec{E}(\vec{r}, t) = \vec{E}_{DC}(\vec{r}) + \vec{E}_{AC}(\vec{r}) \cdot \sin(\omega t)$$

is the consequence, which is depicted in Figure 32. In such a system, a charged and polarizable macromolecule or (bio-) particle will be subjected to a potential landscape induced by three different effects. First of all, the electric field gradients emerging in the

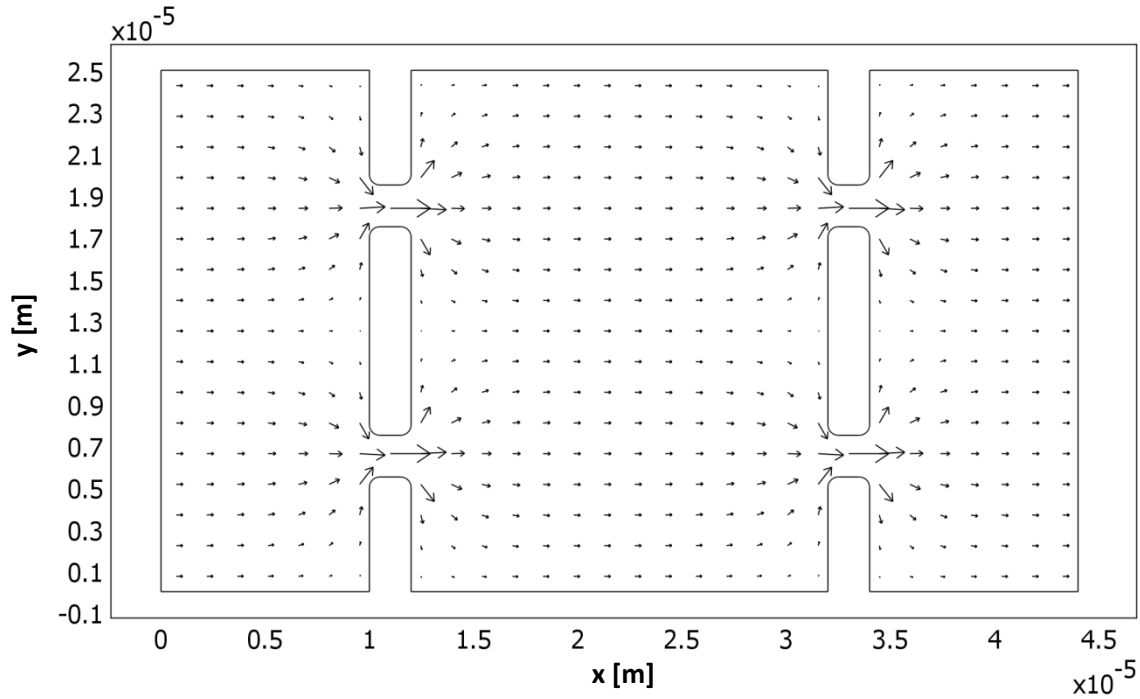


Figure 32: Electric field \vec{E} generated by $U(t)$ between the rectangular posts structured in the microfluidic channel. Because the structures are non-conducting, the electric field lines are deformed and electric field gradients emerge which are required for dielectrophoretic forces.

vicinity of the structured non-conducting posts induce dielectrophoretic traps described by the potential function (see paragraph 2.2.2)

$$\Psi_{\text{DEP}} = -\frac{1}{2} \alpha_p \vec{E}^2. \quad [4-4]$$

Regions with high electric field strength are thus local potential minima for the DNA molecules. Secondly the applied DC offset U_{DC} causes a constant tilt of the whole potential landscape because the electrophoretic force is proportional to the electric field and thus induces electrophoretic motion of the analyte molecules (see paragraph 2.2.1). Finally the omnipresent thermal energy $k_B T$ introduces thermal fluctuations (see section 2.3).

In summary, electrophoresis and dielectrophoresis create the effective potential landscape, illustrated in Figure 33 being basically an inclined plane superimposed by an array of dielectrophoretically induced local potential minima. A cross section of Figure 33 parallel to the x axis along a line of dielectrophoretic traps is illustrated schematically in Figure 34. A charged and polarizable (bio-) particle (brown circle) is migrating down the inclined plane parallel to the x axis driven by electrophoresis until it is trapped by a local dielectrophoretic potential minimum. The relevant potential barrier $\Delta V - \Delta W_{DC}$ is so high, that the particle

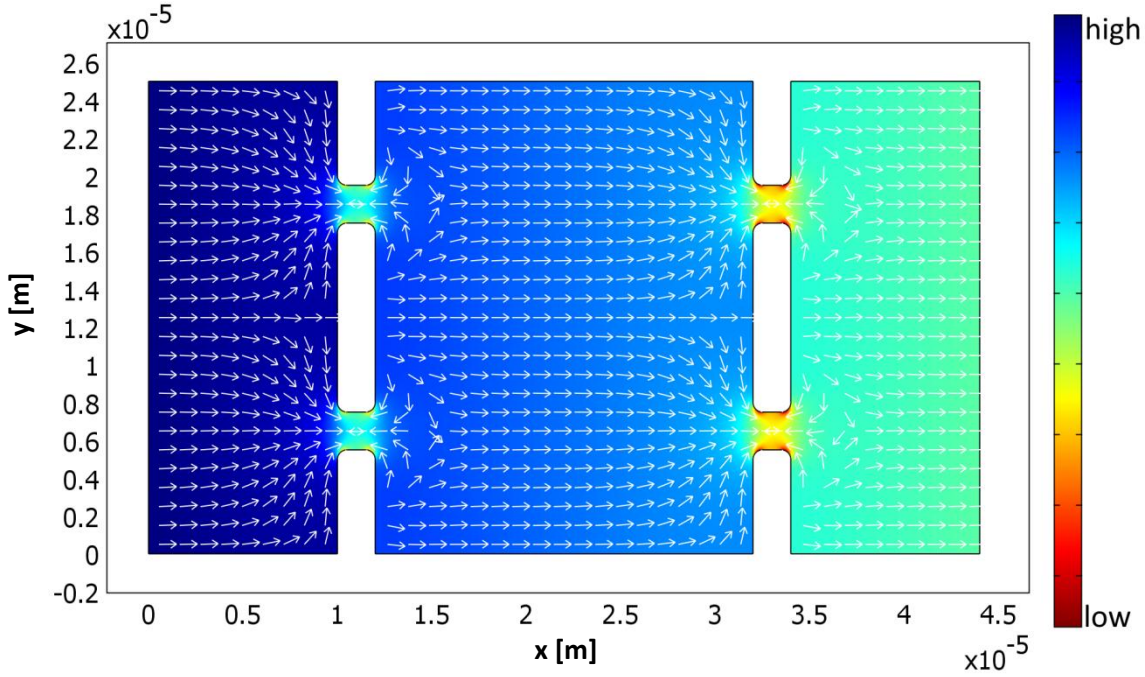


Figure 33: Effective potential (color code in arbitrary units) and resulting force (normalized vectors) exerted on a DNA molecule flowing through the structured part of the microfluidic device. For the used DNA molecules (positive dielectrophoresis) potential minima can be found in the gaps between the posts because here, the electric field strength has a maximum. Regions of low field strength on the other hand are potential maxima.

would be trapped forever without diffusion. However, if $\Delta V - \Delta W_{DC}$ is only slightly larger than the ambient thermal energy $k_B T$, it is possible for the particle to escape out of the trap in a reasonable time and migrate further through the structure until it is trapped by a further potential minimum.

Recalling paragraph 2.4.1, the escape rate out of such a potential minimum can be described with a Kramers rate R_K

$$R_K \propto \exp \left[- \left(\frac{\Delta V - \Delta W_{DC}}{k_B T} \right) \right]$$

with its inverse

$$\tau_K \propto \exp \left(\frac{\Delta V - \Delta W_{DC}}{k_B T} \right) \quad [4-5]$$

which is the average time, a particle is trapped before it is able to escape due to a thermal kick with sufficient energy. The next step is the quantification of the numerator in equation [4-5]. It is dependent on the particle's polarizability being the desired result.

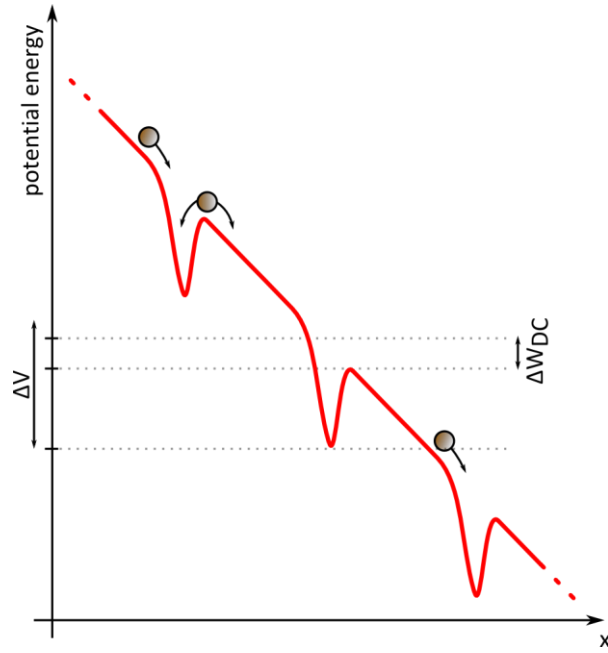


Figure 34: Cross section of the effective potential landscape parallel to the x axis through the dielectrophoretic traps (schematically). While local potential minima (traps) are induced by dielectrophoresis, the applied Bias U_{DC} homogenously tilts the effective potential function along the x axis. A charged and polarizable (bio-) particle (brown circle) thus migrates down the inclined plane until it reaches a potential minimum with height $\Delta V - \Delta W_{DC}$ where it is permanently trapped in the first instance. However, if this potential barrier is not too large compared to the thermal energy $k_B T$, it will randomly be able to leave the trap when it receives a sufficient thermal kick and migrate further through the channel until it enters the next trap. The escape process can be modeled with a Kramers rate R_K (see paragraph 2.4.1) to calculate mean trapping times and thus the effective particle polarizability α_p .

To obtain a value for $\Delta V - \Delta W_{DC}$, the electric field between the posts, that is dependent on the applied voltages and especially the channel geometry needs to be quantified. This dependence is expressed by a proportionality constant ξ in the relationship

$$E^2 = 2\xi U_{AC}^2.$$

Here, the contribution of the DC voltages to the dielectrophoretic traps is neglected because usually $U_{AC} \gg U_{DC}$. ξ has been obtained previously by Regtmeier et al. via approximating the microfluidic channel with a network of resistors resulting in $\xi \approx 22900 \text{ m}^{-2}$ ⁸². Inserting equation [4-4] into equation [4-5] to express ΔV then leads to

$$\tau_K \propto \exp\left(\alpha_p \frac{\xi U_{AC}^2}{k_B T}\right)$$

assuming again that $U_{DC} \ll U_{AC}$. Because ΔW_{DC} is kept constant, it can be absorbed into the proportionality constant. To obtain α_p experimentally it is now necessary to measure the average logarithmic trapping times $\ln(\tau_K)$ for different U_{AC}^2 and constant U_{DC} because

$$\ln \tau_K \propto \alpha_p \frac{\xi U_{AC}^2}{k_B T}$$

and thus

$$\alpha_p = \frac{\ln \tau k_B T}{\underbrace{U_{AC}^2}_u \xi}$$

When fully considering equation [2-23] also non-exponential terms occur which are, however, still dependent on α_p . Therefore, logarithmic corrections to the otherwise linear fit in an $\ln \tau_K$ vs. U_{AC}^2 plot are required and thus the actual general fit function for such a plot is

$$f(x) = u \cdot x - \ln(x) + q_0$$

where u and q_0 are fit parameters¹⁸⁴.

Consequently the key problem for the quantification of single molecule polarizabilities is the measurement of the mean trapping time τ_k in dependence of U_{AC} . Of course one could count the number of frames a specific molecule stays in a trap and average over many molecules, but this procedure has three major drawbacks. First of all, it is very tedious work taking several hours to gain enough information so that statistical significance is achieved. Secondly, the maximum available frame rate of 10 fps is usually not high enough to exactly determine the instant of time of entering and escaping processes. Finally, not all molecules are considered and the evaluated portion is chosen by the experimenter and thus not completely random.

Therefore, an alternative evaluation method with high potential for automatization in the context of a final commercial product is considered. During an experiment, fluorescently labeled DNA ensembles are migrating through the structure and the recorded greyscaled image series thus contain spatially and temporally localized brightness information. The basic idea behind the automated analysis of DNA polarizability is the reduction of the problem to a simple time dependent measurement of fluorescent brightness. This quantity is proportional to the number of visible DNA molecules assuming that the DNA has been homogenously stained and when taking care, that the DNA concentration is sufficiently low to avoid camera saturation. After N_T columns of posts (in this thesis $N_T = 4$ was used, counted from the sinistral beginning of the structure) a rectangular region of interest which spans over the whole image in y direction and 10 pixels ($\cong 5.2 \mu\text{m}$) in x direction is defined

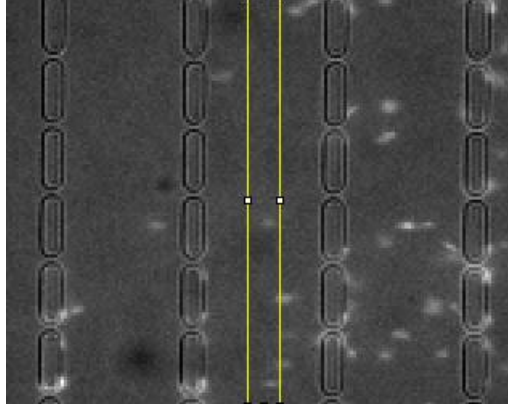


Figure 35: Definition of a region of interest for the analysis of the temporal evolution of fluorescence intensity required for the quantification of single DNA (white spots) polarizability. It is located behind four columns of posts from the left beginning of the structure (not completely shown in the image) and spans over the whole image height (y direction) and over 10 pixels ($\cong 5.2 \mu\text{m}$) in x direction. The final result is a convolution of the time dependent fluorescence intensity function and the geometry of the region of interest which should thus be set infinitesimally small in x direction. However, this is unpractical for accurate image analysis because the signal to noise ratio would be too small. Thus, the actual width of 10 pixels is a convenient compromise which was identified empirically.

(see Figure 35). Subsequently the mean brightness of all pixels in the region of interest is determined for each image. The result is a time dependent distribution $H_{N_T}(t)$ that is automatically baseline corrected by subtracting the mean value of $H_{N_T}(t)$ obtained over the first 60 frames of the video where typically no DNA is visible.

The mean migration time it takes for a DNA molecule from the injector to the region of interest can be extracted out of $H_{N_T}(t)$ via

$$\langle t \rangle = \frac{\sum_i H_{N_T}(t_i) \cdot t_i}{\sum_i H_{N_T}(t_i)}. \quad [4-6]$$

Because the potential tilting induced by U_{DC} is usually large enough, one can safely assume that a specific molecule cannot be trapped by more than one trap in a single column. The result is the actual sum of free migration times t_{free} and the mean trapping times in N_T traps which is $N_T \cdot \tau_K$ provable as follows¹⁸⁴. First, three statistical distributions are defined:

- $\Psi_{\text{esc}}(t)$: Distribution of trapping times
- $\Psi_f(t)$: Distribution of free migration times between the traps
- $\Psi_+(t)$: Distribution of free migration times between the injector and the structure

Combining these functions leads to a theoretical description of the brightness distribution in the region of interest after the molecules passed N_T traps:

$$H_{N_T}(t) = \int d\tilde{t} \Psi_+(\tilde{t}) \int \prod_{i=1}^{N_T} dt_i dt'_i \Psi_{\text{esc}}(t_i) \Psi_f(t'_i) \cdot \delta \left[t - \left(\tilde{t} + \sum_{n=1}^{N_T} t_n + t'_n \right) \right] \quad [4-7]$$

Assuming that the description with a Kramers rate is valid (see paragraph 2.4.1) or in other words assuming that the thermal energy is small compared to the dielectrophoretic potential barrier ($k_B T \ll \Delta W$), Ψ_{esc} can be directly identified as

$$\Psi_{\text{esc}}(t) = \frac{1}{\langle \tau_K \rangle} \exp \left(-\frac{t}{\langle \tau_K \rangle} \right).$$

It is furthermore assumed, that the distribution of DNA molecules directly after the injection is describable with a δ -function. This is reasonable when compared with the DNA distribution after N_T traps. Additionally it is safe to assume that distribution broadening is only induced by the traps and not in between by diffusion. With these assumptions, $\Psi_+(t)$ and $\Psi_f(t)$ can be explicitly declared as well:

$$\Psi_+(t) = \delta(t - t_+) \quad \text{and} \quad \Psi_f(t) = \delta(t - t_0)$$

Here t_0 is the time it takes for a molecule to travel from one trap to the next and t_+ is the time, a molecule needs to migrate from the injector to the first trap. With these assumptions, equation [4-7] can be simplified to

$$\begin{aligned} H_N(t) &= \int \prod_{i=1}^{N_T} dt_i \Psi_{\text{esc}}(t_i) \cdot \delta \left(t - t_+ + N_T t_0 - \sum_{n=1}^{N_T} t_n \right) \\ &= \int \prod_{i=1}^{N_T} dt_i \Psi_{\text{esc}}(t_i) \cdot \delta \left(t - t_{\text{free}} - \sum_{n=1}^{N_T} t_n \right) \end{aligned}$$

where $t_{\text{free}} = N_T t_0 + t_+$. Using a Laplace transformation the problem can be solved and one obtains

$$H_{N_T}(t) = \frac{1}{\tau_K (N_T - 1)!} \cdot \left(\frac{t - t_{\text{free}}}{\tau_K} \right)^{N_T - 1} \cdot \exp \left(-\frac{t - t_{\text{free}}}{\tau_K} \right) \cdot \Theta(t - t_{\text{free}})$$

where $\Theta(t - t_{\text{free}})$ denotes the Heaviside step function to suppress negative values of the brightness function before the DNA arrives. The mean time it takes for a DNA molecule to arrive at the region of interest can now be calculated via

$$\begin{aligned}\langle t \rangle &= \int dt H_{N_T}(t) \cdot t \\ &= N_T \cdot \tau_K + t_{\text{free}}\end{aligned}$$

or in other words

$$\tau_K = \frac{\langle t \rangle - t_{\text{free}}}{N_T}. \quad [4-8]$$

As already mentioned, $\langle t \rangle$ can be extracted from the time dependent fluorescence brightness distributions by weighting discrete time points with the measured brightnesses. t_{free} is obtained experimentally by additionally providing a measurement without dielectrophoretic traps ($U_{AC} = 0$) because

$$t_{\text{free}} = \langle t (U_{AC} = 0) \rangle.$$

In conclusion, an automated setup for the determination of the polarizability α_p is proposed to operate according to the following algorithm (source codes are given in appendix A2.1).

1. Record image sequences of DNA migrating through the structured area of the chip for different U_{AC} , especially for $U_{AC} = 0$ V and constant U_{DC} .
2. Set region of interest after N_T columns of traps and analyze mean brightness of all pixels therein as a function $H_{N_T}(t)$ of the elapsed time for every image stack with different U_{AC} .
3. Calculate the individual baseline of each stack by averaging the first 60 frames and subtract this value from every frame in the currently considered $H_{N_T}(t)$.
4. Calculate $\langle t \rangle$ according to equation [4-6] and with that result τ_K with equation [4-8] for every realization.
5. Calculate a statistical error with a bootstrapping method. Here 2/3 of all data points are randomly selected 10.000 times and equation [4-6] is evoked once again on this subset. The statistical error $\Delta\langle t \rangle$ is the standard deviation of the bootstrapped values from the original result for $\langle t \rangle$.
6. The results for τ_k are plotted in the form $\ln \tau_K(U_{AC}^2)$ and the function is analyzed with the fit function $f(x) = u \cdot x - \ln(x) + q_0$ via u and q_0 .

The question remains whether the discussed automated evaluation method based on the analysis of fluorescent brightness distributions yields comparable results compared to a

manual analysis of 30 molecules. A quantitative comparison between both methods is provided in Figure 36 where the mean trapping times τ_K of λ -DNA (48 502 bp) are obtained for several different U_{AC} values. While the blue plot is obtained by manually counting the video frames a molecule stays in a trap and averaging over 30 individual molecules (result $\alpha_p = (3.1 \pm 0.3) \cdot 10^{-29} \text{ Fm}^2$), the red plot shows data obtained with the newly developed brightness distribution method which considers all present molecules (result $\alpha_p = (2.8 \pm 0.6) \cdot 10^{-29} \text{ Fm}^2$). In this comparison, no significant difference, in particular no systematic deviations of the considered data points is notable.

However, directly comparing these values to the literature is difficult. Besides the different employed techniques, especially the DNA length, applied frequencies, and the ionic conditions in the surrounding solution have an impact on the polarizability (see paragraph 4.2.2). Unfortunately several different buffer systems instead of a single standard were employed in the literature. Furthermore, the present approach requires fluorescent staining whose impact is closer discussed in paragraph 4.2.3.

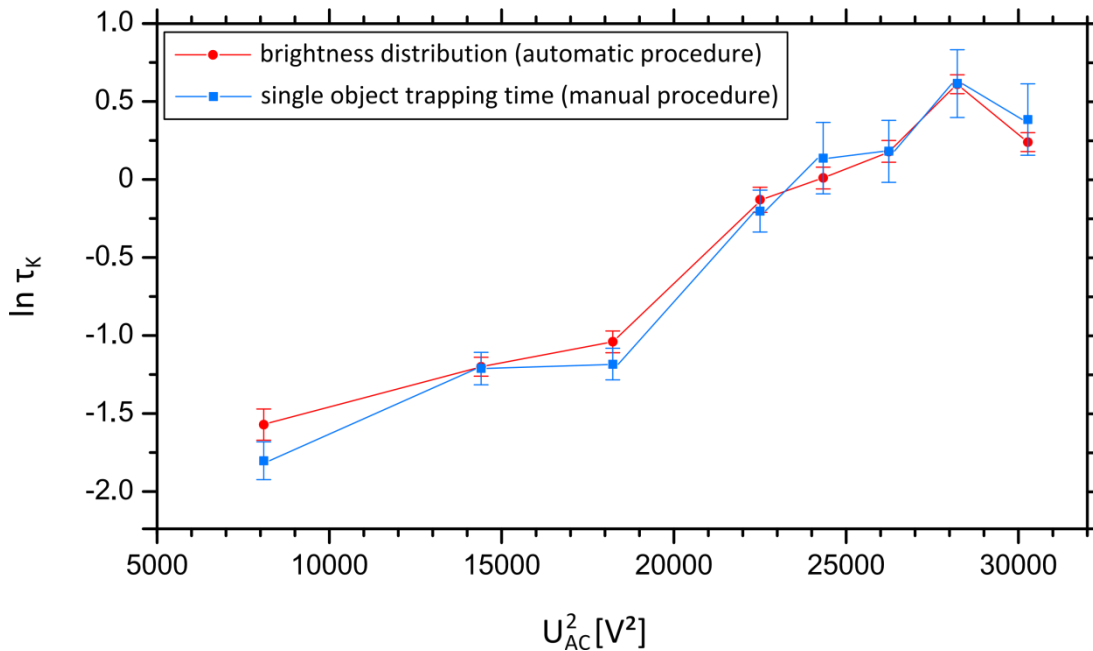


Figure 36: Exemplary measurement of the mean trapping time τ_K of linear λ -DNA for different U_{AC} values, analyzed with two different methods (with lines as guides to the eye). The blue dataset is obtained by simply counting the video frames a molecule stays in a trap and average the results of 30 individual molecules. The red dataset is an evaluation of the same experimental data with the newly developed automated method which relies on analyzing fluorescence brightness distributions as described above. There is now significant difference between the results and in particular no systematic deviation.

Nevertheless the obtained values for λ -DNA are quite comparable to the literature. Using transient electric birefringence, e.g. Rau and Bloomfield quantified the polarizability of 39.9 kbp T7 phage DNA and obtained $1.3 \cdot 10^{-28} \text{ Fm}^2$ in 0.5 mM sodium phosphate buffer at pH=6.9¹⁸⁰. For an even shorter 4.4 kbp DNA fragment in 0.2 mM Tris buffer at pH=8, Stellwagen found $5.56 \cdot 10^{-31} \text{ Fm}^2$ with the same technique¹⁸¹. Another approach which also employs dielectrophoretic trapping in a tilted potential was recently made by Tuukkanen and colleagues¹⁸⁵. Here, a dielectrophoretic field induced by a pair of structured electrodes is chosen such that it barely overcomes thermal energy. In the following calculation, the dielectrophoretic potential well is equalized with the thermal energy and thus the polarizability value is obtained. Their shorter 8 kbp DNA fragment showed a polarizability of $8.4 \cdot 10^{-30} \text{ Fm}^2$ (3mM Hepes, 1mM NaOH, pH=6.9, 200 kHz). This value is quite comparable to the obtained data for λ DNA here keeping the different buffer solution and the shorter DNA fragment in mind. As already stated, the exact comparison of the polarizability values with the exemplary data from the literature is impossible due to the influence of many side effects and technical details. However, the experimental results obtained here lie well within similar orders of magnitude. Furthermore the comparison shows, that the slight deviation of 9.6 % between the manual evaluation and the new automated procedure is insignificant. The manual evaluation involves besides other severe drawbacks very tedious work as one data point requires approximately 15 – 20 minutes for its analysis. A typical dataset like the one illustrated in Figure 36 with eight data points is thus processed in roughly 2½ hours. Depending on the available hardware, the script (see appendix A2.1) completes its analysis of the same data in less than one minute and considers all of the several hundred injected DNA molecules.

4.2.2 VERIFICATION: POLARIZABILITY VS. IONIC STRENGTH

A scaling law, well-documented in the literature and studied so far with different techniques is the correlation between the molecular polarizability and the ionic strength of the surrounding solution^{180,186–188}. In this paragraph this scaling law $\alpha_p \propto \lambda_D \propto 1/\sqrt{I}$, where λ_D represents the Debye-length and I the ionic strength is closer analyzed to validate the new automated quantification method for molecular polarizabilities. The results for 12 kbp and 48.5 kbp DNA are summed up in Table 9 and plotted with two logarithmic axes in Figure 37 to obtain scaling exponents.

Table 9: Measured polarizability values in dependence of the ionic strength I for two different double stranded DNA fragments, 12 kbp and the 48.5 kbp long λ -DNA.

12 kbp linear DNA		48.5 kbp linear DNA	
Ionic strength I [10^{-2} mol/l]	Polarizability α_p [10^{-29} Fm ²]	Ionic strength I [10^{-2} mol/l]	Polarizability α_p [10^{-29} Fm ²]
0.48	5.13 ± 0.15	1.13	3.44 ± 0.54
0.74	3.11 ± 0.11	2.13	2.10 ± 0.83
0.99	3.30 ± 0.13	4.13	2.19 ± 0.03
1.48	4.64 ± 1.59	5.13	1.73 ± 0.08
2.21	2.65 ± 0.17		
3.73	1.79 ± 0.07		
4.74	1.76 ± 0.11		

For both DNA types, it is observable that the molecular polarizability decreases with increasing ionic strength. The slopes of the double logarithmic depictions in Figure 37 are $m_{12kbp} = -0.46 \pm 0.02$ and $m_{\lambda} = -0.51 \pm 0.1$ which lies very close to $-1/2$. This means that indeed the scaling law $\alpha_p \propto 1/\sqrt{I}$ is reproduced by the present approach with deviations below 2σ on the single molecular scale.

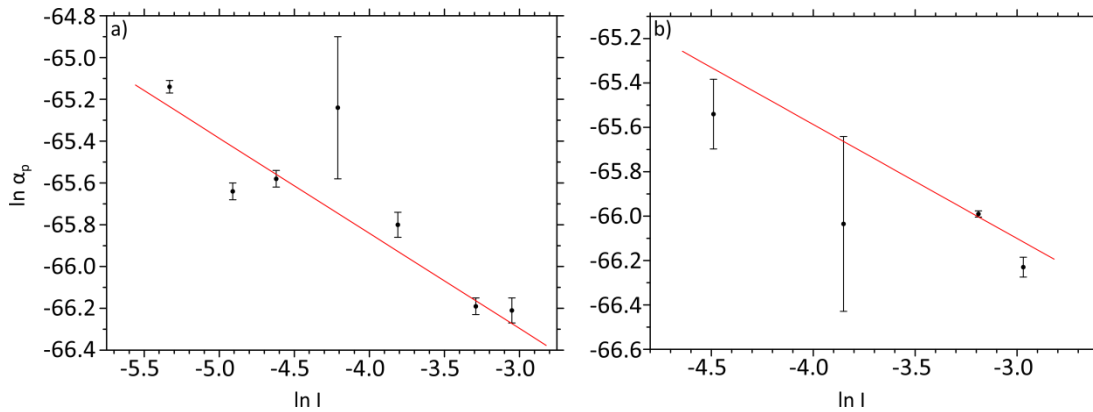


Figure 37: Dependence of the polarizability α_p on the ionic strength of the surrounding solution tuned by adding monovalent sodium chloride ions for two different DNA lengths. The resulting slopes of the weighted linear fit functions are -0.46 ± 0.02 for the 12 kbp DNA in a) and -0.51 ± 0.1 for the λ -DNA with 48.5 kbp in b).

4.2.3 POLARIZABILITY IN DEPENDENCE OF DYE CONCENTRATION

In comparison to established macroscopic techniques for the quantification of polarizabilities^{180–183} the present microfluidics based method requires the use of fluorescent staining or some other tag to detect the position of the molecule. However, a molecule like YOYO-1 carrying four positive charges and intercalating into the DNA strand (see paragraph 2.5.2) is suspected to somehow alter the polarization behavior because it might have an impact on the dynamics of the ion cloud surrounding the DNA and on the persistence length. This could be considered as drawback of the present approach. This paragraph investigates the impact of fluorescent staining with different YOYO-1 concentrations on the resulting polarizability of double stranded 12 kbp DNA. Using the method introduced in paragraph 4.2.1 the main result is depicted in Figure 38 for a practically relevant spectrum of dye concentrations.

The dependence of fluorescent staining with YOYO on the system's polarizability is weaker than the deviations induced by a change of the buffer's ionic strength (cf. Table 9) but lies in the same order of magnitude. However, the influence is notable and shows a significant non-monotonic behavior around concentrations of 15 to 20 basepairs per dye molecule. From 1 to 15 basepairs per YOYO (Figure 38 a) the polarizability α_p of the DNA-YOYO compound is decreasing with decreasing dye concentrations. On the other hand from 15 to 30 basepairs per YOYO molecule (Figure 38 b) a notable increase in polarizability is observed for decreasing dye concentrations.

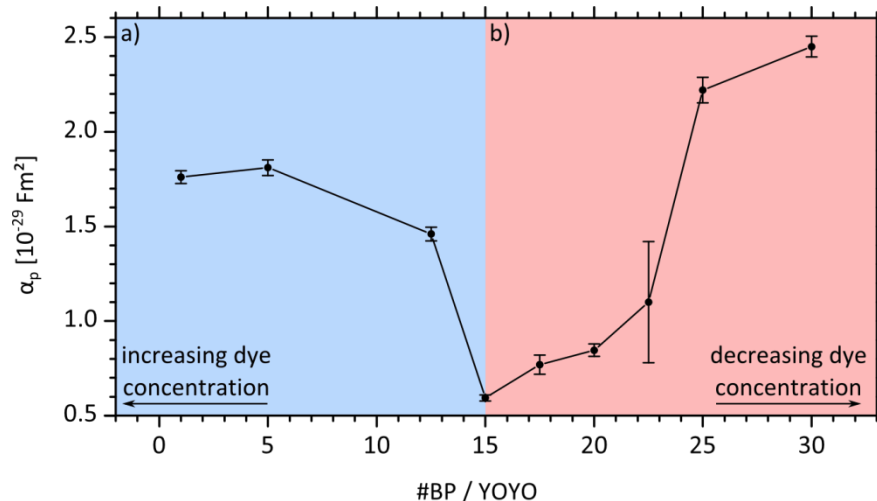


Figure 38: The analysis of the polarizability of 12 kbp doublestranded DNA intercalated with different concentrations of YOYO-1 reveals a relatively weak but non-monotonic dependence compared to a change of the buffer's ionic strength. The black solid lines are meant as guide to the eye.

The observations in the red part of Figure 38 can be explained with a very simple picture. The YOYO intercalation is characterized as equilibrium reaction (see paragraph 2.5.2 and references therein). Thus, increasing the overall concentration of free YOYO in the buffer will inevitably lead to an increased absolute number of intercalated molecules. Because YOYO carries four positive charges (in contrast to the negatively charged backbone of the DNA) more intercalated dye molecules will lower the effective charge of the DNA-dye system. Thus, less buffer ions are required to shield it in the liquid. However, the charges in the ion cloud are one major contributor to the overall polarizability of the DNA molecule^{65,187,189}. Consequently the polarizability decreases with increasing dye concentration.

An alternative or possibly coexistent mechanism could be the following. With increasing YOYO-concentration, more and more free dye molecules are present in the surrounding liquid as well. Although the YOYO-molecules interact differently with the DNA than sodium ions, the decrease of polarizability in this regime can be somehow compared to the results from paragraph 4.2.2 where the polarizability decreases with increasing ionic strength. Assuming a typical DNA concentration in the microfluidic device of 50 pM/l and a basepair/dye ratio of 8:1, approximately 75 nM/l YOYO are present in the buffer. According to Larsson et al.¹⁵³ the typical binding constant of YOYO in this concentration regime is 10^{10} M^{-1} . Consequently, only a tiny amount of $\frac{75 \text{ nM/l}}{10^{10}} = 7.5 \text{ aM/l}$ of free unbound YOYO is available. This corresponds to an increase of ionic strength of $\Delta I = 6 \cdot 10^{-17}$ which will have a fairly low influence on the polarizability compared to the results e.g. of paragraph 4.2.2. Thus, the first hypothesis, that the total charge of the DNA molecule is reduced by intercalating YOYO seems to be more likely.

However, the increase of polarizability with further increase of the dye concentration in the blue part of Figure 38 is not that intuitive. First of all, the question arises, why the system behaves non-monotonic. In their study of YOYO binding behavior, Larsson et al. identified a critical dye concentration, where the preferred binding mechanism to DNA changes¹⁵³. Below this concentration, the usual bisintercalation of YOYO is observed. For higher dye concentrations, it is stated therein, that the YOYO molecules start to adsorb to the DNA grooves (see paragraph 2.5.2) and thus act as tetravalent groove binders. The critical value observed here is not exactly located at a concentration of 1:8 but lies in close proximity.

Now, that the YOYO molecule does not intercalate anymore the possibility to treat it as a tetravalent ion somehow adhering to the DNA opens up. A similar adhesion to DNA is

described in the literature for two other (however quite different) substances, the tetravalent spermine and the trivalent spermidine which are known to collapse and reexpand a DNA molecule in dependence of their concentration^{190,177}. Murayama et al. observed such a reexpansion for high spermidine concentrations (which is only trivalent) via force spectroscopy with optical tweezers. The adhered strongly positively charged molecules adhere to the DNA molecule and thus shield the intramolecular negative charges of the DNA backbone against each other. Thus, the overall persistence length is reduced which was also observed by Matsuzawa and Yoshikawa for the minor groove binder 4',6-diamidion-2-phenylindole¹⁹¹. The reason for the subsequent expansion of the DNA for even higher ion concentrations is speculated to be DNA overcharging¹⁹⁰ which means that even though the DNA is fully neutralized, further positive ions are accumulated¹⁹². Obviously an inverted overall charge of the DNA system would lead to an inverse electrophoretic mobility which was not observed in the present experiment. Nevertheless Hsiao et al. demonstrated in simulations, that such a described collapse in combination with subsequent reexpansion may be accomplished even without charge inversion. However, this effect is strongly dependent on the geometry of the considered multivalent ion^{193,192}. A possibility to investigate whether YOYO induces similar behavior would be a future experiment, where diffusion coefficients and thus radii of gyration of DNA for different dye concentrations are analyzed.

As the experiment in this paragraph demonstrates, there is a certain non-monotonic dependence of the polarizability α_p of DNA on the actual concentration of the employed fluorescent dye (here YoYo-1). However, the deviations compared to the results in paragraph 4.2.2 are notable but slightly weaker. Although the concentration of the dye was changed by a factor of 30 from 1 bp/YOYO to 30 bp/YOYO, the actual polarizability α_p changed only by approximately $1.8 \cdot 10^{-29} \text{ Fm}^2$.

4.2.4 SUMMARY

A microfluidic chip with structured non-conducting posts to generate electrodeless dielectrophoretic traps has been used to implement an automated quantification method for single molecule polarizabilities. Using two different DNA types the idea has been tested by successfully reproducing the well-known relation $\alpha_p \propto 1/\sqrt{I}$ between the polarizability and the buffer's ionic strength. The method requires spatial localization of the analyte

molecules e.g. here via fluorescence staining. For this reason the influence of the dye concentration on the DNA polarizability is investigated and found to be non-monotonic but in general rather weak.

4.3 ENANTIOSELECTIVE SEPARATION OF MICROPARTICLES

Two molecules which are chiral to each other behave like image and mirror image and cannot be transformed into each other by rotation or translation although they are described by the same chemical sum formula (see section 2.5.1). Biological systems such as the human body are highly chiral environments, because most of the basic building blocks of life (for instance typically left handed natural amino acids or typically right handed natural sugars¹⁹⁴) are chiral organic molecules. In most cases e. g. only one specific representation of a guest molecule can bind to a chiral receptor. A macroscopic example of everyday life would be the attempt to shake someone's left hand with one's right hand. Therefore, chiral partners (e.g. enantiomers) being used as racemic agents in pharmaceutical products may act completely different. While one form could show a therapeutical effect the other forms might be ineffective or even toxic when incorporated into an organism although their physical properties are identical (aside from optical phenomena)^{129,130,132,134,195-197}.

During in vitro synthesis of organic molecules a racemate is usually created with equal amounts of all chiral forms. Up to the 1980s, most of the newly introduced synthetically prepared pharmaceutical agents were sold without any chiral purification because such a complicated and costly process was unattractive. Hence, only 12 % of all available chiral products were distributed enantiopure at this time. During the second half of the 1980s this attitude changed, especially after the publication of a provoking article by Ariëns¹³¹ in 1984. It was stated in that publication, that inactive chiral constituents of a racemic pharmaceutical have to be regarded as an impurity and studies were referenced where they could even be identified as the main reason for side effects, may have opposite effects, or may be converted by the metabolism to active forms again, and so on. It took two decades until in 2004 no further racemic or diastereomeric new drugs were introduced to the market (see Figure 39)¹⁹⁸.

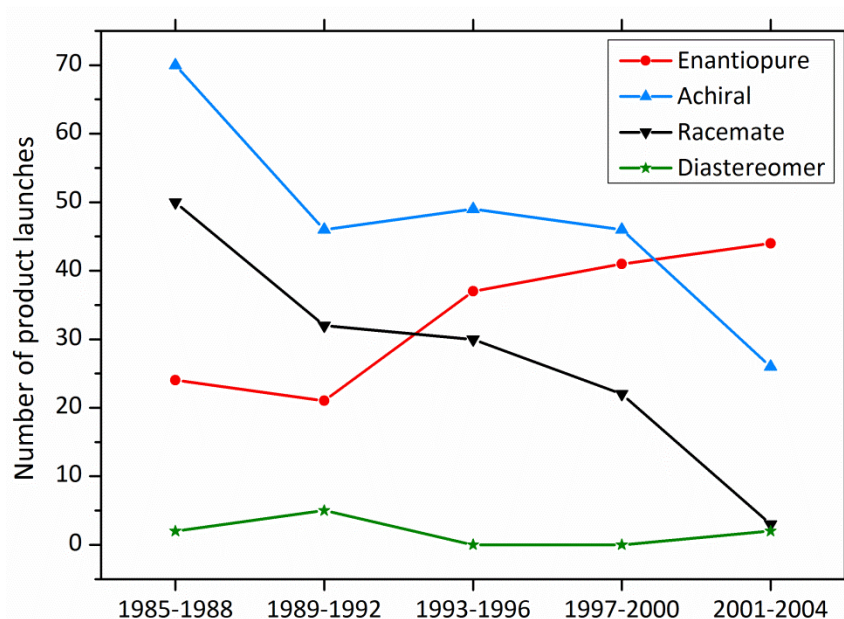


Figure 39: Overview of synthetic pharmaceutical product launches from 1985 to 2004. The trend towards clean enantiopure medication (red line) containing only single enantiomers is clearly visible. Drawn with data from¹⁹⁸.

As a consequence, there is an increasing demand for chiral separation techniques in the chemical and pharmaceutical industry which are today mostly based on chromatography and electromigration. Since these methods strongly rely on so called chiral selectors or chiral derivatisation agents their main disadvantage is, that these chemicals have to be precisely predesigned and developed for each chiral analyte^{11,199-204}.

Besides the utilization of different chemical affinities of enantiomers, physical effects, based on the chiral object's geometry have been studied in recent publications mostly from a theoretical point of view. The main advantages of these techniques are the abolition of the elaboration of chemical selectors. De Gennes predicted e.g. that two macroscopic chiral crystals would slide into different directions down an inclined plane²⁰⁵. Kostur et al. exploited a flow field with variable vorticity to theoretically demonstrate the separation of chiral particles²⁰⁶. Very recently, the same group studied the motion of *deformable* chiral objects in uniform shear flows delivering an even more realistic model²⁰⁷. A rotating drum filled with liquid and macroscopic chiral crystals was proposed for an experiment by Howard and coworkers for separation²⁰⁸. A quite similar system has been studied by Makino et al. theoretically and experimentally²⁰⁹. Shear flows have also been used by Chen et al. to induce different lifting forces of chiral helices in the flow²¹⁰. Kirkinis et al. simulated the separation of chiral ferromagnetic nanoparticles in electromagnetic fields²¹¹. Even achiral objects with anisotropic rigidity may be separated with shear flows according to the

theoretical study of Watari and Larson²¹². Another straightforward concept of dynamic symmetry breaking concerning the realization in a microfluidic device has been introduced by Speer et al. theoretically^{213,214}. A lattice of periodic potentials is tilted by a certain angle with respect to a constantly biased force. The chiral particles are subjected to this system and move under different deflection angles through the array for an array tilting angle of 45°. The symmetry breaking is thus dynamic. In contrast, Eichhorn proposed a theoretical concept where enantioseparation of chiral micro particles has been induced by using channels ruled by a force field with broken symmetry^{215,216}. However, the studies concerning experimental applications in the microfluidics scale or lower are rare. It seems that so far only Marcos et al. observed helical bacteria pumped through a very long serpentine micro channel²¹⁷. Nevertheless they considered only one chiral flavor of these bacteria.

In this section, efficient experimental separation of chiral microparticles in the microfluidic scale is presented which was carried out with two conceptual different approaches. The first concept, inspired by the purely theoretical work of Speer et al.^{213,214}, is discussed in section 4.3.2 and employs a tilted array of posts within a microfluidic channel to mime the modeled periodic potentials (see Figure 40). A fluidic stream of chiral microparticles that interacts with this kind of structure is shown to split up according to the corresponding particle species. Eichhorn proposed a second realization based on the interaction of chiral microparticles with an asymmetric flow profile within a microfluidic channel, realized with a spatially structured sidewall^{215,216}. It will be shown in section 4.3.3 that microparticles subjected to such a system will split up according to their chirality as well (see Figure 41). Both experiments are carried out with L and Γ shaped chiral microparticles fabricated with a newly introduced simplified quick release lithography procedure, discussed in section 4.3.1.

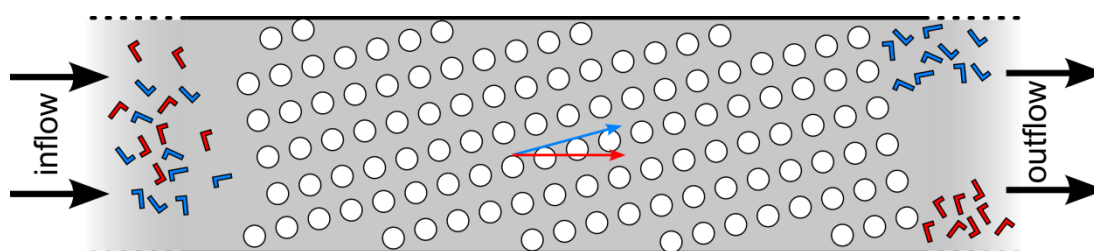


Figure 40: Schematic representation of the underlying separation principle (not to scale) for chiral microparticles in L (blue) and Γ form (red). A straight microchannel is equipped with a periodic array of potentials, tilted by a certain angle (neither 45° nor 90°) with respect to a constant biased force represented by the hydrodynamic transport from left to right. In this experiment, the potentials are mimed by periodically structured cylindrical posts which range from the channel bottom to the top. Because of the (asymmetric) particle interaction with the posts, the outcome is asymmetric as well and a splitting of the inserted particles according to the red and the blue arrow into two distinct streams will be observed.

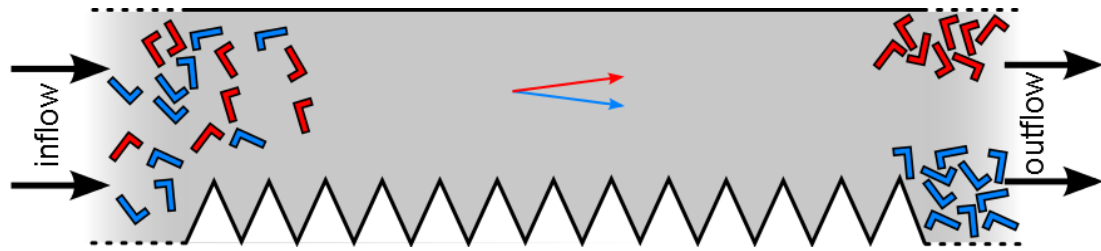


Figure 41: Schematic representation of the second underlying separation principle (not to scale). A straight micro channel is equipped with a triangular saw tooth structure on one side. Hence, the asymmetric micro particles with L and Γ shape interact differently with the resulting asymmetric flow profile and split up into two distinct streams at the end of the channel.

4.3.1 QUICK RELEASE LITHOGRAPHY

Besides being the essential ingredient for the presented chiral separation experiments, microparticles are important key elements in biotechnological, chemical and physical sciences. Possible applications might be carriers for vaccines²¹⁸, self-assembly of new materials²¹⁹, photonic materials²²⁰, microfluidic carriers²²¹, or even model systems for acoustics in media²²². Almost all commercially available micro and nano particles are spherical. Concerning the study of shape dependent phenomena, their field of application is thus strongly limited. However, several approaches were made to synthesize nonspherical microparticles employing many different materials and fabrication strategies^{223–231}. So far, two major strategies have been observed in the literature. On the one hand, particles were fabricated within the liquid phases of microfluidic systems where their shape was determined by the shape of the channels^{225,226,228}. On the other hand, the particles were structured on a substrate e.g. by lithography and released either mechanically²²⁷, with acids²²⁴, solvents²³¹, or sacrificial layers^{229,230}.

Results discussed in this paragraph have been published in: L. Bogunovic, D. Anselmetti & J. Regtmeier: *Photolithographic fabrication of arbitrarily shaped SU-8 microparticles without sacrificial release layers*, *Journal of Micromechanics and Microengineering* 21 (2011), 027003

The most common materials for fabricating these non-spherical particles are e.g. poly(ethylene glycol) diacrylate^{226–228}, silicon dioxide²²⁴, and the well characterized epoxy-based negative photoresist SU-8^{229–231}. SU-8 is a standard material in MEMS-technology due to its mechanical and chemical stability and its excellent processing properties²³². It is furthermore ideally suited for particle production as it offers the possibility to create structures with high aspect ratios at submicrometer resolution. Structures made of SU-8

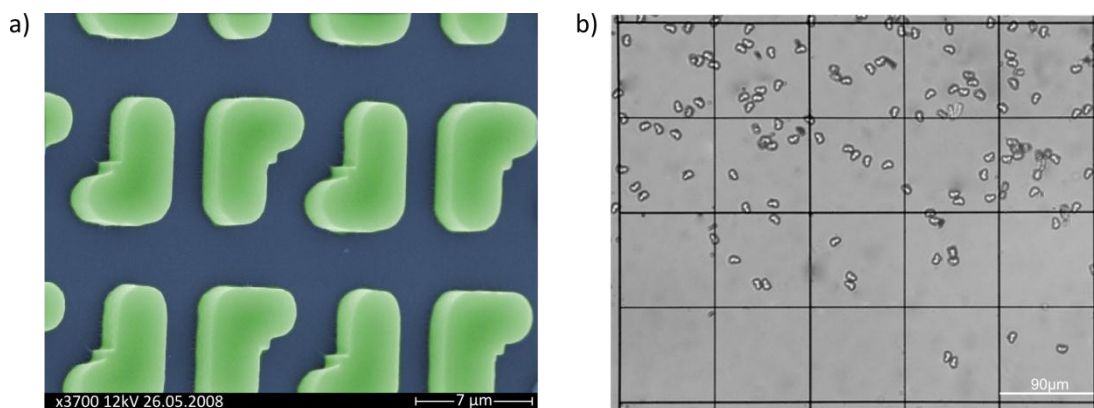


Figure 42: Scheme of the L-shaped particles to define dimensions. A): Scanning electron micrograph (colored) of the structured particles while they are still bound to the silicon substrate prior to removal. B): The L-shaped particles in free solution after they have been released from the substrate.

were even demonstrated to be fully biocompatible and even suitable for implantation and in vivo applications according to ISO 10993²³³.

Unfortunately, SU-8 is usually unsuited for lift-off processes complicating the release of the fabricated particles²³². Therefore, sacrificial layers of Omnicoat^{229,230} or polyimide are commonly used to release SU-8 patterns. A typical protocol contains the following steps:

1. spincoating and baking of the sacrificial layer.
2. spincoating and prebake of SU-8.
3. Exposure to UV light and postbake.
4. Development of the SU-8 structures.
5. Dissolution of the sacrificial layer and particle release.
6. Centrifugation and redispersion of the particles in a favored solution to remove the chemical agent for dissolution of the sacrificial layer (repeated up to three times).

The chiral microparticles used for the separation experiments in this thesis were fabricated according to a simplified new procedure *without* sacrificial layers or removal agents. The technique reduces the number of processing steps from 6 to 4, is cost efficient, freely scalable to large throughputs and requires less harmful chemicals.

Figure 14 shows the simplified lithography procedure for producing SU-8 microparticles with just 4 processing steps:

1. A SU-8 film is spincoated and prebaked. This step controls the height of the particles.

2. The photoresist is exposed to UV light and postbaked. The shape of the particles is controlled by the UV transparent regions on the mask.
3. The photoresist is developed.
4. Release of the particles by placing the silicon substrate in a vial filled with DI water in an ultrasonic bath.

As an example, L-shaped particles are shown in Figure 42 before and after release. Optical inspection revealed no destroyed or broken particles after sonification and release. Furthermore, no intra-particle adhesion was observed. An analysis of the size distribution by scanning electron microscopy is given in Figure 43. The deviations are less than 2.3 % and therefore competitive compared to recently published lithographically formed SU-8 particles: Badaire et al. demonstrated 6 % deviation using Omnicat^{229,230} and Moon et al. 10-50 % by using interference lithography and polyimide for lift-off²³¹.

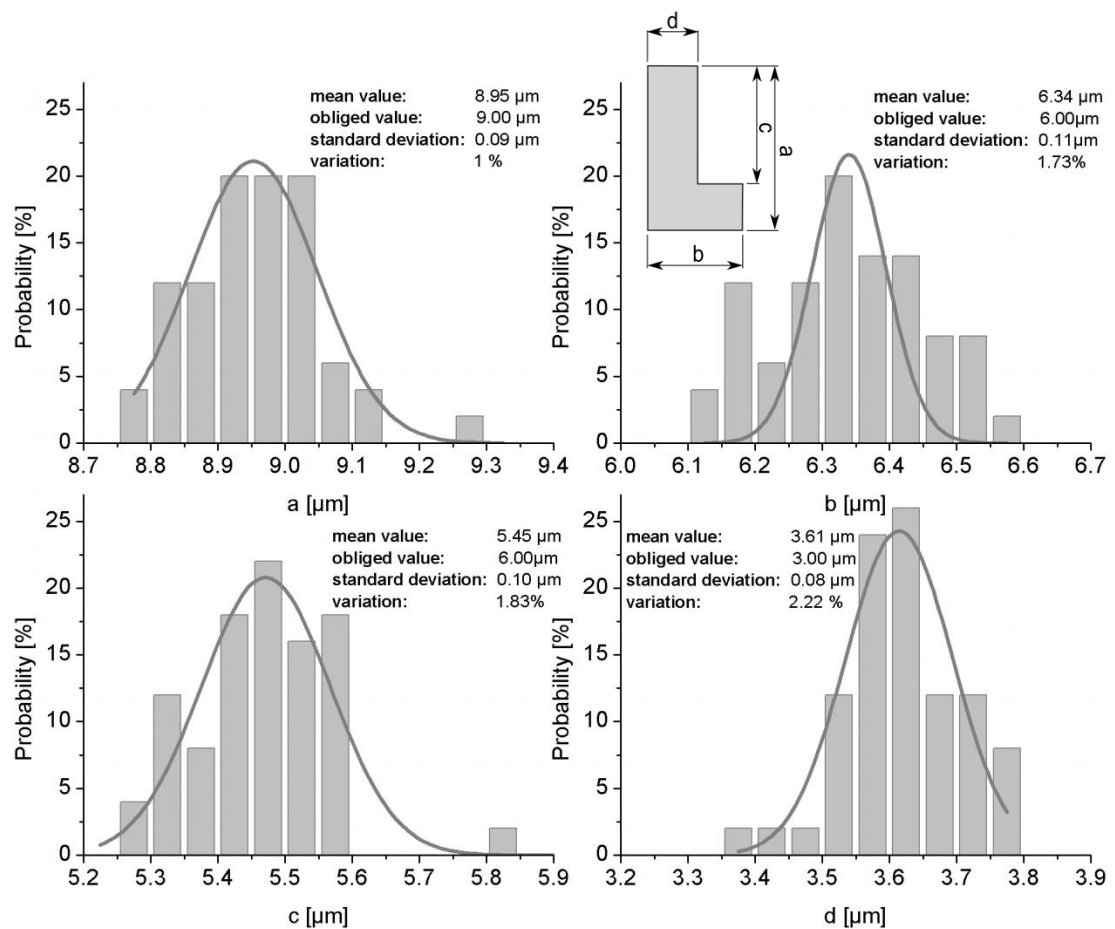


Figure 43: The measured four characteristic dimensions of the L-shaped reference particles in comparison to their corresponding obliged values and standard deviations / variations. The identifiers a,b,c, and d correspond to those in Figure 42. The sample size is n=50.

Finally Figure 44 shows more examples of microparticles, fabricated with the presented technique before (A, B, C) and after lift-off (D).

Usually SU-8 is considered as a hard to remove photoresist^{234,235}. The wide usage of products to generate sacrificial layers below the resist structure supports this claim. However, one could think of two effects that might sufficiently weaken the adhesion forces between the resist pattern and the substrate. First of all, instead of fabricating widespread microstructures with large contact areas, which is the typical application of SU-8, the micro particles here are relatively small. Secondly, during the lithography procedures, in some extend quite intense mechanical stress occurs up to 19 MP during postbake. These strains are provoked by material shrinkage due to cross-linking (up to 7.5 %), solvent evaporation or thermal expansion/retraction (up to 52 ± 5 ppm/K at 95°C) and might thus sufficiently weaken the adhesion to induce liftoff in the ultrasonic bath²³².

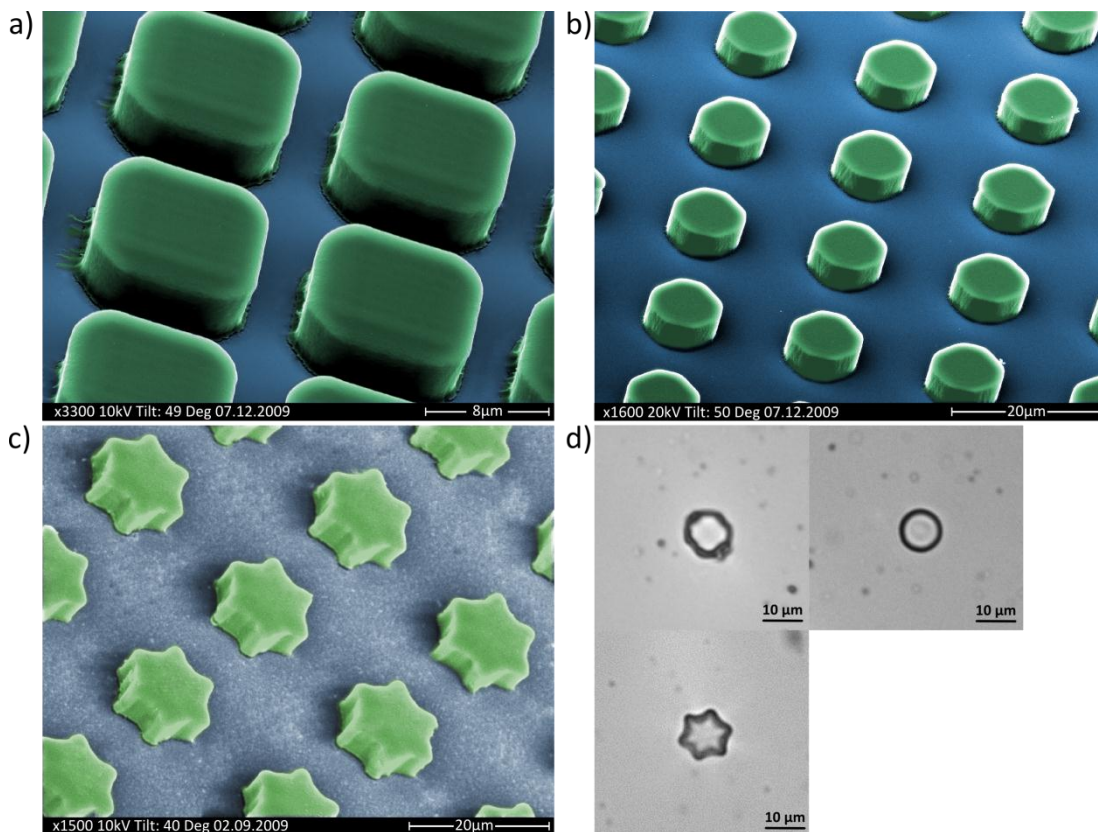


Figure 44: Scanning electron micrographs (colored) of further arbitrarily shaped microparticles before their lift-off: cuboids (A), cylinders (B), stars (C). D) shows the particles from A, B, and C after successful removal from the substrate in free solution via optical bright field microscopy.

4.3.2 CHIRAL PARTICLE SEPARATION WITH A *NON*-CHIRAL ARRAY OF POSTS

As already stated in the introduction of section 4.3, breaking the symmetry of the surrounding of chiral objects in every relevant dimension is sufficient to cause an asymmetric outcome which is the desired

Results discussed in this paragraph have been published in: L. Bogunovic, M. Fliedner, R. Eichhorn, S. Wegener, J. Regtmeier, D. Anselmetti & P. Reimann: *Chiral particle separation by a non-chiral micro-lattice*, Physical review letters 109 (2012), 100603

chiral separation (Curie's Principle²⁶). According to the purely theoretical work by Speer and coworkers^{213,214}, chiral objects transported by a constant bias force that interact with a regular array of potentials tilted by an angle $\alpha = 45^\circ$ against that driving force will effectively migrate into different directions.

The experimental realization of a related principle is schematically depicted in Figure 45. A 1 cm long (x direction), 1 mm wide (y direction) and 6 μm high (z direction) microfluidic channel connects two fluidic reservoirs that contain a solution of microfluidic test particles in deionized water. Their concentration is sufficiently low so that their interaction among each other is negligible. The experiment is carried out with chiral test particles with L and Γ shape fabricated according to paragraph 3.2.3 and closer elucidated in paragraph 4.3.1. The length of their long and short axis is a and b respectively with $3.0 \pm 0.3 \mu\text{m}$ thickness and a fixed aspect ratio. Their height of roughly 3 μm is an important parameter and has to correspond with the height of the microchannel under consideration which is 6 μm in this case. If the channel height is too low, particles cannot be injected into the channel. If it is too high, the particles may rotate along their long axis which means, that they would flip and hence change their chirality which is undesired. Here the relationship between particle and channel height is chosen in a way, that the particle can be injected into the channel but cannot switch its chirality. As a consequence the experiment can be regarded as effectively two-dimensional without loss of generality making complex three-dimensional structuring and evaluation unnecessary.

To realize potential functions analogous to²¹³ the whole microchannel is equipped with an array of cylindrical posts with diameter d_p and lattice constant l_p , tilted by an angle α with respect to the x axis. The particle flow through the microfluidic channel is maintained with a self-constructed pneumatic precision pump (see Appendix A1), connected to both reservoirs using silicone tubing. A hydrodynamic velocity of roughly 100 $\mu\text{m/s}$ is achieved by applying a pressure difference of $\Delta p \approx 15 \text{ mbar}$. During the experiment the particles are tracked via digital video microscopy (see section 3.4).

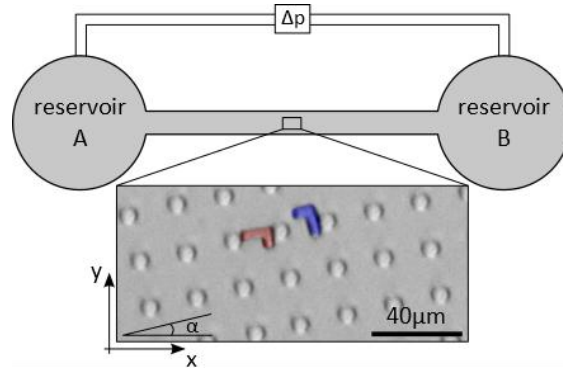


Figure 45: Schematic and a micrograph of the microfluidic setup used for the chiral separation with a tilted post array. A 1cm long (x direction), 1 mm wide (y direction) and 6 μm high (z direction) microfluidic channel connects two fluidic reservoirs where the particle solution is filled in before the experiment. A pneumatic precision pump (see Appendix A1) is attached with silicone tubes to both reservoirs and creates a pressure gradient Δp to transport the fluid through the channel. The required periodic potentials are mimed with an array of structured cylindrical posts, tilted by a certain angle α against the x axis.

4.3.2.1 THEORETICAL EVALUATION

The quantity of interest during this experiment are the mean velocities \vec{v}_L and \vec{v}_Γ of the injected L and Γ particles and especially the angle between \vec{v}_L and the x axis (ϑ_L) and \vec{v}_Γ and the x axis (ϑ_Γ) respectively.

Although the parameter space spanned by the four possible design characteristics (a, α, l_p, d_p) of the microfluidic device and the particles (see paragraph 4.3.2) is only four dimensional, it is still far too huge for efficiently designing a corresponding microfluidic layout that will produce significant $\Delta\vartheta = |\vartheta_L - \vartheta_\Gamma|$. Thus, extensive numerical simulations (see section 3.5) were conducted, to identify possible parameter sets as basis for a real microstructure and particles. However, the present section is confined to a well-fitting and experimentally realized parameter set although there are other solutions which produce significant $\Delta\vartheta$ values with comparable or less performance.

Because the system operates far from turbulent behavior at very low Reynolds numbers (see paragraph 2.1.2) a moderate rescaling of the complete system including microstructure and particles will not lead to significantly different results. Hence, the exact scale of the microfluidic setup is insignificant as long as all involved objects keep their aspect ratio and Re is still adequately small. To eliminate one degree of freedom of the problem, the lattice constant of the post array is fixed arbitrarily to $l_p = 20.5 \mu\text{m}$ in a first step, because it is experimentally well within the available soft lithography process.

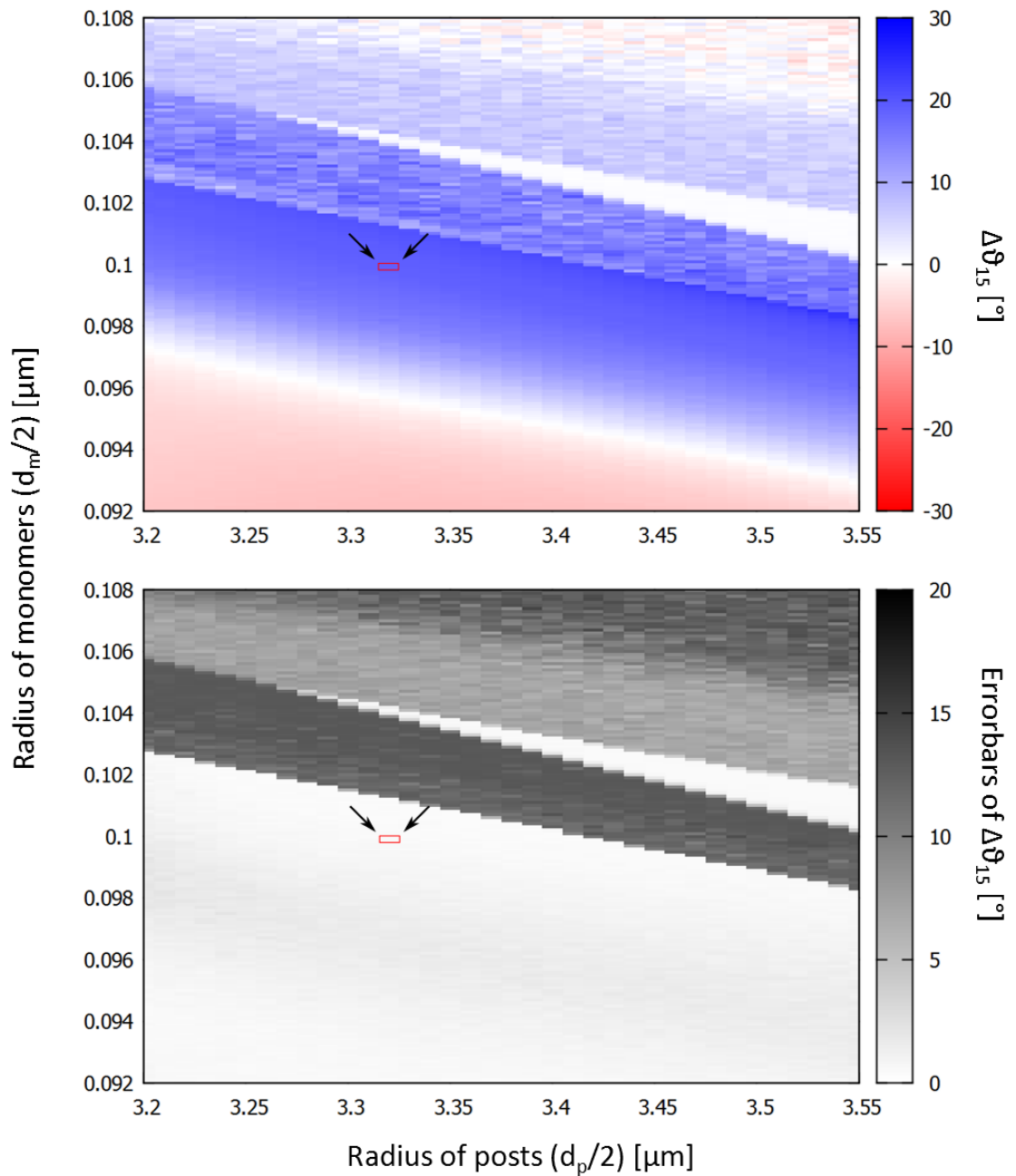


Figure 46: Upper image: Resulting separation angle $\Delta\vartheta_{15}$ at $\alpha = 15^\circ$ for different radii of the structured posts $d_p/2$ and for different particle sizes in terms of the radii of one monomer $d_m/2$ (the total number of monomers is kept constant). Parameters lying in the white areas do not produce significant $\Delta\vartheta_{15}$ whereas regions with strong blue or red color produce optimal splitting. The region in the upper right corner is characterized by significant interaction between the posts and the particles as they tend to stick within the structure while migrating. This leads to a significant increase of the error bars obtained for $\Delta\vartheta_{15}$ which are depicted in the lower image. From this result, the tuple from the darker blue region was selected, which promises significant $\Delta\vartheta$ and on the other hand holds enough distance to the unstable areas in the upper right corner: $(d_p/2, d_m/2) = (3.34 \mu\text{m}, 0.1 \mu\text{m})$.

The second step is the evaluation of the correlation between particle size (expressed here in terms of the radius of one monomer $d_m/2$ (see section 3.5)) and the radius of the structured posts $d_p/2$ for different array tilting angles α . Figure 46 shows a well working result for $\alpha = 15^\circ$ where 50 trajectories for each particle species per spot were averaged. The upper (colored) image represents the splitting angle $\Delta\vartheta_{15} = |\vartheta_L - \vartheta_R|$ in dependence of the particle size (represented by the size of a monomer) and the radius of the posts. The stronger the blue or red color, the larger is the angle of separation. White areas do now show any significant splitting. The upper corner where relatively large particles are brought in contact with small gaps between the posts (because of large post diameters) is characterized by increasing problems with particles getting stuck. As a result, the error bars for $\Delta\vartheta_{15}$ that are shown in the lower part of Figure 46 are increasing in this area.

A closer inspection of Figure 46 reveals that the actual motion of the particles through the array is a complicated process which is often not intuitively predictable. There are certain windows of separation where a significant splitting is observed. On the other hand there are certain regions, where both particle species only migrate along the structure without any notable splitting. For the actual separation process, a parameter tuple from the strong blue region in the middle of the shown parameter space was selected. It should on the one hand produce significant $\Delta\vartheta$ and on the other hand be sufficiently far away from the unstable areas in blue because in the experiment small particle or post deviations cannot be precluded. In the following, the tuple $(d_p/2, d_m/2) = (3.34 \mu\text{m}, 0.1 \mu\text{m})$ has been selected (marked red in Figure 46) and is subject to a closer inspection below.

Figure 47 and Figure 48 depict further results for $\alpha = 5^\circ, 10^\circ, 12.5^\circ, 17.5^\circ, 20^\circ$, and 22.5° and their corresponding error bars in the same arrangement as in Figure 46. These values are obviously not as suitable for chiral separation as the previous case of $\alpha = 15^\circ$. While $\alpha = 5^\circ$ does not produce any separation at all (e.g. both particles species migrate along the array axis and no locking occurs) the separation performance as well as the error bars increase with increasing α up to an optimum value for $\alpha = 15^\circ$. Larger values of α are again characterized by decreasing performance of separation while the standard deviations are further increasing, especially in those areas, where large particles interact with large posts.

Because of limited computing power, only a few values of α could be simulated in full detail as presented in Figure 47 and Figure 48. Instead, only the selected tuple $(d_p/2, d_m/2) = (3.34 \mu\text{m}, 0.1 \mu\text{m})$ which performs well under $\alpha = 15^\circ$ is now analyzed in more detail concerning the migration behavior under different values of α with finer resolution and

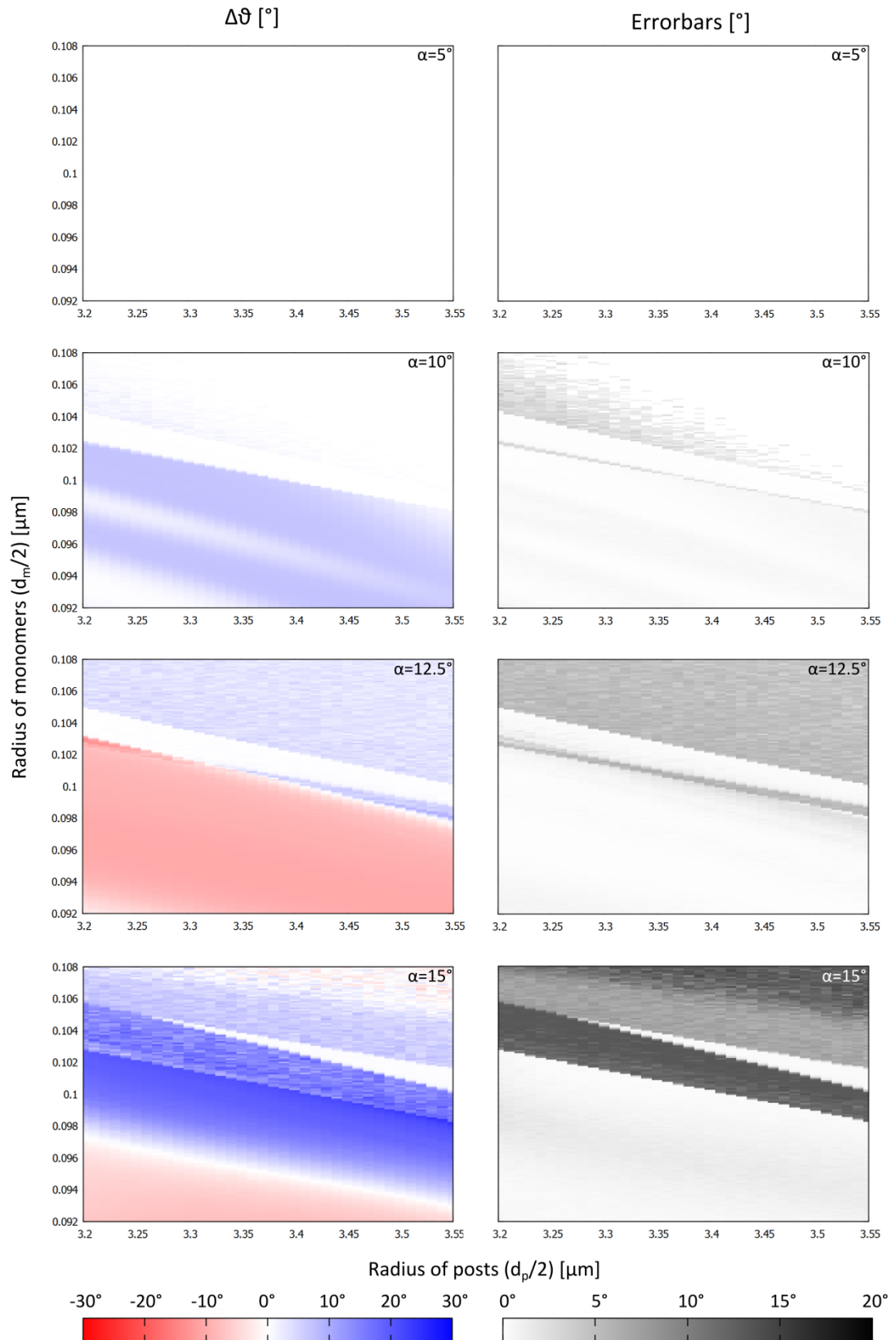


Figure 47: Separation results for $\alpha = 5^\circ, 10^\circ, 12.5^\circ,$ and 15° presented analogously to Figure 46. It is generally observable, that the separation performance increases for higher values of α . However, certain regions are more and more characterized by a strong increase of statistical errors for larger α .

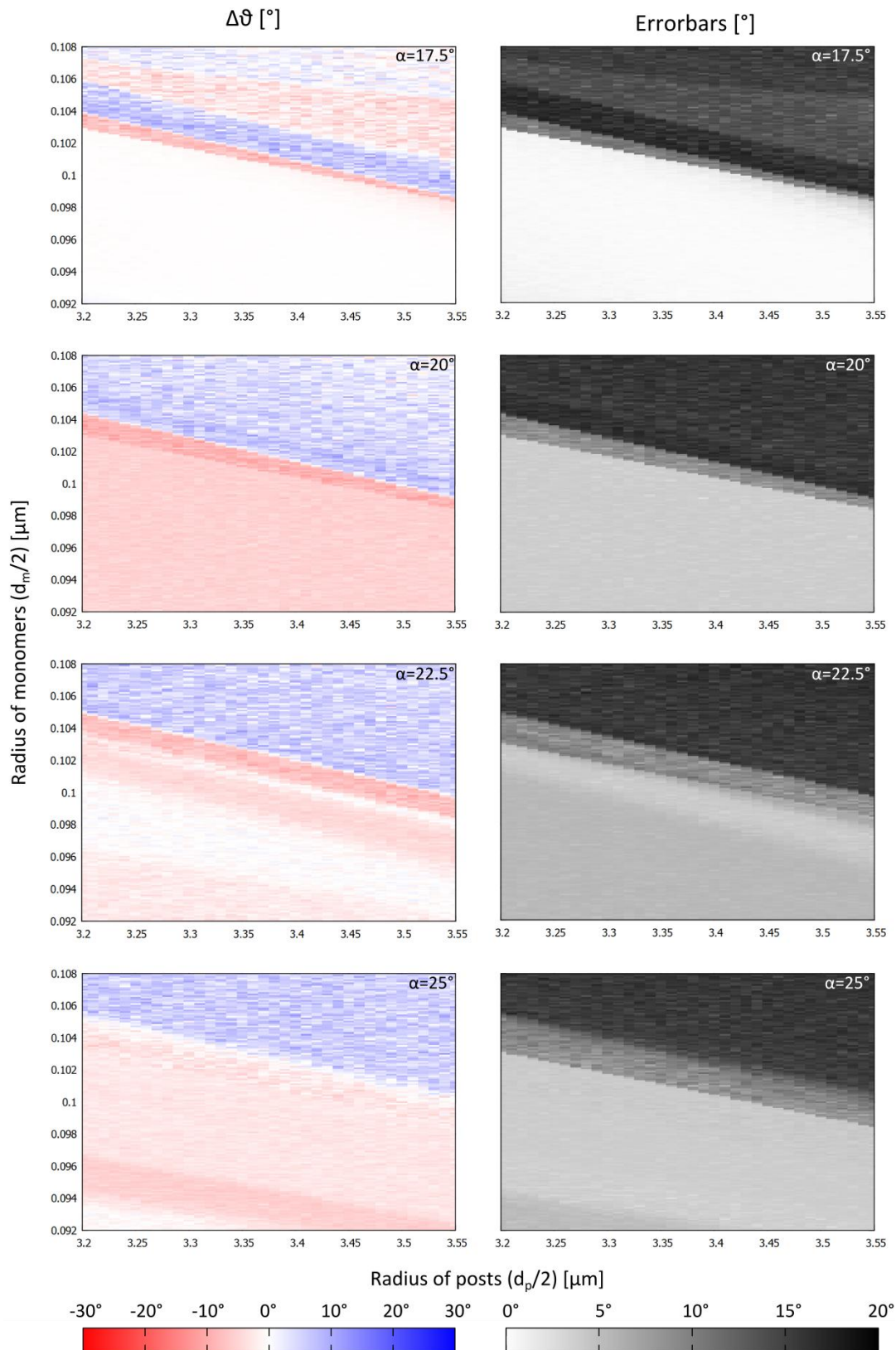


Figure 48: Separation results for $\alpha = 17.5^\circ, 20^\circ, 22.5^\circ$ and 25° presented analogously to Figure 46. It is generally observable, that the separation performance decreases for higher values of α . However, certain regions are characterized by very large statistical errors for, especially in regions where large particles interact with large posts (upper right parts).

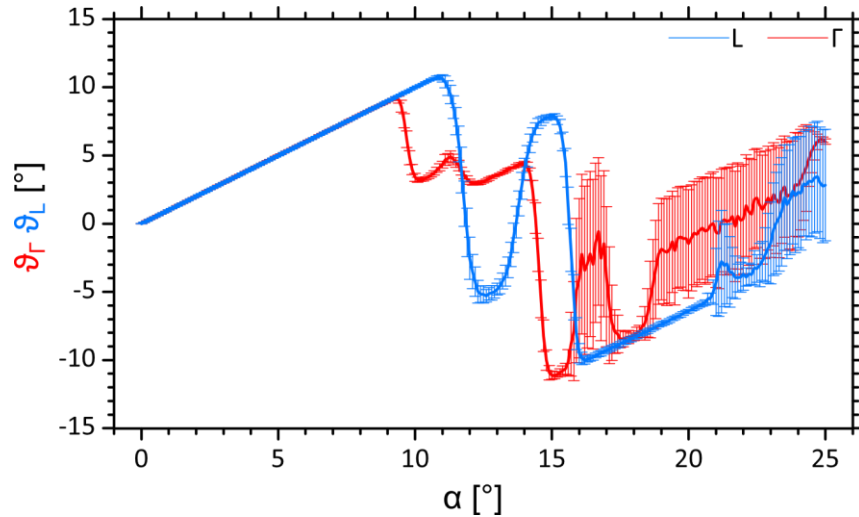


Figure 49: Effective migration angles for Γ and L particles at the point $(d_p/2, d_m/2) = (3.34, 0.1)$ in dependence of different array tilting angles α . An effective window of separation around $\alpha = 15^\circ$ is observable and closer investigated experimentally.

with 100 averaged trajectories per point and particles species (see Figure 49). Here, instead of the effective angle of separation $\Delta\vartheta_{15}$ the absolute migration angles for both species with respect to the x-axis are depicted. From $\alpha = 0^\circ$ to $\alpha = 9^\circ$ the particles essentially follow the axis of the array. Subsequently, three different windows of separation with even different sign of $\Delta\vartheta$ follow from $\alpha = 9^\circ$ to approximately 16° . Around $\alpha = 11^\circ$ and $\alpha = 15^\circ$ the L particles mainly migrate along the array axis and the Γ particles migrate with negative migration angle. On the other hand, around $\alpha = 12^\circ$, the situation is contrary. The Γ particles move along the array axis upwards under a positive migration angle and the L particles move downwards. The third region for $\alpha > 16^\circ$ is characterized by considerably increasing error bars caused by coexistence of more than one migration mode.

With the additional results of Figure 49 in mind, the experimentally realized value of α was fixed to $\alpha = 15^\circ$ because here, a maximum $\Delta\vartheta$ is predicted. This is the main difference to the theoretical work of Speer and coworkers²¹³. In their simulations, spontaneous symmetry breaking for an a priori symmetric environment ($\alpha = 45^\circ$) was observed but no noteworthy chiral separation for much smaller α and thus asymmetric systems. To further verify Figure 49 experimentally and especially the predicted change of sign of $\Delta\vartheta$ around $\alpha = 12^\circ$ a second microfluidic device with $\alpha = 12^\circ$ will be evaluated in a second experiment. With these two values of α the migration behavior of the two particle species was analyzed in more detail (single particle trajectories in Figure 50). While there is optimal separation performance for $\alpha = 15^\circ$ with $\Delta\vartheta_{15} = 18.97^\circ \pm 0.34^\circ$ and 100% correct classification of the particle species, the performance of $\alpha = 12^\circ$ is lower with only

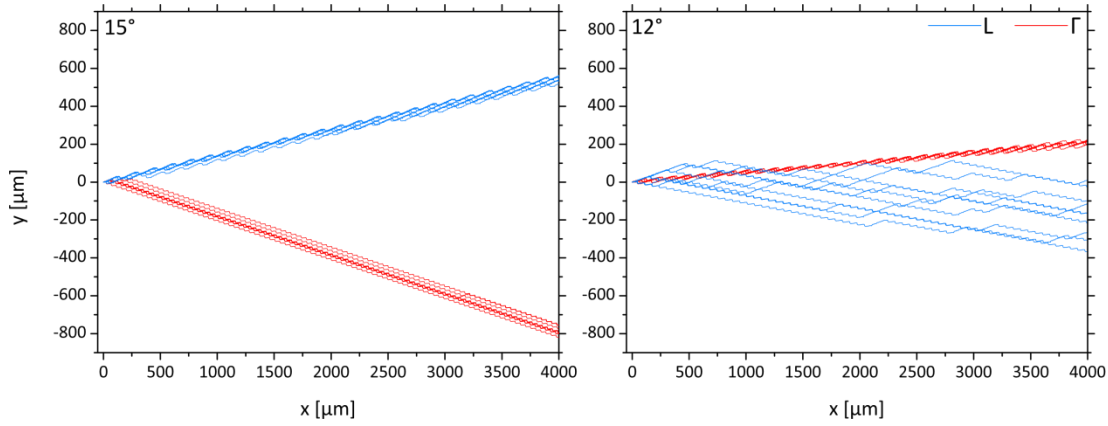


Figure 50: Numerically calculated trajectories of the L (blue) and Γ particles (red) for $\alpha = 15^\circ$ (left) and $\alpha = 12^\circ$ (right). 10 particles of each species were analyzed in detail leading to theoretical separation angles of $\Delta\theta_{15} = 18.97^\circ \pm 0.34^\circ$ and $\Delta\theta_{12} = 5.61^\circ \pm 1.56^\circ$.

$\Delta\theta_{12} = 5.61^\circ \pm 1.56^\circ$ as already anticipatable from the corresponding regions in Figure 49. In conclusion, the theoretical analysis of this separation principle leads to the parameters in Table 10, which are experimentally realized in paragraph 4.3.2.2.

Table 10: Theoretically evaluated parameter set which results in significant values of $\Delta\theta$ and which is experimentally realized in paragraph 4.3.2.2.

Parameter	Symbol	Value
Radius of posts	$d_p/2$	3.34 μm
Radius of monomer	$d_m/2$	0.1 μm
Array tilting angle	α	12°, 15°
Lattice constant of array	l_p	20.5 μm

4.3.2.2 EXPERIMENTAL EVALUATION

The numerically evaluated results from paragraph 4.3.2.1 were used to design a microfluidic experiment, which has already been depicted in Figure 45. It consists of a 1cm long (x direction), 1 mm wide (y direction), and 6 μm high (z direction) microchannel structured with an array of posts with the following measured design parameters (see Table 11). The main experimental result of this project is shown in Figure 51. 10 L and 10 Γ shaped microparticles were transported through the microchannel structured with a fixed array tilted by $\alpha = 15^\circ$. In accordance with the numerical simulations, it could be observed, that the blue L particles are basically following the structure of the post array under an effective

Table 11: Experimental design parameters of the microchannel with structured posts for the separation of chiral microparticles which were quantified with an electron microscope.

Parameter	Symbol	Value
Particle long axis	a	$14.7 \pm 0.3 \mu\text{m}$
Tilting angle	α	$15^\circ, 12^\circ$
Lattice constant	l_p	$20.5 \pm 0.2 \mu\text{m}$
diameter of posts	d_p	$6.68 \pm 0.2 \mu\text{m}$

mean migration angle of $\vartheta_L^{15} = 12.1^\circ \pm 3.5^\circ$ with respect to the x axis of the channel. The red Γ particles migrate through the structure with a mean migration angle with opposite sign of $\vartheta_\Gamma^{15} = -10.7^\circ \pm 0.8^\circ$. Hence, under the given array tilting angle of $\alpha = 15^\circ$, the device splits the trajectories of the chiral microparticles very efficiently with a total angle of separation of

$$\Delta\vartheta_{15} = |\vartheta_L^{15} - \vartheta_\Gamma^{15}| = 22.8^\circ \pm 3.5^\circ$$

without any false results although the post array itself is *not* chiral. Furthermore, Figure 51 demonstrates that after already $\Delta x = 200 \mu\text{m}$ travelled distance which is roughly 14 times the longest dimension of the analyzed particles, a clear separation with baseline resolution was achieved. Compared to microfluidic separation results from other groups, this value is extremely low. The $16 \mu\text{m}$ long helical bacteria of Marcos et al. needed approximately 100 cm for a clear differentiation which is 62500 times the dimension of the considered particles²¹⁷.

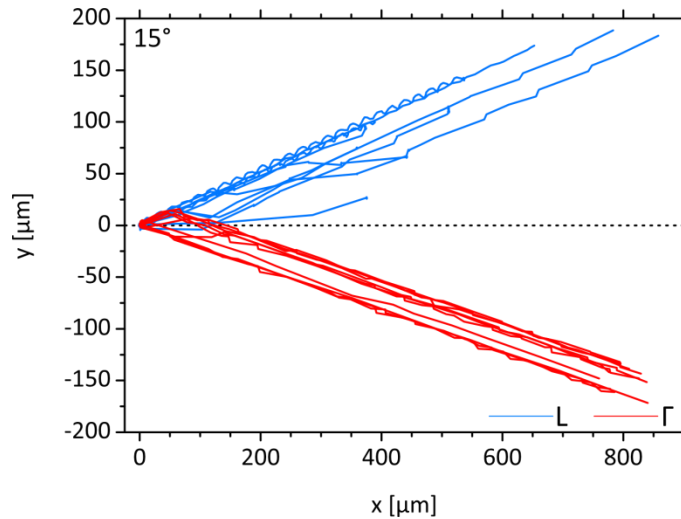


Figure 51: Trajectories of the 10 L (blue) and 10 Γ particles (red) which were observed experimentally in an array with $\alpha = 15^\circ$. The device shows excellent sorting properties with a splitting angle of $\Delta\vartheta_{15} = 22.8^\circ \pm 3.5^\circ$ of the device. Not a single particle was migrating into the wrong direction. However, there is no clear estimate of an actual resolution, because it is a non-constant function of x . Redrawn with data from²³⁶.

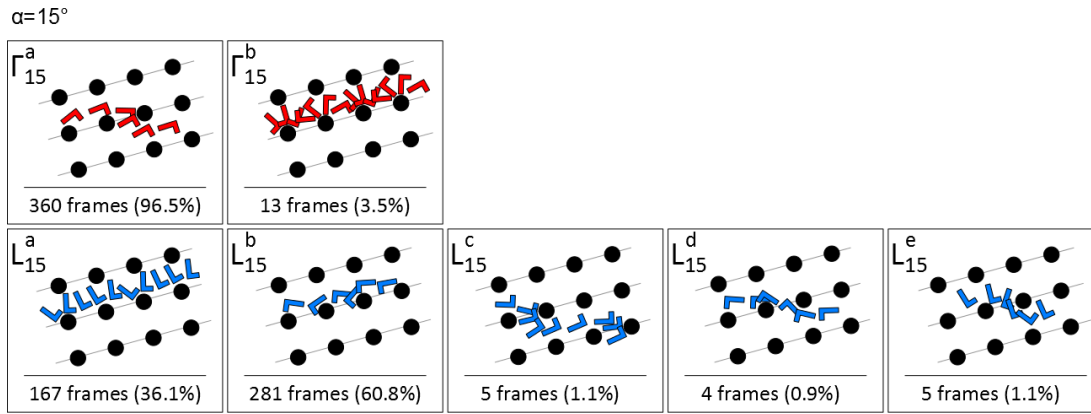


Figure 52: Observed experimental attractors for the case $\alpha = 15^\circ$ for Γ particles (red) and L particles (blue). The frequency of occurrence is denoted in terms of video frames where this certain attractor could be observed. The frame rate is kept constant throughout all experiments. While there are only two distinct attractors observable in case of the Γ particles, the motion of the L particles is governed by five different attractors. However, there are altogether only three predominant attractors which represent 96.5% of all Γ trajectories (Γ_{15}^a) and 96.9% of all L trajectories (L_{15}^a and L_{15}^b).

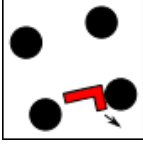
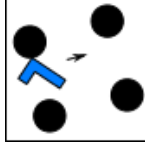
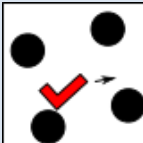

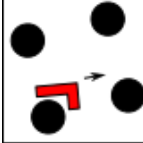

The actual trajectories for $\alpha = 15^\circ$ through the array of posts can be described with a set of attractors (schematically depicted in Figure 52) located in the space of all physical trajectories. The trajectory of a migrating particle with random initial condition concerning location and rotation will almost instantly converge to one of the identified attractors and continue its motion. Two distinct attractors Γ_{15}^a and Γ_{15}^b could be identified for the case of a moving Γ particle where Γ_{15}^a is by far the strongest among them. 360 out of 373 video frames (96.5%) captured of moving Γ particles show a behavior, drawn schematically in the corresponding picture in Figure 52 (top left). Here the short end of the particle collides with a post while the hydrodynamic friction at the long end pulls the particle downwards. As a consequence, all Γ trajectories in Figure 51 have a negative effective angle of migration ϑ_{Γ}^{15} . The very few video frames where behavior according to Γ_{15}^b is observed lead to some small deviations at the beginning only.

The case of the L particles is a little more complex, as it is characterized by two main attractors L_{15}^a and L_{15}^b which together represent 448 out of 462 (96.9%) video frames. In both cases, L particles, that collide with a post further migrate parallel to the array (grey lines in Figure 52) and hence show a positive effective migration angle ϑ_L^{15} under $\alpha = 15^\circ$. The underrepresented attractors L_{15}^c , L_{15}^d , and L_{15}^e lead to some minor deviations.

It is observable that the current migration mode is subjected to changes once in a while (see Table 12). In most cases of the Γ particles for instance, the stable attractor Γ_{15}^a is not reached directly at the beginning of the trajectory. In fact, disadvantageous initial conditions like in cases 1, 2, 4, 5, 7, and 9 lead to an approach towards the weaker attractor

Table 12: Initial conditions and sequences of occurred migration modes (see Figure 52 for details). The number in brackets represents the number of video frames the particle migrated in the given mode.

Γ particles			L particles	
#	Initial condition	Migration mode	Initial condition	Migration mode
1		$\Gamma_{15}^b(2), \Gamma_{15}^a(38)$		$L_{15}^b(159)$
2		$\Gamma_{15}^b(3), \Gamma_{15}^a(38)$		$L_{15}^a(49)$
3		$\Gamma_{15}^a(29)$		$L_{15}^a(3), L_{15}^c(1), L_{15}^a(23)$
4		$\Gamma_{15}^b(4), \Gamma_{15}^a(39)$		$L_{15}^a(1), L_{15}^c(2), L_{15}^a(4),$ $L_{15}^c(2), L_{15}^a(28)$
5		$\Gamma_{15}^b(1), \Gamma_{15}^a(15)$		$L_{15}^d(1), L_{15}^a(19)$
6		$\Gamma_{15}^a(46)$		$L_{15}^a(5), L_{15}^d(1), L_{15}^a(3),$ $L_{15}^b(2), L_{15}^a(2)$
7		$\Gamma_{15}^b(1), \Gamma_{15}^a(40)$		$L_{15}^a(10)$

Γ particles		L particles		
#	Initial condition	Migration mode	Initial condition	Migration mode
8		$\Gamma_{15}^a(22)$		$L_{15}^a(2), L_{15}^b(3), L_{15}^a(3),$ $L_{15}^b(3), L_{15}^a(2), L_{15}^b(2),$ $L_{15}^e(1), L_{15}^a(1), L_{15}^b(1),$ $L_{15}^e(1), L_{15}^a(2)$
9		$\Gamma_{15}^b(2), \Gamma_{15}^a(51)$		$L_{15}^b(109)$
10		$\Gamma_{15}^a(42)$		$L_{15}^c(2), L_{15}^b(2), L_{15}^a(1),$ $L_{15}^e(1), L_{15}^a(1), L_{15}^e(2),$ $L_{15}^a(2)$

Γ_{15}^b instead of Γ_{15}^a . Because the simulated trajectories, where only Brownian motion is accounted for (see section 3.5 and the left part of Figure 50) did not show any attractor changes in the case of $\alpha = 15^\circ$ it can be concluded, that here, a stronger stochastic disturbance, e.g. the collision with the ceiling or the bottom of the channel is required for the trajectory to change the attractor. The particles made out of SU-8²³⁷ (density 1190 kg/m³) have a slightly higher density than water at room temperature⁵⁰ (density 1003 kg/m³). Consequently during their motion through the channel these particles will slowly sediment to the channel floor. On the other hand, Brownian motion will oppose this motion and might hinder the particles from hitting the channel bottom. Faucheux and Libchaber investigated this problem for spherical objects and demonstrated that Brownian motion in confined spaces under the influence of gravity results in a non-vanishing mean vertical position of the particle over ground²³⁸. In their publication, spherical particles with diameters between 1 and 3.5 μm with a slightly lesser density of 1050 kg/m³ in equally high channels were considered among others which showed a mean height over ground between 2.4 and 2.8 μm . However, the particles considered in the present experiment are denser and show much less diffusion. In fact, diffusion is even unobservable under the microscope. Thus, the assumed interaction with at least the floor of the channel is quite likely. Furthermore slight deviations in the channel structure could be sufficient as well. On

the other hand, Γ_{15}^a is stable enough, so that there are no reoccurrences of Γ_{15}^b once Γ_{15}^a has been reached.

For the L particles, the situation is more complex. Again depending on the initial conditions trajectories select the closest corresponding attractor and then change to L_{15}^a or L_{15}^b after a while. However, in the case of the L particles these two attractors seem weaker compared to the disturbance effects and hence, further reallocations (up to ten) were observed.

As already predicted by the numerical simulations in paragraph 4.3.2.1, a slight change of the array tilting angle α can have a tremendous impact on the separation characteristics and performance. To verify this prediction experimentally, a similar microfluidic channel with $\alpha = 12^\circ$ instead of $\alpha = 15^\circ$ has been considered as well.

The experimental results for $\alpha = 12^\circ$ are depicted in Figure 53 where the trajectories of 7 L and 8 Γ particles could be recorded. Although the array tilting angle α has been changed only by three degrees, the separation result is significantly different and worse compared to the case $\alpha = 15^\circ$. Here the L particles move under a mean deflection angle of $\vartheta_L^{12} = -1.8^\circ \pm 4.0^\circ$ and the Γ particles with $\vartheta_\Gamma^{12} = 4.0^\circ \pm 4.6^\circ$. From these values, the mean angle of separation is only

$$\Delta\vartheta_{12} = |\vartheta_L^{12} - \vartheta_\Gamma^{12}| = 5.8^\circ \pm 6.1^\circ.$$

In addition to the smaller $\Delta\vartheta_{12}$, there are further differences to the previously discussed case as the signs of ϑ_L^{12} and ϑ_Γ^{12} are swapped. This time, the (red) Γ particles travel along

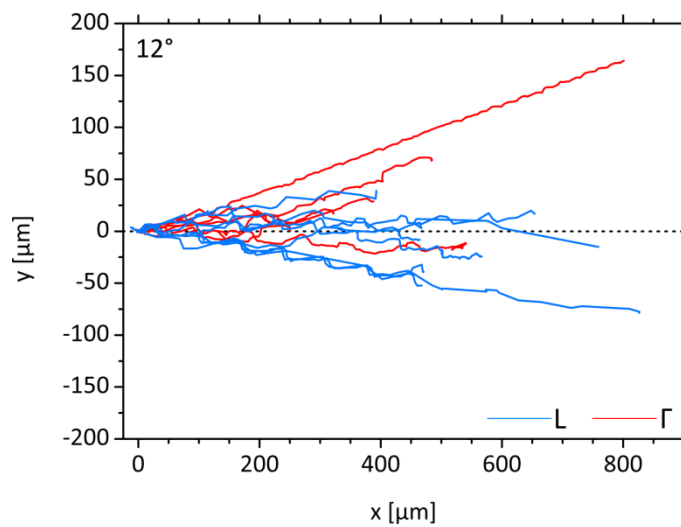


Figure 53: The same experiment as in Figure 51 but with $\alpha = 12^\circ$ instead of $\alpha = 15^\circ$ for 7 L and 8 Γ particles. The change of the array tilting angle has led to a significant change of the sorting performance. This separation attempt lead to a poor splitting angle of only $\Delta\vartheta_{12} = 5.8^\circ \pm 6.1^\circ$.

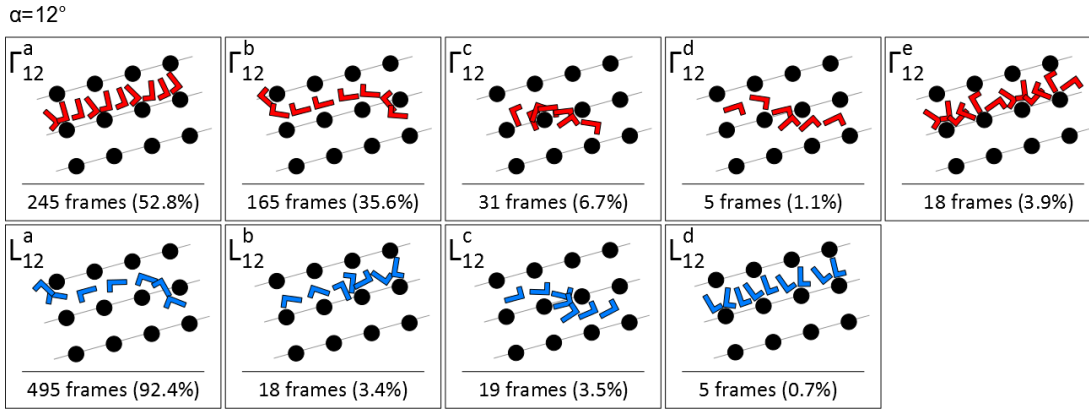


Figure 54: Observed experimental attractors for the case $\alpha = 12^\circ$ for Γ particles (red) and L particles (blue). The frequency of occurrence is again denoted in terms of video frames where a certain attractor could be observed. The most important difference besides the three additional Γ trajectories and the missing fifth L trajectory are the existence of multiple dominant attractors resulting in migration angles with different sign (Γ_{12}^a and Γ_{12}^b).


the post array with positive ϑ_{Γ}^{12} and the L particles migrate through the array downwards with negative ϑ_L^{12} as predicted by the simulation in paragraph 4.3.2.1.

Further differences can be extracted from Figure 54. Instead of two Γ and five L attractors, there are now five Γ and four L attractors. Instead of one dominant Γ and two dominant L attractors, the situation is opposite, because now two dominant Γ and only one dominant L attractor are present. Furthermore this time the migration angles of the two dominant Γ attractors have *different* signs. While trajectories following Γ_{12}^a proceed along the array (grey lines), the Γ_{12}^b trajectories pass the grey lines and migrate through the structure. This is the cause of the larger error of ϑ_{Γ}^{12} compared to ϑ_{Γ}^{15} .

Table 13 shows the observed migration modes of the Γ and L particles and the corresponding initial conditions. Here in the case of $\alpha = 12^\circ$ both Γ and L trajectories change their attractors more often than for $\alpha = 15^\circ$. It seems, that for smaller α and hence less chiral environments, not only the already discussed collisions with the channel's ceiling or bottom (which is supposed to be equal here) play an increasingly important role, but also the disturbing effects of Brownian motion. This claim is supported by the right part of Figure 50 where only Brownian motion as a possible disturbance is accounted for. While for $\alpha = 15^\circ$, the considered Brownian motion did not lead to any significant changes of the corresponding attractors, thermal noise is now strong enough to regularly disturb the process of a given trajectory experimentally as well as theoretically.

Table 13: Initial conditions and sequences of occurred migration modes (see Figure 54 for details). The number in brackets represents the number of video frames the particle migrated in the given mode. “undef” means, that the current mode of migration could not be clearly identified because of bad image quality.

Γ particles			L particles	
#	Initial condition	Migration mode	Initial condition	Migration mode
1		$\Gamma_{12}^a(144)$		$L_{12}^a(11), L_{12}^b(3), L_{12}^a(13),$ undef (7)
2		$\Gamma_{12}^b(78), \Gamma_{12}^c(7), \Gamma_{12}^a(14)$		$L_{12}^a(46), L_{12}^b(12),$
3		$\Gamma_{12}^a(15), \Gamma_{12}^b(43),$		$L_{12}^a(17), L_{12}^b(3)$
4		$\Gamma_{12}^a(9), \Gamma_{12}^b(4), \Gamma_{12}^a(4),$ $\Gamma_{12}^b(3), \Gamma_{12}^a(9)$		$L_{12}^c(5), L_{12}^a(4), L_{12}^c(6),$ $L_{12}^d(4), L_{12}^a(8), L_{12}^c(8),$ $L_{12}^a(12),$
5		$\Gamma_{12}^b(33), \text{undef}(3)$		$L_{12}^d(124)$
6		$\Gamma_{12}^a(16), \Gamma_{12}^c(4), \Gamma_{12}^d(5),$ $\Gamma_{12}^c(20)$		$L_{12}^a(87)$
7		$\Gamma_{12}^a(21), \Gamma_{12}^b(4), \Gamma_{12}^a(13),$ $\Gamma_{12}^e(18)$		$L_{12}^a(41)$

Γ particles			L particles	
#	Initial condition	Migration mode	Initial condition	Migration mode
8				$L_{12}^{\alpha}(132)$

4.3.2.3 COMPARISON OF NUMERICAL SIMULATION AND THE EXPERIMENT

In the previous paragraph, it was shown that the numerical simulations qualitatively reproduce the experimental data quite well (especially for $\alpha = 15^\circ$) as the sorting behavior itself and the correct signs of the migration angles ϑ_L^{15} and ϑ_Γ^{15} as well as ϑ_L^{12} and ϑ_Γ^{12} were predicted correctly. This paragraph provides a closer quantitative comparison between experiment and simulations concerning a) the resulting migration angles ($\vartheta_L^{15}, \vartheta_\Gamma^{15}, \vartheta_L^{12}, \vartheta_\Gamma^{12}$) and the effective angles of separation $\Delta\vartheta_{15}$ and $\Delta\vartheta_{12}$ and b) the reproduction of the observed attractors of migration.

Table 14 summarizes the obtained values for the angles of migration and the angles of separation from the numerical and the experimental analysis. In all cases with the exception of ϑ_L^{15} the theoretical value is located within the σ interval of the corresponding experimental value. The deviation for ϑ_L^{15} is significantly larger but can still be found within the 2σ regime of the experimental value. Generally, the obtained experimental errors are

Table 14: Comparison of experimental and theoretical angles of migration for $\alpha = 12^\circ$ and $\alpha = 15^\circ$. The numerical data is gathered by averaging over 100 trajectories per particle species and value of α . The experimental values are identified accordingly with all available experimental trajectories and the statistical errors are the corresponding standard deviations or calculated according to the Gaussian error analysis respectively.

Parameter	Experiment	Simulation
ϑ_Γ^{12}	$+ 3,98^\circ \pm 4,60^\circ$	$+ 3,07^\circ \pm 0,19^\circ$
ϑ_L^{12}	$- 1,78^\circ \pm 3,93^\circ$	$-2,54^\circ \pm 1,55^\circ$
$\Delta\vartheta_{12}$	$5.76^\circ \pm 6.05^\circ$	$5,61^\circ \pm 1,56^\circ$
ϑ_Γ^{15}	$-10,66^\circ \pm 0,75^\circ$	$-11,11^\circ \pm 0,30^\circ$
ϑ_L^{15}	$+12,10^\circ \pm 3,45^\circ$	$+ 7,86^\circ \pm 0,16^\circ$
$\Delta\vartheta_{15}$	$22.76^\circ \pm 3.53^\circ$	$18.97^\circ \pm 0.34^\circ$

larger than their numerical counterparts. The reason can be found with a closer inspection of the trajectories in Figure 50, Figure 51, and Figure 53. Large deviations in the resulting angle of migration are generated when particles switch their attractor of migration as demonstrated e.g. for the L trajectories in Figure 51 experimentally. As already stated for $\alpha = 15^\circ$ the experimental attractors are so strong, that Brownian motion alone is too weak to induce attractor changes because no changes can be found in the simulation. Consequently, the experimental particles must have been subjected to even stronger stochastic disturbances e.g. a collision with ceiling or floor of the channel which are omitted in the simulation. Thus, the resulting experimental error is larger. For $\alpha = 12^\circ$ Brownian motion is just strong enough to induce significant disturbances that result in changes of attractors at least for the L particles (see Figure 50) because now, these disturbances can be seen even in the theoretical results. However, disturbances in the experiment (e.g. collisions with ceiling or floor) are still dominant and hence the experimental error is again larger than the theoretical error.

The exact numerical prediction of separation angles is most important for an experimental reproduction and further technological use of the presented principle. However, a closer comparison of the experimentally and theoretically observed attractors of migration is also adjuvant to further judge the quality of the applied numerical model. Figure 55 shows stroboscopic image series of the actual movement of L and Γ particles in the array of posts

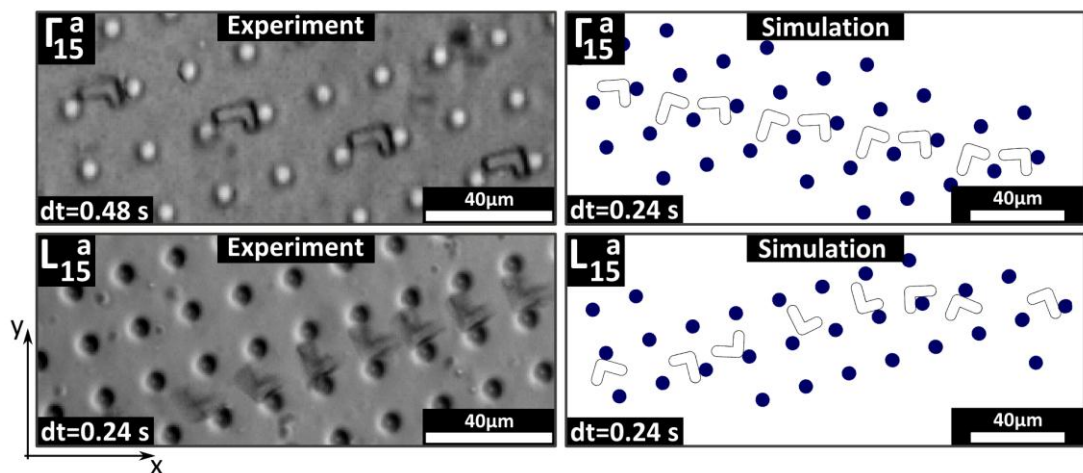


Figure 55: Stroboscopic images of the attractor Γ_{15}^a (see Figure 52) observed in the experiment (top left) and in the simulation (top right) for $\alpha = 15^\circ$. The two lower panels show the attractor L_{15}^a . While the prediction of Γ_{15}^a is perfect in the simulation, the situation for L_{15}^a is not that clear. Note the different value for dt in the left upper image because of non-optimal image quality. All images were generated with the GIMP layer effect “darken only”, were a stack of images is properly aligned manually and the resulting image is generated by using the darkest color value for every pixel which can be found in all stacked images at this position. The contrast of the experimental images is later adjusted with GIMP’s brightness & contrast tool.

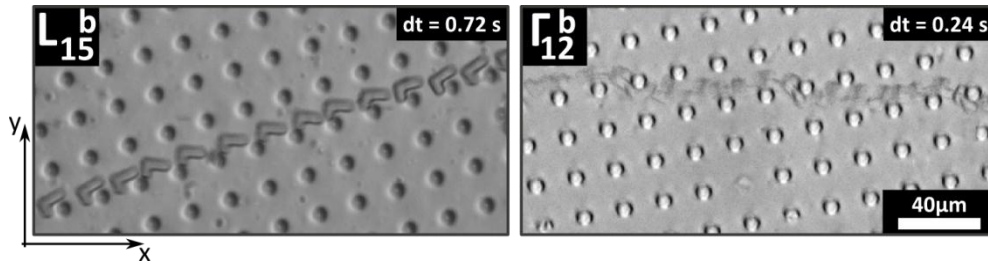


Figure 56: Stroboscopic images of the two attractors L_{15}^b and Γ_{12}^b which occur quite often in the experiment but for which no numerical counterpart could be found.

for $\alpha = 15^\circ$ and their theoretical counterparts while being attracted by the two prominent attractors Γ_{15}^a and L_{15}^a . The simulation predicts the movement of the Γ particles perfectly. Even the spatial periodicity of the particle movement (2 elementary cells) is calculated correctly according to the experiment. On the other hand the attractor L_{15}^a shows slight differences between the experimental and the theoretical result. While the L particle moves straight along the inclined row of posts during the experiment, the simulation shows regular deviations from that behavior. Here, the L particle passes the row roughly every ten elementary cells. As a result, the obtained values for ϑ_L^{15} from the experiment and the simulation are equal only within the 2σ regime of the experimental value (see Table 14). The experimentally rarely observed attractors Γ_{15}^b , L_{15}^c , L_{15}^d , and L_{15}^e could not be observed in the simulation. These might have their origin in the already discussed disturbances because a particle hits the channel floor or the ceiling. However, there is an experimentally quite prominent attractor L_{15}^b which could not be observed in the simulation as well (left image in Figure 56).

The situation for $\alpha = 12^\circ$ is quite similar. Figure 57 compares the two experimentally most prominent attractors Γ_{12}^a and L_{12}^a to the corresponding numerical predictions. In this case, the behavior of the L particles is perfectly predicted by the simulation and even the spatial periodicity of the motion (3 elementary cells) is calculated correctly. While the experimental trajectory of the Γ particles is straight along a row of structured posts, the numerical analysis shows regular deviations from this behavior as particles sometimes pass the row and then migrate further along the array. As a result the numerical and experimental results for ϑ_{12}^Γ differ by nearly 1° which is, however, still within the experimental error.

A third attractor Γ_{12}^b that is still occurring quite regularly in the experiment could not be predicted by the theory as shown in the right part of Figure 56. Like for $\alpha = 15^\circ$ the very

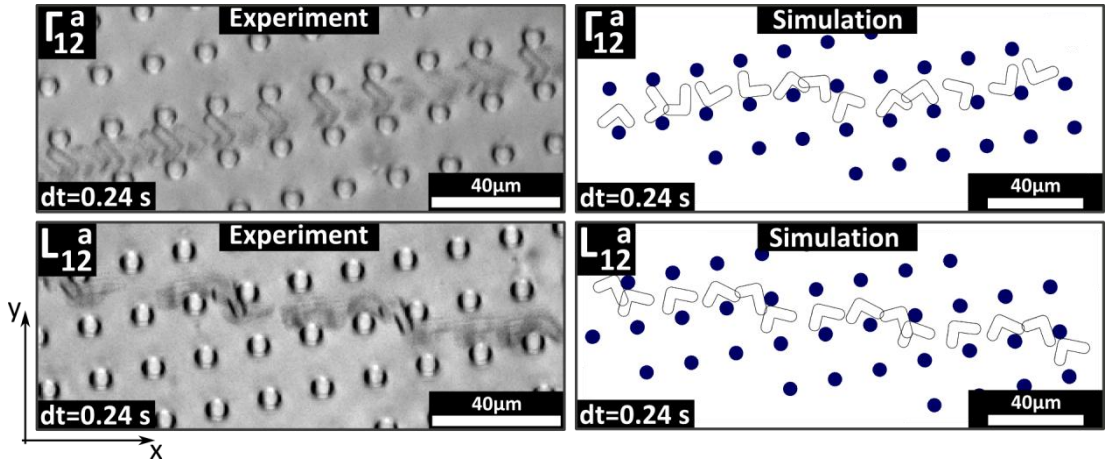


Figure 57: Stroboscopic images of the attractor Γ_{12}^a (see Figure 54) observed in the experiment (top left) and in the simulation (top right) for $\alpha = 12^\circ$. The two lower panels show the attractor L_{12}^a . While the prediction of L_{12}^a is perfect in the simulation, the numerically evaluated behavior of the Γ particle in the upper two images is slightly different compared to experiment. The images were generated as described in the caption of Figure 55.

rarely observed experimental attractors Γ_{12}^c , Γ_{12}^d , and Γ_{12}^e as well as L_{12}^b , L_{12}^c , and L_{12}^d could not be predicted in the simulation. Their very sporadic occurrence in the experiment and their absence in the simulation can again be interpreted as disturbance induced by imperfections of the channel geometry or collisions with the floor or ceiling of the channel.

The numerical simulations were originally conducted to quickly identify possible design parameters for an optimal experimental realization. With these guidelines in mind, the theoretical model behind the presented simulations (see section 3.5) contains the following approximations to be as economic as possible concerning development and computing time but precise enough for correctly identifying a working design:

1. The simulation is purely two dimensional, which means that the interaction of a particle in z direction with the ceiling or the floor of a microchannel is neglected. This could be the reason, why the experimentally rarely occurring attractors $\Gamma_{15}^b, L_{15}^c - L_{15}^e$ and $\Gamma_{12}^c - \Gamma_{12}^e, L_{12}^b - L_{12}^d$ which might be induced by such a collision with ceiling or floor are not present in the simulation as thermal noise alone is too weak to overcome the dominant attractors in most cases.
2. The structure of the microchip deviates from a perfect array with posts of equal size and shape. Small imperfections and defects as well as deviations from the prospected dimensions lie within the nature of the soft lithography process and could not be further reduced. On the other hand, the data presented in Figure 46, Figure 47, and Figure 48 shows that slight deviations from optimal values may lead

to significantly different migration behavior. Such randomly appearing faults in the geometry are presently not included in the model.

3. Although the actual force field, that drives the monomers of a particle is obtained by solving the Navier-Stokes-equation for a given elementary cell, the influence of the particle on the flow field is not accounted for because then one would have to solve the flow equations not just once but for every time step. This is a very time and resource consuming endeavor and hence practically unfeasible.

However, the predicted window of separation from Table 10 yielded excellent separation results for $\alpha = 15^\circ$ in the experiment. In fact, not a single particle was sorted incorrectly. Furthermore the predicted angles of separation could all be confirmed by the experiment (see Table 14) with the exception of ϑ_{15}^L which nevertheless still lies within the 2σ regime of the corresponding experimental value.

4.3.3 CHIRAL SEPARATION WITH STRUCTURED SIDEWALLS

In this paragraph, a second approach demonstrating enantioselective separation of chiral objects based on the systematic breaking of relevant spatial symmetries is discussed. Instead of exploiting the direct interaction of the model particles with certain asymmetric channel structures, it is also sufficient to break the symmetry of the otherwise typical parabolic flow profile through the microchannel (see paragraph 2.1.2 and especially Figure 4)^{215,216}. Chiral microparticles transported within such a shear flow are shown to accumulate near opposite sidewalls.

The experimental realization of this principle is displayed in Figure 58. A 16 mm long (x direction) and 6 μm high (z direction) straight microchannel connects two fluid reservoirs with a diameter of 2 mm. To introduce the broken symmetry of the flow profile, one sidewall of the channel is structured with triangles so that the overall 70 μm wide (y direction) channel is periodically constricted to a total width of 40 μm (periodicity: 50 μm). The fluid within the channel is transported with a pressure gradient $\Delta p \approx 20$ mbar created by a self-constructed pneumatic precision pump (see Appendix A1), that is connected with silicone tubing to both reservoirs.

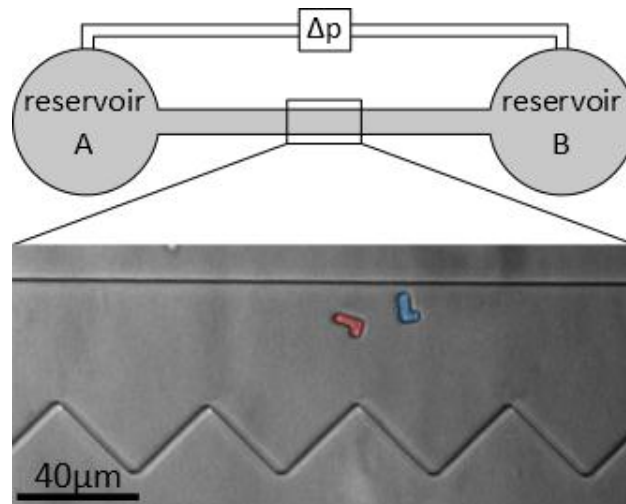


Figure 58: Schematic and a micrograph of the microfluidic setup used for the chiral separation with a structured sidewall. A 16 mm long (x direction), 40-70 mm wide (y direction) and 6 μm high (z direction) microfluidic channel connects two fluidic reservoirs where the particle solution is filled in before the experiment. A pneumatic precision pump (see Appendix A1) is attached with silicone tubes to both reservoirs and creates a pressure gradient to transport the fluid through the channel. The symmetry of the typically parabolic flow profile which leads to the desired particle separation is broken by the triangularly structured sidewall.

A sufficiently low concentrated solution of 3 μm high chiral testparticles with $a = 8.95 \mu\text{m} \pm 0.3 \mu\text{m}$ and $b = 6.34 \mu\text{m} \pm 0.3 \mu\text{m}$ is injected into the fluidic reservoirs. Like already discussed in the previous paragraph 4.3.2 the experiment can be regarded as quasi two dimensional because the channel is adequately flat so that the particles cannot rotate along their long axis and hence their chirality is maintained.

4.3.3.1 HYDRODYNAMIC FLOW PROFILE

Figure 59 shows the experimentally obtained effective flow profile through the channel averaged over one period of triangles. The triangles are located in the region of negative y values. The plot shows, that the flow profile is clearly asymmetric as required. The shear flows occur in regions with a width of approximately 10-15 μm around $y = -10 \mu\text{m}$ and $y = 35 \mu\text{m}$. This width corresponds to the dimensions of the microparticles so that they optimally couple to the shear flow field without losses or overcompensation.

However, the walls show significant artificial slip length due to the finite size of the tracer particles and their resulting inability to move sufficiently close to the walls. Although the channel is isotropic along the z-axis, there are still no-slip conditions occurring at the bottom and at the ceiling of the channel and thus a parabolic profile along the z-axis is present (cf. Figure 4). The flow speed is thus homogenously reduced over the whole width in y direction of the channel. Hence, the microscope focus was placed approximately

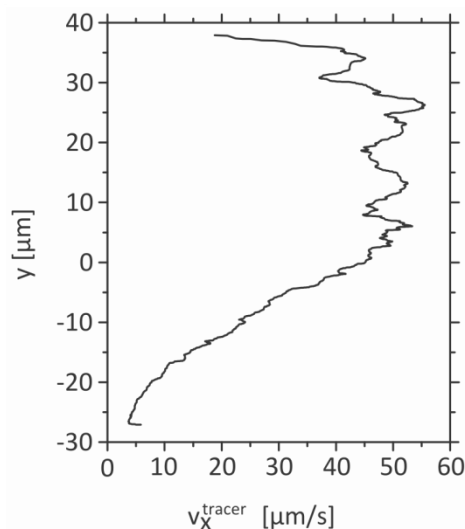


Figure 59: Flow profile of the hydrodynamic flow created by the triangular sawtooth structure of the considered micro channel (data smoothed). 75 trajectories of fluorescent tracer particles ($\phi=0.5 \mu\text{m}$) with velocity v_x^{tracer} and with approximately 25 data points each were considered. Because of the very low Reynolds numbers, the system operates free from inertia and the particles thus always adopt the velocity of the surrounding medium immeasurably fast. The structure is located where $y < 0$. The asymmetry is clearly visible and sufficient for baseline separation as shown below.

between floor and ceiling, so that unfocused particles near the boundaries were not considered for evaluation. However, this effect would only rescale the shown flow profile and not alter its characteristic shape.

4.3.3.2 EXPERIMENTAL EVALUATION

The enantioselective separation experiments are invoked by injecting the particle analyte solution into one reservoir and filling the other reservoir with deionized water. The particles which are at this time still all identical select their chirality when they get injected into the main channel because the $3 \mu\text{m}$ high micro particles cannot rotate along their long axis to change their chirality in a $6 \mu\text{m}$ high channel once they leave the reservoir. Now, one particle is selected and transported back and forth through the whole channel and tracked via video microscopy. As the field of view is too small for the observation of the whole channel, the microscopy stage is moved at a constant velocity and the number of covered triangles is counted for later coordinate correction. It was furthermore taken advantage of the effect, that one and the same particle controllably changes its chirality without rotation when the direction of migration changes due to symmetry reasons. Therefore, transporting one particle back and forth through the channel to generate statistically sufficient realizations is sufficient and desired for reasons of reproducibility. Hence, one does not

have to deal with minimal deviations of the particle geometry, that could have an influence on their actual behavior and the experimental procedure is alleviated. However, in the following the expression L and Γ particles are still used for reasons of readability although only one single particle, pumped back and forth is actually considered.

Figure 60 shows the main result, where 16 effective L trajectories (blue) and 18 effective Γ trajectories (red) could be recorded. All absolute x coordinates were transformed to relative coordinates, so that every trajectory starts at $x=0$ and the corresponding unchanged y value and all particles move effectively move from left to right.

There is no argument why asymmetrical particles like the considered L and Γ particles should move with the same velocity vector \vec{v}_p in an asymmetric environment^{26,213}. Hence, due to their interaction with the asymmetrically engineered flow profile within the channel (Figure 59) the particle species split up and approach different attractors according to their chirality. The L species (blue) accumulates near the structured sidewall, whereas the Γ species (red) is attracted by the flat wall in all cases. There is no explicit false classification of particles by the device within these 34 realizations, although there are three particles (one L and two Γ) which show no action because they were already at the right y position

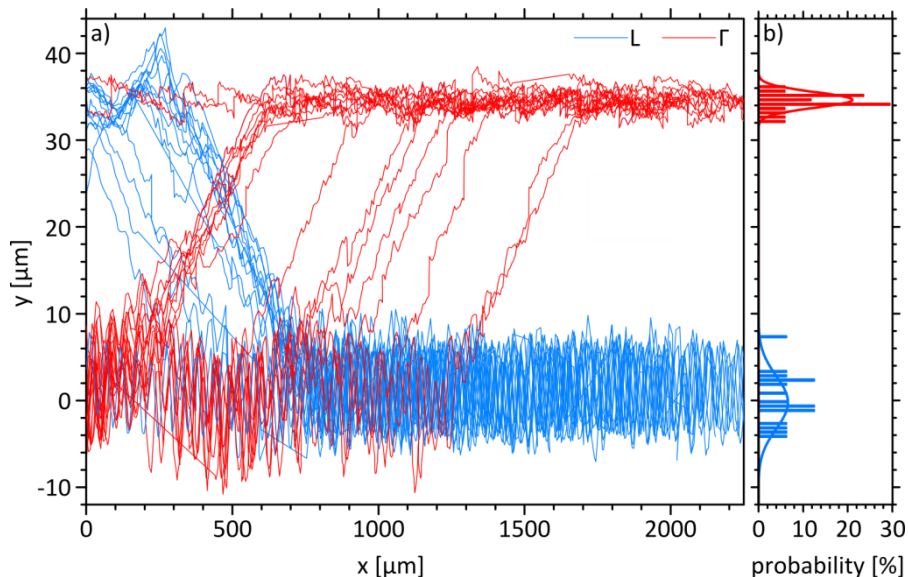


Figure 60: a) Experimental trajectories of 16 L particles (blue) and 18 Γ particles (red). After roughly 2000 μm of covered distance in x direction, the particles have split up according to their chirality (attractor of L near the structured sidewall and attractor of Γ on the opposite wall.) Some particles are already at the correct position and thus show no action. There is no explicit false classification of any particle. Redrawn with data from²³⁹. b) Histogram plot along the line $x = 2000 \mu\text{m}$ to demonstrate the resolution of the separation concept. Because the Γ particles are moving along the flat wall, the red peak is thinner than the blue peak. The L particles move in the vicinity of the triangular structure and therefore have a non-vanishing y component in their velocity. The resolution of this separation is 3.75.

before the experiment started. Furthermore, Figure 60 demonstrates that all particles have been sorted after they travelled a distance of only $\Delta x = 2000 \mu\text{m}$ in x direction which is 133 times the longest dimension of the particles. Compared to experimental microfluidic separation results from other groups, this value is extremely low. The $16 \mu\text{m}$ long helical bacteria of Marcos et al. needed approximately 100 cm for a clear diffraction which is 62500 times the dimension of the considered particles²¹⁷.

Separation efficiency

From Figure 60 one can already infer, that the presented separation concept is quite efficient in terms of correct selection of particles. The histogram plot in Figure 60 b) along the line $x = 2000 \mu\text{m}$ further supports this claim.

Both species have clearly been baseline separated into distinct streams. Splitting up the microchannel at $x = 2000 \mu\text{m}$ and $y = 20 \mu\text{m}$ into two distinct channels would lead to a collection of the particles in different reservoirs. However, the blue peak is broadened due to the triangular structure at this side of the channel. The particles do not accumulate in the vicinity of a flat wall but enter the space between the triangles disturbing their trajectory because they have a non-vanishing y component in their velocity.

The resolution of this separation can be calculated via

$$R = \left(\frac{y_{\max}^{\Gamma} - y_{\max}^L}{\text{FWHM}^{\Gamma} + \text{FWHM}^L} \right) = 3.75$$

where $y_{\max}^{\Gamma} = 34.6 \mu\text{m}$ and $y_{\max}^L = -0.2 \mu\text{m}$ are the peak positions of the Γ and the L particles respectively and $\text{FWHM}^{\Gamma} = 2.1 \mu\text{m}$ and $\text{FWHM}^L = 7.2 \mu\text{m}$ are the full width half maximum values of both peaks.

However, one has to keep in mind, that the actual resolution is not necessarily a function of the channel width. For the separation mechanism to work, the y dimension of the triangular side structure has to be rescaled with the channel width. Otherwise, the asymmetric flow profile would be deformed as well and the shear gradients could be reduced lowering separation performance. The broadening of the triangular structure would thus lead to a broadening of the blue peak in Figure 60 b) and thus to an approximately constant resolution when broadening the channel width.

Migration behavior

Migration velocity. So far, only the transverse migration of the microparticles in y direction has been studied. With a continuously working separation device in mind, this mode of operation is most practical. However, there is also a temporal resolution observable (Figure 61) which could be theoretically predicted^{215,216}. From Figure 59 one can already infer, that the flow speed near the flat wall is larger, than in the triangularly structured regime. If the selection process of a microparticle is over, the microparticles migrate exactly in these regimes. The result is a difference in migration speeds of approximately 13 per cent.

Further analysis of Figure 61 reveals that the flow speed of the surrounding medium (measured with tracer particles) is nearly twice as fast as the migration speed of the particles. Since the system operates with very small Reynolds numbers, there is no inherent inertia in the system. Therefore, the particles should immediately adopt the speed of the medium. The only reason for the observed deceleration can be a permanently acting force on the particles for example their sporadic friction with the bottom or the ceiling of the microchannel. Since the density of SU-8 is higher than water, the particles will sediment. This effect is compensated by Brownian motion. However, this effect is fairly low as diffusion of the chiral particles is not observable under the microscope (cf. paragraph 4.3.2.2). Hence, it is very likely, that the particles will collide with the bottom from time to time leading to a reduction of their mean velocity. The stochastic influence of this friction is

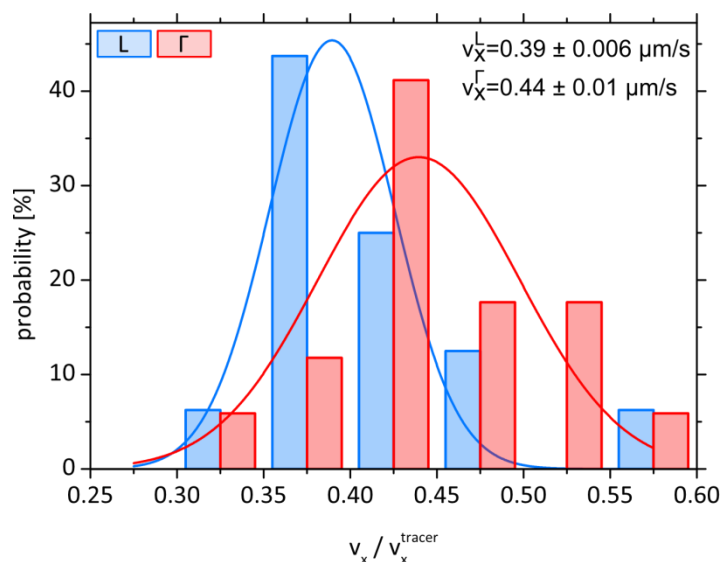


Figure 61: Effective migration velocities of the considered L and Γ particles in x direction. Because of small leakages in the tubing, the actual speed of the liquid in the channel is not exactly controllable. Hence, tracer particles have been added to the medium as described above and the migration velocities of the particles have been normalized with the x component of the speed of the tracers. The result is a small difference in migration velocity which could already be suspected in Figure 59.

not very dominant in view of complete particle trajectories (see Figure 60). The sorting mechanism itself still seems to be stronger because there are no large fluctuations in the trajectories and particles leaving their attractor were not observed. An alternative explanation could be the fact, that the fluid velocity is not homogeneously distributed along the z-axis (cf. Figure 4). The channel is roughly twice as high as the chiral particles. Therefore, particles that somehow sediment might experience a slower hydrodynamic flow and their migration speed is thus lower.

Attractor allocation. The separation of the chiral microparticles is a complicated interplay between the asymmetric structure of the particles and the engineered asymmetric flow profile. At some point during their trajectory through the channel, one of the two available attractors, either the flat or the structured sidewall prevails and thus attracts the particle. Within this context, Figure 62 reveals an overview over the distances Δx , a certain particle needs to travel along the channel before it is fully attracted by its attractor. The three particles that were already close to the correct attractor were omitted in this overview.

Figure 62 shows, that the L particles start migrating towards their attractor before they have travelled a distance of only 600 μm which is approximately 66 times the particle dimension. There are no significant deviations in this aspect. However, there are quite large variations in the group of the Γ particles. Approximately only one half of them have started to head for their corresponding attractor, before the mark of 600 μm . In fact, it takes up to approximately 1400 μm until all particles were sufficiently affected by the shear flow. This behavior can be explained with the predominant asymmetric flow shown in Figure 59. The

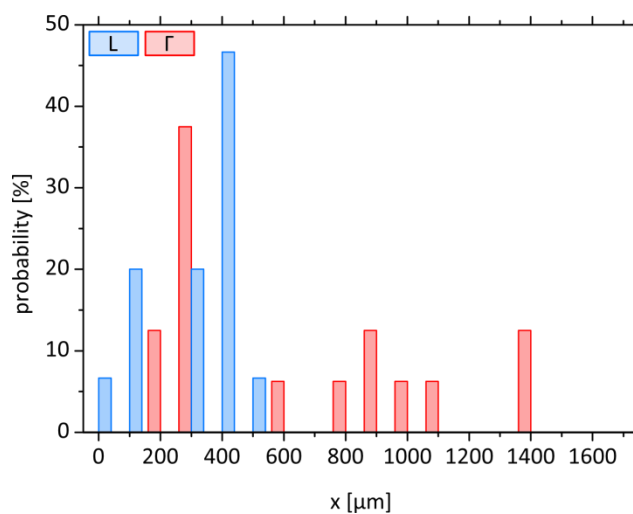


Figure 62: Analysis of the distance in x direction a particle needs before approaching its certain attractor, either the flat sidewall or the structured sidewall. Although there is no huge difference the Γ particles need a little more traveling distance than the L particles although they have a larger mean velocity.

gradient of the shear flow is much smaller on the structured sidewall ($y < 0$) than on the flat sidewall. Most of the Γ particles were located near the triangular wall before the actuation was switched on. As a result, the shear forces a particle is subjected to are smaller. On the other hand, the L particles are subjected to a much larger shear gradient resulting in quicker reaction to the asymmetric actuation by this species. From these facts, one may conclude that the separation mechanism is based on the occurrence of shear gradients and that the strength of these gradients corresponds to the separation efficiency.

4.3.4 COMPARISON OF THE TWO APPROACHES

Two conceptually different microfluidic approaches to continuously separate chiral model enantiomers from each other were presented and discussed in detail in this section. Both approaches require a microfluidic environment of comparable complexity with somehow broken symmetry in every relevant dimension, either introduced with a tilted (symmetric) array of structured posts (Principle A, paragraph 4.3.2) or by a single structured sidewall that creates shear flows (Principle B, paragraph 4.3.3) (cf. Figure 40 and Figure 41). In both cases, the particles are actuated by a hydrodynamic flow of the carrier solution through the channel. However, the resulting forces on the particles in y direction are induced differently. While the particles according to principle A directly hit the hard walls of the integrated channel structure, principle B employs the soft interaction of the particles with the induced shear flow of the carrier medium.

Both approaches worked very robust and separated the model enantiomers continuously while no explicit false classification of particles could be observed (compare Figure 51 and Figure 60). However, the differently intense interactions between the particle and the asymmetric environment employed in principles A and B redound to different overall separation performances. While the intensive interactions with the hard walls of the closely structured posts lead to an overall traveling distance of only 200 μm before the particle streams can be clearly differentiated, the softer interaction of the particles with the hydrodynamic shear flow requires at least 1800 μm for a clear separation. Both values are nevertheless orders of magnitude shorter, than comparable experimental microfluidic approaches²¹⁷.

The excellent (roughly) 10 fold better density of separation performance of principle A in contrast to principle B comes along with certain drawbacks concerning a potential practical

realization on the molecular scale. Because of the very narrow gaps, especially for the suboptimally working case $\alpha = 12^\circ$, some particles got stuck between two posts from time to time. Furthermore the corresponding numerical analysis (see e.g. Figure 46 and Figure 49) predicts that the slightest changes of the surrounding geometry can have a large impact on the separation result. In turn, this means, that a certain device requires a precise adaption to the desired analyte before a separation can take place. From an experimental point of view, the explicit realization of such a small regular post array is currently a very complicated endeavor. On the other hand, the less complex but also slightly less efficient principle B did not suffer from these limitations and could therefore be a more promising candidate for further downscaling.

The currently used microparticles showed excellent coupling to the hydrodynamic shear flow field for principle B. However, the question remains whether such a coupling would be as effective when the device is downscaled to the actual molecular scale. While the microparticles showed no measurable diffusion, real molecules are subjected to very considerable Brownian motion. In theory, the larger coefficients of diffusion can be compensated by increasing the driving speed, so that the Péclet number is kept constant (see section 2.3). Hence, the current relative magnitude of diffusion with respect to the flow speed is maintained. However, at very small scales, this might require quite significant applied hydrodynamic pressures. On the other hand, from the perspective of a small molecule, the ambient water consists of single dipolar molecules that cannot be considered as a continuous fluid anymore. If the chiral analytes are charged, they will even acquire a hydrate hull fixed by hydrogen bonds. These effects might conceal the real shape of the chiral molecules and thus can prevent them from specifically coupling to the shear flow.

Nevertheless, there are certain hints in the literature that small molecular structures are able to couple to a shear flow (see ^{194,240} and references therein). For example, Kondepudi and coworkers created optically active crystals out of (non-chiral) sodium chlorate molecules with high purity. Nucleation sites with broken symmetry were induced by a stirring apparatus creating a shear flow in the solution. Its direction of rotation determines the handedness of the crystals²⁴¹. Ribò et al. used self-aggregating achiral chromophores in a stirring setup and detected a strong specific rise of signals in their circular dichroism spectra upon stirring in a certain direction²⁴².

Although the setting in these experiments is slightly different, because achiral monomers were crystallized to form chiral crystals, they still demonstrate that the shear flow has an

impact on how asymmetric nucleation seeds under the influence of diffusion and hydrate hulls are formed. Thus, it seems plausible, that small chiral molecules might couple to shear flows as well.

4.3.5 SUMMARY

The present idea for the separation of chiral microobjects within symmetry broken environments in microfluidic channels was inspired by Curie's Law. It refers to the asymmetric outcome of an experiment that has to be caused by asymmetric elements in the experimental device. The aim of the present project was an implementation of such elements in a microchannel by a slightly rotated non-chiral lattice of structured posts and by a triangular structure of one sidewall resulting in a shifted flow pattern. It could be successfully demonstrated that in those environments with broken symmetries, chiral microparticles are deflected axially in different directions.

Using homemade model enantiomers, both approaches performed excellent under the present experimental conditions. While the particles flowing through the device with the structured sidewall required roughly 1800 μm to be fully separated, the channel featuring the microlattice shows a roughly 10 fold better performance density. Not a single particle was falsely classified in both experiments.

5 SUMMARY AND OUTLOOK

Microfluidic devices are a very versatile cost- and sample efficient alternative to common laboratory techniques with currently lots of interesting and fruitful research and application perspectives. In this thesis three different projects with the goal to implement new advanced separation techniques on the microfluidic scale for single (bio-)molecules and particles such as micro beads or cells are presented in detail.

Advanced particle separation with tunable selectivity

In the first project, a microfluidic ratchet device has been constructed, that is able to separate N different particle species by using an elaborate scheme of dynamically changeable voltage protocols which triggers both trapping of particles and their transportation. Unlike standard biotechnological separation equipment like e.g. gel electrophoresis, the separation criterion is not statically implemented in the system but may freely be changed instantly at any time. Additionally, the effective direction of motion may be independently selected for every considered particle species.

The generic separation principle has been experimentally verified using $N = 3$ species of polystyrene microparticles with different q^*/α_p values where q^* is the effective charge and α_p the polarizability of a particle. Upon applying appropriate voltage schemes, it was possible to transport any arbitrary subsection of the mixture into negative x -direction while the remaining species moved with positive velocity into x -direction. Seizing the provided generic separation principle, simulations demonstrated that it is also working with higher N (here $N = 5$) in different modes of separation.

Electrophoresis and dielectrophoresis are two very common techniques in (bio)-technological applications and are able to address a wide range of possible analyte classes, e.g. nanoparticles, DNAs, proteins, cells, carbon nanotubes, and many more. Consequently, those substance classes should be analyzable with the present device as well, although slight adaptations (e.g. to generate higher electric field gradients and thus stronger dielectrophoretic traps) might be required. Since the present device relies on different q^*/α_p values for separation, even objects with identical size, but different material parameters are separable. This is especially interesting when e.g. DNAs of the same length but in different conformations need to be separated which is possible with means of comparable dielectrophoretic traps²⁴³.

So far, the separation takes place only in one dimension parallel to the x-axis. The application of a second pair of electrodes parallel to the y-direction will open up a further useable dimension allowing for more complex separation tasks. Additionally, the structuring of the channel with different types of posts along the y-direction might further boost possible multidimensional analysis, analogous to e.g. a two dimensional gel electrophoresis of proteins.

Of course, with more complex separation tasks the voltage pulses to apply will be even more complex as well and very hard to predict for the (perhaps inexperienced) experimenter. With a functional particle tracking software²⁴⁴ and an appropriate training algorithm the computer controlling the voltage pulses should be able to choose the best working voltage protocol on its own. Such a training algorithm would consist of at least a sequence where the electrophoretic mobility of each particle class is quantified and one where the corresponding polarizabilities are analyzed (e.g. with the technique discussed in section 4.2) because q^*/α_p is the relevant quantity.

Automated quantification of single molecule polarizability

Dielectrophoresis is a very common physical principle used in microfluidic systems to sort, immobilize, or manipulate a polarizable sample without any labeling. The overall performance of the final device is usually dependent on the actual polarizability of the present analyte under consideration. However, the actual value usually remains unquantified and correct parameters for dielectrophoresis are thus obtained via trial and error methods in the experiment. The aim of the second project was the implementation of an automated and easily useable microfluidic device to quantify polarizability values on the single molecule scale. Therefore, an analysis channel structured with rectangular posts is employed to generate dielectrophoretic traps where the electrophoretically driven analyte molecules (here DNA) are trapped for a certain time, before they are able to escape due to thermal energy. The polarizability can be calculated using the mean trapping times which are extracted automatically from fluorescence microscopy data by a home written script whose function is proofed theoretically.

As a proof of principle, the well-known relation $\alpha_p \propto 1/\sqrt{I}$ between the ionic strength I of the buffer and the molecular polarizability α_p of 12 kbp and 48.5 kbp double stranded DNA could be reproduced with this technique and a comparison between the automated method and a manual evaluation was provided. However, this technique requires spatial

localization of the analyte molecule that is usually accomplished with fluorescent staining (here with YoYo-1). Thus, the impact of the dye concentration on the molecular polarizability is investigated demonstrating that there is a weak but notable non-monotonic dependence.

Such an automated evaluation method is a useful tool not only for the quantification of single object polarizabilities in basic research. In a productive laboratory environment, micro devices with a broad range of possible analysis targets which are thus cost efficient and easy to use are demanded. However, a microfluidic device based on dielectrophoresis somehow automatically needs to adapt to the present sample which requires the automated analysis of its polarization behavior – a task that could be accomplished with the presented method.

Continuous selector free separation of chiral objects

Chiral organic molecules have mostly different pharmacological activities underlining the need for preparational and analytical techniques. Traditionally, for their purification, chiral selectors are used that specifically bind or derivatize only one enantiomeric form in a chromatography setup. This approach, however, requires the identification of new selectors for every new analyte and is working in batch-mode only. The third project thus deals with two different microfluidic devices with inherently broken symmetry to separate chiral microobjects without selectors.

The present concept to separate chiral microobjects by means of symmetry broken environments in microfluidic channels was inspired by Curie's Law. According to this principle the asymmetric outcome of an experiment has to be caused by asymmetric elements in the experimental device.

These elements are introduced by

1. chiral microparticles in combination with a *non-chiral* lattice of structured posts, slightly rotated against the x axis by an angle α (see Figure 40).
2. a triangular structuring of one sidewall of a straight microchannel which results in a shifted and thus asymmetric flow pattern (see Figure 41).

Because of these broken symmetries, chiral microparticles are deflected laterally within the fluid stream.

Both continuously working approaches performed excellent under the present experimental test conditions with homemade model enantiomers. Not a single particle was falsely classified in both devices. At optimal working conditions ($\alpha = 15^\circ$, see Table 11), the channel featuring the microlattice required approximately 200 μm in x direction for clearly splitting the particle stream. In this case, an overall splitting angle of $\Delta\vartheta_{15} = 22.8^\circ \pm 3.5^\circ$ under which the two particles species departed from each other has been observed experimentally. It was furthermore demonstrated in the experiment as well as theoretically, that the actual system geometry significantly influences the separation performance. Besides the dimensions of particles and posts, the tilting angle α plays an important role as e.g. demonstrated in a second experiment with $\alpha = 12^\circ$. In this case, the separation performance was significantly lower ($\Delta\vartheta_{12} = 5.76^\circ \pm 6.05^\circ$) and the behavior of L and Γ particles swapped. In all cases, the theoretically obtained results predicted experimental splitting angles quite well. All simulation results were located in the 1σ regime around the experimental counterparts with the exception of $\Delta\vartheta_{15}$ which lies in the 2σ regime.

The particles flowing through the device with the structured sidewall were observed to split up laterally in the flow as well and required roughly 1800 μm to be fully baseline separated. A total spatial resolution along the y axis of 3.75 was obtained. Additionally a significantly different migration speed of the two particle species in x direction was observed ($v_x^\Gamma = 0.44 \pm 0.01 \mu\text{m/s}$ and $v_x^L = 0.39 \pm 0.006 \mu\text{m/s}$).

Further development stages of the current system could be envisioned. First of all, for reasons of simplification the so far presented systems are quasi two dimensional because the generic principle behind the presented projects is independent of the dimensionality. However, for a real application with three dimensional samples, the symmetry in z direction has to be broken as well. This can e.g. be accomplished with a combination of asymmetric hydrodynamic flows (like in the 2D experiments) and a surface modification (e.g. with F108) on either the ceiling or the floor of the considered microchannel. An electric field applied to such a channel will induce an electroosmotic flow, partly suppressed on the modified surface but unhindered near the uncoated surface. When this electroosmotic flow is directed against the hydrodynamic flow, a flow field with completely broken symmetry, displayed in Figure 63 can be experimentally realized.

Regardless of the full three dimensional realization, the current scale of the two model systems is too large for actual molecular considerations. Hence, further downscaling of the

discussed generic principles is required. However, with current state of the art lithography e.g. with our newly obtained helium ion microscope practical feature sizes down to some nanometers are possible²⁴⁵ which is still too large for actual pharmaceutical compounds even if a channel with structured sidewalls is used. One could think of an asymmetrically self-organizing system of e.g. nanocrystals^{246–248} which is, however, in a very early stage of research²⁴⁹.

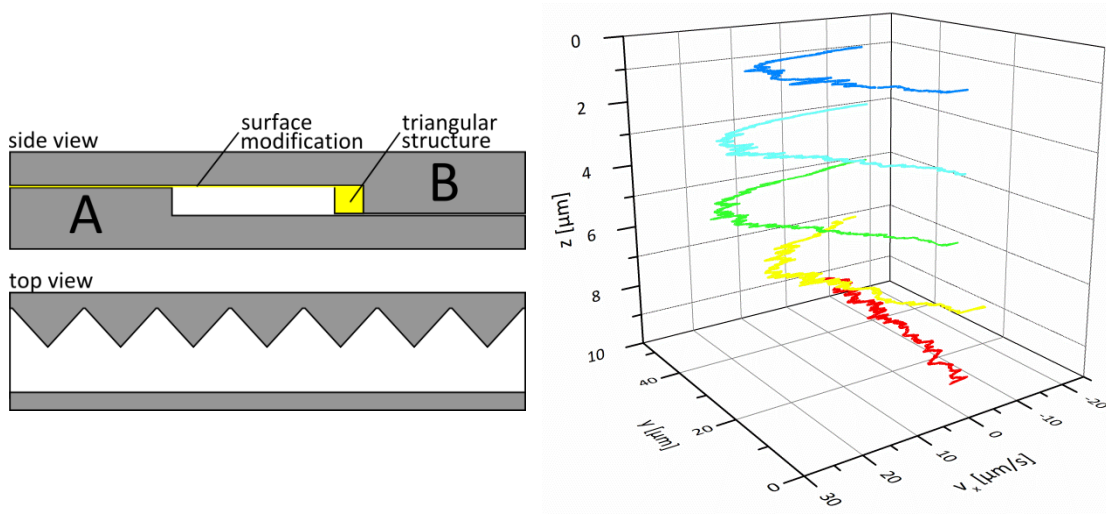


Figure 63: Left: Schematic overview of a chip prototype that creates a flow profile with broken symmetry in all three dimensions. Two separate prestructured pieces of PDMS A and B are precisely aligned and bonded with a Fineplacer® Lambda System after an oxygen plasma treatment. Only piece B which carries the triangular structure on its sidewall has been surface modified with F108 to suppress electroosmotic flow on its surface. Piece A is unmodified. Right: The resulting experimental and fully three dimensional flow profile for the separation of three dimensional chiral microparticles. Here electroosmotic flow and hydrodynamic flow act against each other. While the hydrodynamic flow is dominant near the modified ceiling and the triangular structure, the situation near the unmodified bottom and the flat wall is contrary. Here, electroosmotic effects annihilate hydrodynamic effects and even move liquid to the opposite direction (v_x changes sign over the height of the channel). With such a device, chiral particles could even be separated by letting them flow against each other into opposite directions. Plot redrawn with data from²⁵⁰.

6 REFERENCES

1. F. Lottspeich & J. W. Engels: *Bioanalytik*, 3rd ed. (Spektrum Akademischer Verlag, Berlin, 2012).
2. T. Ideker, T. Galitski & L. Hood: *A New Approach to Decoding Life: Systems Biology*, Annual Review of Genomics and Human Genetics 2 (2001), 343–372.
3. H. Kitano: *Systems biology: a brief overview*, Science 295 (2002), 1662–1664.
4. J. van der Greef, P. Stroobant & R. van der Heijden: *The role of analytical sciences in medical systems biology*, Current opinion in chemical biology 8 (2004), 559–565.
5. H.-Y. Chuang, M. Hofree & T. Ideker: *A decade of systems biology*, Annual review of cell and developmental biology 26 (2010), 721–744.
6. J. R. Heath, M. E. Phelps & L. Hood: *NanoSystems biology*, Molecular imaging and biology 5 (2003), 312–325.
7. L. Hood, J. R. Heath, M. E. Phelps & B. Lin: *Systems Biology and New Technologies Enable Predictive and Preventative Medicine*, Science 306 (2004), 640–643.
8. A. D. Weston & L. Hood: *Systems biology, proteomics, and the future of health care: toward predictive, preventative, and personalized medicine*, Journal of Proteome Research 3 (2004), 179–196.
9. L. Hood & S. H. Friend: *Predictive, personalized, preventive, participatory (P4) cancer medicine*, Nature Reviews: Clinical Oncology 8 (2011), 184–187.
10. G. Gübitz & M. G. Schmid: *Recent progress in chiral separation principles in capillary electrophoresis*, Electrophoresis 21 (2000), 4112–4135.
11. A. Amini: *Recent developments in chiral capillary electrophoresis and applications of this technique to pharmaceutical and biomedical analysis*, Electrophoresis 22 (2001), 3107–3130.
12. C. D. Chin, V. Linder & S. K. Sia: *Lab-on-a-chip devices for global health: past studies and future opportunities*, Lab on a Chip 7 (2007), 41–57.
13. G. M. Whitesides: *The origins and the future of microfluidics*, Nature 442 (2006), 368–373.
14. P. Yager, T. Edwards, E. Fu, K. Helton, K. Nelson, M. R. Tam & B. H. Weigl: *Microfluidic diagnostic technologies for global public health*, Nature 442 (2006), 412–418.
15. D. R. Reyes, D. Iossifidis, P.-A. Auroux & A. Manz: *Micro Total Analysis Systems. 1. Introduction, Theory, and Technology*, Analytical Chemistry 74 (2002), 2623–2636.
16. P.-A. Auroux, D. Iossifidis, D. R. Reyes & A. Manz: *Micro Total Analysis Systems. 2. Analytical Standard Operations and Applications*, Analytical Chemistry 74 (2002), 2637–2652.
17. T. Vilkner, D. Janasek & A. Manz: *Micro Total Analysis Systems. Recent Developments*, Analytical Chemistry 76 (2004), 3373–3386.
18. P. S. Dittrich, K. Tachikawa & A. Manz: *Micro Total Analysis Systems. Latest Advancements and Trends*, Analytical Chemistry 78 (2006), 3887–3908.

19. J. West, M. Becker, S. Tombrink & A. Manz: *Micro Total Analysis Systems: Latest Achievements*, Analytical Chemistry 80 (2008), 4403–4419.
20. A. Arora, G. Simone, G. B. Salieb-Beugelaar, J. T. Kim & A. Manz: *Latest Developments in Micro Total Analysis Systems*, Analytical Chemistry 82 (2010), 4830–4847.
21. H. A. Pohl: *Dielectrophoresis - The behavior of neutral matter in nonuniform electric fields*, 1st ed. (Cambridge University Press, Cambridge, 1978).
22. E. A. Strychalski, S. M. Stavis, M. Gaitan & L. E. Locascio: *Nanoslinky: DNA entropophoresis down a nanofluidic staircase*, Proceedings of the 14th International Conference on Miniaturized Systems for Chemistry and Life Sciences 2010, Groningen, The Netherlands (2010), 2071–2073.
23. J. Han & H. G. Craighead: *Separation of long DNA molecules in a microfabricated entropic trap array*, Science 288 (2000), 1026–1029.
24. P. Reimann: *Brownian motors: noisy transport far from equilibrium*, Physics Reports 361 (2002), 57–265.
25. R. Eichhorn, P. Reimann, B. Cleuren & C. van den Broeck: *Moving backward noisily*, Chaos 15 (2005), 26113.
26. P. Curie: *Sur la symétrie des phénomènes physiques: symétrie d'un champ électrique et d'un champ magnétique*, Journal de Physique 3 (1894), 393–415.
27. B. Lojek: *History of semiconductor engineering*, 1st ed. (Springer, New York, 2006).
28. W. Shockley (Bell Telephone Laboratories Inc.): *Semiconductor amplifier*, Patent No.: US2502488, patented April 4th 1950.
29. K. E. Petersen: *Silicon as a mechanical material*, Proceedings of the IEEE 70 (1982), 420–457.
30. W. P. Eaton & J. H. Smith: *Micromachined pressure sensors: review and recent developments*, Smart Materials and Structures 6 (1997), 530–539.
31. E. Bassous, H. H. Taub & L. Kuhn: *Ink jet printing nozzle arrays etched in silicon*, Applied Physics Letters 31 (1977), 135.
32. K. Liu, W. Zhang, W. Chen, K. Li, F. Dai, F. Cui, X. Wu, G. Ma & Q. Xiao: *The development of micro-gyroscope technology*, Journal of Micromechanics and Microengineering 19 (2009), 113001.
33. M. Vogel: *Wischen, antippen, aufziehen*, Physik Journal 10, No. 4 (2011), 42–43.
34. A. Manz, N. Graber & H. M. Widmer: *Miniaturized total chemical analysis systems: a novel concept for chemical sensing*, Sensors and Actuators B 1 (1990), 244–248.
35. N.-T. Nguyen & S. T. Wereley: *Fundamentals and applications of microfluidics*, 2nd ed. (Artech House, Boston (Massachusetts), 2006).
36. T. M. Squires & S. R. Quake: *Microfluidics: Fluid physics at the nanoliter scale*, Reviews of Modern Physics 77 (2005), 977–1026.
37. P. Tabeling: *Introduction to microfluidics*, 1st ed. (Oxford University Press, Oxford, 2005).
38. H. Bruus: *Theoretical microfluidics*, 1st ed. (Oxford University Press, Oxford, 2008).
39. R. F. Probstein: *Physicochemical hydrodynamics*, 2nd ed. (Wiley-Interscience, Hoboken, New Jersey, 2003).

40. L. D. Landau & E. M. Lifschitz: *Hydrodynamik*, 5th ed. (Harri Deutsch, Frankfurt am Main, 2007).
41. J. Koplik & J. R. Banavar: *Continuum Deductions from Molecular Hydrodynamics*, Annual Review of Fluid Mechanics 27 (1995), 257–292.
42. H. A. Stone, A. D. Stroock & A. Ajdari: *Engineering flows in small devices*, Annual Review of Fluid Mechanics 36 (2004), 381–411.
43. E. Lauga, M. Brenner & H. Stone: *Microfluidics: The No-Slip Boundary Condition*, in: *Springer Handbook of Experimental Fluid Mechanics*, edited by C. Tropea, A. L. Yarin & J. F. Foss (Springer-Verlag Berlin Heidelberg, Berlin, 2007), pp. 1219–1240.
44. R. Pit, H. Hervet & L. Léger: *Direct Experimental Evidence of Slip in Hexadecane: Solid Interfaces*, Physical Review Letters 85 (2000), 980–983.
45. P. Joseph & P. Tabeling: *Direct measurement of the apparent slip length*, Physical Review E 71 (2005), 35303.
46. C. I. Bouzigues, P. Tabeling & L. Bocquet: *Nanofluidics in the Debye Layer at Hydrophilic and Hydrophobic Surfaces*, Physical Review Letters 101 (2008), 114503.
47. H. Brenner: *Beyond the no-slip boundary condition*, Physical Review E 84 (2011), 46309.
48. W. Hellmich, J. Regtmeier, T. T. Duong, R. Ros, D. Anselmetti & A. Ros: *Poly(oxyethylene) Based Surface Coatings for Poly(dimethylsiloxane) Microchannels*, Langmuir 21 (2005), 7551–7557.
49. U. Aebi & T. D. Pollard: *A Glow Discharge Unit to Render Electron Microscope Grids and Other Surfaces Hydrophilic*, Journal of Electron Microscopy Technique 7 (1987), 29–33.
50. H. Stöcker (ed.): *Taschenbuch der Physik*, (Harri Deutsch, Frankfurt am Main, 2005).
51. E. M. Purcell: *Life at low Reynolds number*, American Journal of Physics 45 (1977), 3–11.
52. C.-Y. Lee, C.-L. Chang, Y.-N. Wang & L.-M. Fu: *Microfluidic Mixing: A Review*, International Journal of Molecular Sciences 12 (2011), 3263–3287.
53. C. J. Campbell & B. A. Grzybowski: *Microfluidic mixers: from microfabricated to self-assembling devices*, Philosophical Transactions of the Royal Society A 362 (2004), 1069–1086.
54. J. B. Hubbard & J. F. Douglas: *Hydrodynamic friction of arbitrarily shaped Brownian particles*, Physical Review E 47 (1993), R2983.
55. C. Gerthsen & D. Meschede: *Gerthsen Physik*, 22nd ed. (Springer, Berlin, 2004).
56. F. F. Reuss: *Charge-Induced Flow*, Proceedings of the Imperial Society of Naturalists of Moscow 3 (1809), 327–344.
57. E. B. Cummings, S. K. Griffiths, R. H. Nilson & P. H. Paul: *Conditions for Similitude between the Fluid Velocity and Electric Field in Electroosmotic Flow*, Analytical Chemistry 72 (2000), 2526–2532.
58. H. A. Pohl: *The Motion and Precipitation of Suspensoids in Divergent Electric Fields*, Journal of Applied Physics 22 (1951), 869–871.
59. T. B. Jones: *Electromechanics of particles*, 1st ed. (Cambridge University Press, Cambridge, 1995).

60. J. Regtmeier, R. Eichhorn, M. Viefhues, L. Bogunovic & D. Anselmetti: *Electrodeless dielectrophoresis for bioanalysis: Theory, devices and applications*, *Electrophoresis* 32 (2011), 2253–2273.
61. S. Koneshan, J. C. Rasaiah, R. M. Lynden-Bell & S. H. Lee: *Solvent Structure, Dynamics, and Ion Mobility in Aqueous Solutions at 25 °C*, *Journal of Physical Chemistry B* 102 (1998), 4193–4204.
62. T. B. Jones: *Basic theory of dielectrophoresis and electrorotation*, *IEEE Engineering in Medicine and Biology Magazine* 22 (2003), 33–42.
63. R. Pethig: *Dielectrophoresis: Status of the theory, technology, and applications*, *Biomicrofluidics* 4 (2010), 22811.
64. J. S. Park & D. Saintillan: *Dipolophoresis in large-scale suspensions of ideally polarizable spheres*, *Journal of Fluid Mechanics* 662 (2010), 66–90.
65. C.-F. Chou, J. O. Tegenfeldt, O. Bakajin, S. S. Chan, E. C. Cox, N. Darnton, T. Duke & R. H. Austin: *Electrodeless Dielectrophoresis of Single- and Double-Stranded DNA*, *Biophysical journal* 83 (2002), 2170–2179.
66. H. Zhou, M. A. Preston, R. D. Tilton & L. R. White: *Calculation of the electric polarizability of a charged spherical dielectric particle by the theory of colloidal electrokinetics*, *Journal of Colloid and Interface Science* 285 (2005), 845–856.
67. T. S. Simonova, V. N. Shilov & O. A. Shramko: *Low-Frequency Dielectrophoresis and the Polarization Interaction of Uncharged Spherical Particles with an Induced Debye Atmosphere of Arbitrary Thickness*, *Colloid Journal* 63 (2001), 108–115.
68. L. Bogunovic: *Einflüsse der Ionenkonzentration und von Fluorophoren auf die Polarisierbarkeit von linearer DNA in Mikrofluidiksystemen*, Bachelor-Thesis, Bielefeld University, 2007.
69. V. N. Shilov: *Dielectrophoresis of nanosized particle*, *Colloid Journal* 70 (2008), 515–528.
70. S. Basuray, H.-H. Wei & H.-C. Chang: *Dynamic double layer effects on ac-induced dipoles of dielectric nanocolloids*, *Biomicrofluidics* 4 (2010), 22801.
71. T. Jones: *Dielectrophoretic force calculation*, *Journal of Electrostatics* 6 (1979), 69–82.
72. R. Brown: *A brief account of microscopical observations made in the months of June, July and August, 1827, on the particles contained in the pollen of plants; and on the general existence of active molecules in organic and inorganic bodies*, *Edinburgh New Philosophical Journal* 19 (1828), 358–371.
73. D. Layton: *The original observations of Brownian motion*, *Journal of Chemical Education* 42 (1965), 367–368.
74. A. Einstein: *Über die von der molekularkinetischen Theorie der Wärme geforderte Bewegung von in ruhenden Flüssigkeiten suspendierten Teilchen*, *Annalen der Physik* 17 (1905), 549–560.
75. M. Smoluchowski: *Zur kinetischen Theorie der Brownschen Molekularbewegung und der Suspensionen*, *Annalen der Physik* 21 (1906), 756–780.
76. O. Geschke, H. Klank & P. Telleman: *Microsystem engineering of lab-on-a-chip devices*, 1st ed. (WILEY-VCH, Weinheim, 2005).

77. N. G. van Kampen: *Stochastic processes in physics and chemistry*, 3rd ed. (North-Holland, Amsterdam, 2007).
78. H. A. Kramers: *Brownian motion in a field of force and the diffusion model of chemical reactions*, *Physica* 7 (1940), 284–304.
79. P. J. Park & W. Sung: *Dynamics of a polymer surmounting a potential barrier: The Kramers problem for polymers*, *Journal of Chemical Physics* 111 (1999), 5259–5266.
80. P. Hänggi, P. Talkner & M. Borkovec: *Reaction-rate theory: fifty years after Kramers*, *Reviews of Modern Physics* 62 (1990), 251–341.
81. P. Reimann, G. J. Schmid & P. Hänggi: *Universal equivalence of mean first-passage time and Kramers rate*, *Physical Review E* 60 (1999), R1–R4.
82. J. Regtmeier, T. T. Duong, R. Eichhorn, D. Anselmetti & A. Ros: *Dielectrophoretic Manipulation of DNA: Separation and Polarizability*, *Analytical Chemistry* 79 (2007), 3925–3932.
83. P. Hänggi & F. Marchesoni: *Artificial Brownian motors: Controlling transport on the nanoscale*, *Reviews of Modern Physics* 81 (2009), 387–442.
84. F. Jülicher, A. Ajdari & J. Prost: *Modeling molecular motors*, *Reviews of Modern Physics* 69 (1997), 1269–1282.
85. R. D. Astumian: *Thermodynamics and Kinetics of a Brownian Motor*, *Science* 276 (1997), 917–922.
86. J. Rousselet, L. Salome, A. Ajdari & J. Prost: *Directional motion of brownian particles induced by a periodic asymmetric potential*, *Nature* 370 (1994), 446–447.
87. L. Faucheux, L. Bourdieu, P. Kaplan & A. Libchaber: *Optical Thermal Ratchet*, *Physical Review Letters* 74 (1995), 1504–1507.
88. H. Linke, T. E. Humphrey, A. Löfgren, A. O. Sushkov, R. Newbury, R. P. Taylor & P. Omling: *Experimental Tunneling Ratchets*, *Science* 286 (1999), 2314–2317.
89. J. S. Bader, R. W. Hammond, S. A. Henck, M. W. Deem, G. A. McDermott, J. M. Bustillo, J. W. Simpson, G. T. Mulhern & J. M. Rothberg: *DNA transport by a micromachined Brownian ratchet device*, *Proceedings of the National Academy of Sciences of the United States of America* 96 (1999), 13165–13169.
90. J. E. Villegas, S. Savel'ev, F. Nori, E. M. Gonzalez, J. V. Anguita, R. García & J. L. Vicent: *A Superconducting Reversible Rectifier That Controls the Motion of Magnetic Flux Quanta*, *Science* 302 (2003), 1188–1191.
91. S. Ghosh, A. K. Sood & N. Kumar: *Carbon Nanotube Flow Sensors*, *Science* 299 (2003), 1042–1044.
92. S. Matthias & F. Müller: *Asymmetric pores in a silicon membrane acting as massively parallel brownian ratchets*, *Nature* 424 (2003), 53–57.
93. J. V. Hernandez, E. R. Kay & D. A. Leigh: *A Reversible Synthetic Rotary Molecular Motor*, *Science* 306 (2004), 1532–1537.
94. S.-H. Lee, K. Ladavac, M. Polin & D. G. Grier: *Observation of Flux Reversal in a Symmetric Optical Thermal Ratchet*, *Physical Review Letters* 94 (2005), 110601.
95. D. Cole, S. Bending, S. Savel'ev, A. Grigorenko, T. Tamegai & F. Nori: *Ratchet without spatial asymmetry for controlling the motion of magnetic flux quanta using time-asymmetric drives*, *Nature Materials* 5 (2006), 305–311.

96. A. Pérez-Junquera, V. Marconi, A. Kolton, L. Álvarez-Prado, Y. Souche, A. Alija, M. Vélez, J. V. Anguita, J. Alameda, J. Martín & J. Parrondo: *Crossed-Ratchet Effects for Magnetic Domain Wall Motion*, *Physical Review Letters* 100 (2008), 37203.
97. G. Lambert, D. Liao & R. H. Austin: *Collective Escape of Chemotactic Swimmers through Microscopic Ratchets*, *Physical Review Letters* 104 (2010).
98. R. Eichhorn, P. Reimann & P. Hänggi: *Brownian Motion Exhibiting Absolute Negative Mobility*, *Physical Review Letters* 88 (2002), 190601.
99. B. Cleuren & C. van den Broeck: *Random walks with absolute negative mobility*, *Physical Review E* 65 (2002), 30101.
100. R. Eichhorn, P. Reimann & P. Hänggi: *Paradoxical motion of a single Brownian particle: Absolute negative mobility*, *Physical Review E* 66 (2002), 66132.
101. R. Eichhorn, P. Reimann & P. Hänggi: *Absolute negative mobility and current reversals of a meandering Brownian particle*, *Physica A* 325 (2003), 101–109.
102. B. Cleuren & C. van den Broeck: *Brownian motion with absolute negative mobility*, *Physical Review E* 67 (2003), 55101.
103. B. Jiménez de Cisneros, P. Reimann & J. M. R. Parrondo: *Non-cooperative Brownian donkeys: A solvable 1D model*, *Europhysics Letters* 64 (2003), 599–605.
104. R. Eichhorn & P. Reimann: *Paradoxical directed diffusion due to temperature anisotropies*, *Europhysics Letters* 69 (2005), 517.
105. I. Derényi & R. Dean Astumian: *ac separation of particles by biased Brownian motion in a two-dimensional sieve*, *Physical Review E* 58 (1998), 7781–7784.
106. C. Keller, F. Marquardt & C. Bruder: *Separation quality of a geometric ratchet*, *Physical Review E* 65 (2002), 41927.
107. C. Kettner, P. Reimann, P. Hänggi & F. Müller: *Drift ratchet*, *Physical Review E* 61 (2000), 312–323.
108. L. P. Faucheux & A. Libchaber: *Selection of Brownian particles*, *Journal of the Chemical Society, Faraday Transactions* 91 (1995), 3163–3166.
109. K. Louthback, J. Puchalla, R. H. Austin & J. C. Sturm: *Deterministic Microfluidic Ratchet*, *Physical Review Letters* 102 (2009), 45301.
110. K. Louthback, K. S. Chou, J. Newman, J. Puchalla, R. H. Austin & J. C. Sturm: *Improved performance of deterministic lateral displacement arrays with triangular posts*, *Microfluidics and Nanofluidics* 9 (2010), 1143–1149.
111. L. Gorre-Talini, S. Jeanjean & P. Silberzan: *Sorting of Brownian particles by the pulsed application of an asymmetric potential*, *Physical Review E* 56 (1997), 2025–2034.
112. L. Gorre-Talini, J. P. Spatz & P. Silberzan: *Dielectrophoretic ratchets*, *Chaos* 8 (1998), 650–656.
113. A. van Oudenaarden & S. G. Boxer: *Brownian Ratchets: Molecular Separations in Lipid Bilayers Supported on Patterned Arrays*, *Science* 285 (1999), 1046–1048.
114. C. Marquet, A. Buguin, L. Talini & P. Silberzan: *Rectified Motion of Colloids in Asymmetrically Structured Channels*, *Physical Review Letters* 88 (2002), 168301.

115. L. R. Huang, P. Silberzan, J. O. Tegenfeldt, E. C. Cox, J. C. Sturm, R. H. Austin & H. Craighead: *Role of Molecular Size in Ratchet Fractionation*, Physical Review Letters 89 (2002), 178301.
116. L. R. Huang, E. C. Cox, R. H. Austin & J. C. Sturm: *Continuous Particle Separation Through Deterministic Lateral Displacement*, Science 304 (2004), 987–990.
117. S. Choi & J.-K. Park: *Microfluidic system for dielectrophoretic separation based on a trapezoidal electrode array*, Lab on a Chip 5 (2005), 1161–1167.
118. P. Tierno, S. V. Reddy, M. G. Roper, T. H. Johansen & T. M. Fischer: *Transport and Separation of Biomolecular Cargo on Paramagnetic Colloidal Particles in a Magnetic Ratchet*, Journal of Physical Chemistry B 112 (2008), 3833–3837.
119. G. Mahmud, C. J. Campbell, K. J. M. Bishop, Y. A. Komarova, O. Chaga, S. Soh, S. Huda, K. Kandere-Grzybowska & B. A. Grzybowski: *Directing cell motions on micropatterned ratchets*, Nature Physics 5 (2009), 606–612.
120. A. Ros, R. Eichhorn, J. Regtmeier, T. T. Duong, P. Reimann & D. Anselmetti: *Brownian motion: absolute negative particle mobility*, Nature 436 (2005), 928.
121. H. J. Roth: *Chiralität*, Student und Praktikant 1 (2007), 6–11.
122. G. P. Moss: *Basic terminology of stereochemistry*, Pure and applied chemistry 68 (1996), 2193–2222.
123. Lord Kelvin: *The Baltimore lectures on molecular dynamics and the wave theory of light*, (C. J. Clay and sons, London, 1904).
124. S. Capozziello & A. Lattanzi: *Spiral galaxies as enantiomers: Chirality, an underlying feature in chemistry and astrophysics*, Chirality 18 (2006), 17–23.
125. A. Slosar, K. Land, S. Bamford, C. Lintott, D. Andreescu, P. Murray, R. Nichol, M. J. Raddick, K. Schawinski, A. Szalay, D. Thomas & J. Vandenberg: *Galaxy Zoo: Chiral correlation function of galaxy spins*, Monthly Notices of the Royal Astronomical Society 392 (2009), 1225–1232.
126. C. Hardyck & L. F. Petrinovich: *Left-handedness*, Psychological Bulletin 84 (1977), 385–404.
127. B. Casey: *Two rights make a wrong: human left-right malformations*, Human Molecular Genetics 7 (1998), 1565–1571.
128. M. Schilthuizen & A. Davison: *The convoluted evolution of snail chirality*, Naturwissenschaften 92 (2005), 504–515.
129. S. R. Buxton & S. M. Roberts: *Einführung in die organische Stereochemie*, (Vieweg, Braunschweig, 1999).
130. E. L. Eliel, S. H. Wilen & H. Hopf: *Organische Stereochemie*, 1st ed. (WILEY-VCH, Weinheim, 1998).
131. E. J. Ariëns: *Stereochemistry, a basis for sophisticated nonsense in pharmacokinetics and clinical pharmacology*, European Journal of Clinical Pharmacology 26 (1984), 663–668.
132. J. C. Leffingwell: *Chirality & Bioactivity I: Pharmacology*, Leffingwell Reports 3 (2003), 1–27.
133. H. J. Roth: *Dex-, Lev-, Ar-, Es-, Rac-, neue "reine" Arzneistoffe*, Deutsche Apotheker Zeitung 149 (2009), 3182–3186.

134. T. J. Maher & D. A. Johnson: *Review of chirality and its importance in pharmacology*, Drug Development Research 24 (1991), 149–156.
135. C. S. Wu, E. Ambler, R. W. Hayward, D. D. Hoppes & R. P. Hudson: *Experimental Test of Parity Conservation in Beta Decay*, Physical Review E 105 (1957), 1413–1415.
136. M. Goldhaber, L. Grodzins & A. Sunyar: *Helicity of Neutrinos*, Physical Review E 109 (1958), 1015–1017.
137. R. Cahn, C. Ingold & V. Prelog: *The specification of asymmetric configuration in organic chemistry*, Cellular and Molecular Life Sciences 12 (1956), 81–94.
138. R. S. Cahn & C. K. Ingold: *131. Specification of configuration about tetravalent asymmetric atoms*, Journal of the Chemical Society (1951), 612–622.
139. R. Dahm: *Discovering DNA: Friedrich Miescher and the early years of nucleic acid research*, Human Genetics 122 (2008), 565–581.
140. F. S. Collins, E. D. Green, A. E. Guttmacher & M. S. Guyer: *A vision for the future of genomics research*, Nature 422 (2003), 835–847.
141. L. Hartwell, L. Hood, M. L. Goldberg, A. E. Reynolds & L. M. Silver: *Genetics - From genes to genomes*, 4th ed. (McGraw-Hill, New York, 2011).
142. L. Hood, L. Rowen, D. J. Galas & J. D. Aitchison: *Systems biology at the Institute for Systems Biology*, Briefings in Functional Genomics and Proteomics 7 (2008), 239–248.
143. J. D. Watson & F. Crick: *Molecular structure of nucleic acids*, Nature 171 (1953), 737–738.
144. M. Mandelkern, J. G. Elias, D. Eden & D. M. Crothers: *The dimensions of DNA in solution*, Journal of Molecular Biology 152 (1981), 153–161.
145. R. Wing, H. Drew, T. Takano, C. Broka, S. Tanaka, K. Itakura & R. E. Dickerson: *Crystal structure analysis of a complete turn of B-DNA*, Nature 287 (1980), 755–758.
146. International Human Genome Sequencing Consortium: *Finishing the euchromatic sequence of the human genome*, Nature 431 (2004), 931–945.
147. C. R. Calladine, H. R. Drew, B. F. Luisi, A. A. Travers & J. Wissmann: *DNA*, 3rd ed. (Elsevier, Heidelberg, 2006).
148. J. M. Berg, L. Stryer & J. L. Tymoczko: *Biochemie*, 6th ed. (Spektrum, Heidelberg, 2011).
149. L. S. Lerman: *Structural considerations in the interaction of DNA and acridines*, Journal of Molecular Biology 3 (1961), 18–30.
150. H. Ihmels & D. Otto: *Intercalation of Organic Dye Molecules into Double-Stranded DNA -- General Principles and Recent Developments*, Topics in current chemistry 258 (2005), 161–204.
151. S. Gurrieri, K. Sam Wells, I. D. Johnson & C. Bustamante: *Direct Visualization of Individual DNA Molecules by Fluorescence Microscopy: Characterization of the Factors Affecting Signal/Background and Optimization of Imaging Conditions Using YOYO*, Analytical Biochemistry 249 (1997), 44–53.
152. A. N. Glazer & H. S. Rye: *Stable dye–DNA intercalation complexes as reagents for high-sensitivity fluorescence detection*, Nature 359 (1992), 859–861.

153. A. Larsson, C. Carlsson, M. Jonsson & B. Albinsson: *Characterization of the Binding of the Fluorescent Dyes YO and YOYO to DNA by Polarized Light Spectroscopy*, *Journal of the American Chemical Society* 116 (1994), 8459–8465.
154. H. S. Rye, S. Yue, D. E. Wemmer, M. A. Quesada, R. P. Haugland, R. A. Mathies & A. N. Glazer: *Stable fluorescent complexes of double-stranded DNA with bis-intercalating asymmetric cyanine dyes: properties and applications*, *Nucleic Acids Research* 20 (1992), 2803–2812.
155. W. Hellmich: *Einzelzellanalytik in Mikrofluidik-Systemen*, Dissertation, Bielefeld University, 2006.
156. T. T. Duong: *Neue Migrations- und Separationsmechanismen in strukturierten Mikrofluidik-Systemen*, Dissertation, Bielefeld University, 2006.
157. Y. Xia & G. M. Whitesides: *Soft Lithography*, *Annual Review of Materials Science* 28 (1998), 153–184.
158. J. A. Rogers & R. G. Nuzzo: *Recent progress in soft lithography*, *Materials Today* 8 (2005), 50–56.
159. A. Edelstein, N. Amodaj, K. Hoover, R. Vale & N. Stuurman: *Computer Control of Microscopes Using MicroManager*, *Current Protocols in Molecular Biology* 92 (2010), 14.20.1-14.20-17.
160. Zeiss: *Axiovert 200 - Der neue Maßstab in der inversen Mikroskopie* (downloaded Dez 17th 2013). Available at [http://www.zeiss.de/C1256CFB00332E16/0/3330FF6410BF12F2C1256CFC00269004/\\$file/40-084_d.pdf](http://www.zeiss.de/C1256CFB00332E16/0/3330FF6410BF12F2C1256CFC00269004/$file/40-084_d.pdf).
161. B. Carrasco & J. de La García Torre: *Hydrodynamic Properties of Rigid Particles: Comparison of Different Modeling and Computational Procedures*, *Biophysical Journal* 76 (1999), 3044–3057.
162. M. Pycraft Hughes: *AC electrokinetics: applications for nanotechnology*, *Nanotechnology* 11 (2000), 124–132.
163. C. Zhang, K. Khoshmanesh, A. Mitchell & K. Kalantar-zadeh: *Dielectrophoresis for manipulation of micro/nano particles in microfluidic systems*, *Analytical and Bioanalytical Chemistry* 396 (2010), 401–420.
164. A. Kuzyk: *Dielectrophoresis at the nanoscale*, *Electrophoresis* 32 (2011), 2307–2313.
165. J. F. Robyt & B. J. White: *Biochemical techniques*, 1st ed. (Waveland Press, Prospect Heights, Illinois, 1990).
166. R. V. Goering: *Pulsed field gel electrophoresis: A review of application and interpretation in the molecular epidemiology of infectious disease*, *Infection, Genetics and Evolution* 10 (2010), 866–875.
167. Y. Lu, T. Takeshita & K. Morimoto: *Single-cell gel electrophoresis (SCG)-A review and discussion*, *Environmental Health and Preventive Medicine* 2 (1997), 53–58.
168. T. A. J. Duke & R. H. Austin: *Microfabricated Sieve for the Continuous Sorting of Macromolecules*, *Physical Review Letters* 80 (1998), 1552–1555.
169. D. Ertaş: *Lateral Separation of Macromolecules and Polyelectrolytes in Microlithographic Arrays*, *Physical Review Letters* 80 (1998), 1548–1551.

170. J. Regtmeier, R. Eichhorn, T. T. Duong, P. Reimann, D. Anselmetti & A. Ros: *Pulsed-field separation of particles in a microfluidic device*, European Physical Journal E 22 (2007), 335-340.
171. J. Liu, Y. F. Yap & N.-T. Nguyen: *Motion of a droplet through microfluidic ratchets*, Physical Review E 80 (2009), 46319.
172. P. Tierno, P. Reimann, T. H. Johansen & F. Sagués: *Giant Transversal Particle Diffusion in a Longitudinal Magnetic Ratchet*, Physical Review Letters 105 (2010), 230602.
173. Q. Guo, S. M. McFaul & H. Ma: *Deterministic microfluidic ratchet based on the deformation of individual cells*, Physical Review E 83 (2011), 51910.
174. S. M. McFaul, B. K. Lin & H. Ma: *Cell separation based on size and deformability using microfluidic funnel ratchets*, Lab on a Chip 12 (2012), 2369–2376.
175. G. Costantini & F. Marchesoni: *Threshold diffusion in a tilted washboard potential*, Europhysics Letters 48 (1999), 491–497.
176. P. Reimann, C. van den Broeck, H. Linke, P. Hänggi, J. Rubi & A. Pérez-Madrid: *Giant Acceleration of Free Diffusion by Use of Tilted Periodic Potentials*, Physical Review Letters 87 (2001), 10602.
177. J. Regtmeier: *Non-equilibrium migration mechanisms for microfluidic bioanalysis*, Dissertation, Bielefeld University, 2007.
178. P. Reimann & R. Eichhorn: *Weak Disorder Strongly Improves the Selective Enhancement of Diffusion in a Tilted Periodic Potential*, Physical Review Letters 101 (2008), 180601.
179. L. Bogunovic, R. Eichhorn, J. Regtmeier, D. Anselmetti & P. Reimann: *Particle sorting by a structured microfluidic ratchet device with tunable selectivity: theory and experiment*, Soft Matter 8 (2012), 3900–3907.
180. D. C. Rau & V. A. Bloomfield: *Transient electric birefringence of T7 viral DNA*, Biopolymers 18 (1979), 2783–2805.
181. N. C. Stellwagen: *Electric birefringence of restriction enzyme fragments of DNA: optical factor and electric polarizability as a function of molecular weight*, Biopolymers 20 (1981), 399–434.
182. M. Hanss & J. C. Bernengo: *Dielectric relaxation and orientation of DNA molecules*, Biopolymers 12 (1973), 2151–2159.
183. D. J. Bakewell, I. Ermolina, H. Morgan, J. Milner & Y. Feldman: *Dielectric relaxation measurements of 12 kbp plasmid DNA*, Biochimica et biophysica acta 1493 (2000), 151–158.
184. R. Eichhorn, personal communication.
185. S. Tuukkanen, A. Kuzyk, J. J. Toppari, H. Häkkinen, V. P. Hytönen, E. Niskanen, M. Rinkiö & P. Törmä: *Trapping of 27 bp–8 kbp DNA and immobilization of thiol-modified DNA using dielectrophoresis*, Nanotechnology 18 (2007), 295204.
186. D. C. Rau & E. Charney: *Electric dichroism of DNA: Influence of the ionic environment on the electric polarizability*, Biophysical Chemistry 17 (1983), 35–50.
187. D. Porschke: *Macrodipoles Unusual electric properties of biological macromolecules*, Biophysical Chemistry 66 (1997), 241–257.

188. H. Washizu & K. Kikuchi: *Electric polarizability of DNA in aqueous salt solution*, Journal of Physical Chemistry B 110 (2006), 2855–2861.
189. B. Saif, R. K. Mohr, C. J. Montrose & T. A. Litovitz: *On the mechanism of dielectric relaxation in aqueous DNA solutions*, Biopolymers 31 (1991), 1171–1180.
190. Y. Murayama, Y. Sakamaki & M. Sano: *Elastic response of single DNA molecules exhibits a reentrant collapsing transition*, Physical Review Letters 90 (2003), 18102.
191. Y. Matsuzawa & K. Yoshikawa: *Change of the Higher Order Structure in a Giant DNA Induced by 4', 6-Diamidino-2-phenylindole as a Minor Groove Binder and Ethidium Bromide as an Intercalator*, Nucleosides and Nucleotides 13 (1994), 1415–1423.
192. A. Y. Grosberg, T. T. Nguyen & B. I. Shklovskii: *Colloquium: The physics of charge inversion in chemical and biological systems*, Reviews of Modern Physics 74 (2002), 329–345.
193. P.-Y. Hsiao & E. Luijten: *Salt-induced collapse and reexpansion of highly charged flexible polyelectrolytes*, Physical Review Letters 97 (2006), 148301.
194. B. L. Feringa: *A New Twist on Chirality*, Science 292 (2001), 2021–2022.
195. E. J. Ariëns & W. Soudijn (eds.): *Stereochemistry and biological activity of drugs*, (Blackwell Scientific Publ, Oxford, 1983).
196. M. Eichelbaum & A. S. Gross: *Stereochemical aspects of drug action and disposition*, Advances in Drug Research 28 (1996), 1–64.
197. B. Kasprzyk-Hordern: *Pharmacologically active compounds in the environment and their chirality*, Chemical Society Reviews 39 (2010), 4466–4503.
198. H. Murakami: *From Racemates to Single Enantiomers – Chiral Synthetic Drugs over the last 20 Years*, Topics in current chemistry 269 (2007), 273–299.
199. S. Ahuja (ed.): *Chiral separation methods for pharmaceutical and biotechnological products*, (Wiley, Hoboken, New Jersey, 2011).
200. G. Gübitz: *Chiral separations - Methods and protocols*, (Humana Press, Totowa (New Jersey), 2004).
201. G. Gübitz & M. G. Schmid: *Chiral separation by chromatographic and electromigration techniques. A Review*, Biopharmaceutics and Drug Disposition 22 (2001), 291–336.
202. G. K. E. Scriba: *Selected fundamental aspects of chiral electromigration techniques and their application to pharmaceutical and biomedical analysis*, Journal of Pharmaceutical and Biomedical Analysis 27 (2002), 373–399.
203. G. Subramanian: *Chiral separation techniques - A practical approach*, 3rd ed. (WILEY-VCH, Weinheim, 2007).
204. H. Wan & L. G. Blomberg: *Chiral separation of amino acids and peptides by capillary electrophoresis*, Journal of Chromatography A 875 (2000), 43–88.
205. P. G. de Gennes: *Mechanical selection of chiral crystals*, Europhysics Letters 46 (1999), 827–831.
206. M. Kostur: *Chiral separation in microflows*, Physical Review Letters 96 (2006), 14502.
207. P. Talkner, G.-L. Ingold & P. Hänggi: *Transport of flexible chiral objects in a uniform shear flow*, New Journal of Physics 14 (2012), 73006.

208. D. W. Howard, E. N. Lightfoot & J. O. Hirschfelder: *The hydrodynamic resolution of optical isomers*, *AIChE Journal* 22 (1976), 794–798.
209. M. Makino, L. Arai & M. Doi: *Shear Migration of Chiral Particle in Parallel-Disk*, *Journal of the Physical Society of Japan* 77 (2008), 64404.
210. P. Chen & C.-H. Chao: *Lift forces of screws in shear flows*, *Physics of Fluids* 19 (2007), 17108.
211. E. Kirkinis, A. Andreev & B. Spivak: *Electromagnetic propulsion and separation by chirality of nanoparticles in liquids*, *Physical Review E* 85 (2012), 16321.
212. N. Watari & R. Larson: *Shear-Induced Chiral Migration of Particles with Anisotropic Rigidity*, *Physical Review Letters* 102 (2009), 246001.
213. D. Speer, R. Eichhorn & P. Reimann: *Exploiting Lattice Potentials for Sorting Chiral Particles*, *Physical Review Letters* 105 (2010), 90602.
214. D. Speer: *Spontaneous Symmetry Breaking Transport: From Anomalous Response to Chiral Separation*, Dissertation, Bielefeld University, 2011.
215. R. Eichhorn: *Enantioseparation in microfluidic channels*, *Chemical Physics* 375 (2010), 568–577.
216. S. Meinhardt, J. Smiatek, R. Eichhorn & F. Schmid: *Separation of Chiral Particles in Micro- or Nanofluidic Channels*, *Physical Review Letters* 108 (2012), 214504.
217. Marcos, H. Fu, T. Powers & R. Stocker: *Separation of Microscale Chiral Objects by Shear Flow*, *Physical Review Letters* 102 (2009), 158103.
218. J. Hanes, J. L. Cleland & R. Langer: *New advances in microsphere-based single-dose vaccines*, *Advanced Drug Delivery Reviews* 28 (1997), 97–119.
219. S. C. Glotzer: *Some Assembly Required*, *Science* 306 (2004), 419–420.
220. N. Tétreault, H. Míguez & G. A. Ozin: *Silicon Inverse Opal - A Platform for Photonic Bandgap Research*, *Advanced Materials* 16 (2004), 1471–1476.
221. S. Gangwal, O. J. Cayre, M. Z. Bazant & O. D. Velev: *Induced-charge electrophoresis of metallodielectric particles*, *Physical Review Letters* 100 (2008), 58302.
222. Y. A. Kobelev: *Parameters of microparticles responsible for the monopole sound scattering in a liquid*, *Acoustical Physics* 50 (2004), 699–703.
223. S.-M. Yang, S.-H. Kim, J.-M. Lim & G.-R. Yi: *Synthesis and assembly of structured colloidal particles*, *Journal of Materials Chemistry* 18 (2008), 2177–2190.
224. A. B. D. Brown, C. G. Smith & A. R. Rennie: *Fabricating colloidal particles with photolithography and their interactions at an air-water interface*, *Physical Review E* 62 (2000), 951–960.
225. D. Dendukuri, K. Tsoi, T. A. Hatton & P. S. Doyle: *Controlled Synthesis of Nonspherical Microparticles Using Microfluidics*, *Langmuir* 21 (2005), 2113–2116.
226. D. Dendukuri, D. C. Pregibon, J. Collins, T. A. Hatton & P. S. Doyle: *Continuous-flow lithography for high-throughput microparticle synthesis*, *Nature Materials* 5 (2006), 365–369.
227. J. P. Rolland, B. W. Maynor, L. E. Euliss, A. E. Exner, G. M. Denison & J. M. DeSimone: *Direct fabrication and harvesting of monodisperse, shape-specific nanobiomaterials*, *Journal of the American Chemical Society* 127 (2005), 10096–10100.

228. S. Xu, Z. Nie, M. Seo, P. Lewis, E. Kumacheva, H. A. Stone, P. Garstecki, D. B. Weibel, I. Gitlin & G. M. Whitesides: *Generation of Monodisperse Particles by Using Microfluidics: Control over Size, Shape, and Composition*, *Angewandte Chemie International Edition* 44 (2005), 724–728.
229. S. Badaire, C. Cottin-Bizonne & A. D. Stroock: *Experimental Investigation of Selective Colloidal Interactions Controlled by Shape, Surface Roughness, and Steric Layers*, *Langmuir* 24 (2008), 11451–11463.
230. S. Badaire, C. Cottin-Bizonne, J. W. Woody, A. Yang & A. D. Stroock: *Shape Selectivity in the Assembly of Lithographically Designed Colloidal Particles*, *Journal of the American Chemical Society* 129 (2007), 40–41.
231. J. H. Moon, A. J. Kim, J. C. Crocker & S. Yang: *High-Throughput Synthesis of Anisotropic Colloids via Holographic Lithography*, *Advanced Materials* 19 (2007), 2508–2512.
232. A. del Campo & C. Greiner: *SU-8: a photoresist for high-aspect-ratio and 3D submicron lithography*, *Journal of Micromechanics and Microengineering* 17 (2007), R81-R95.
233. G. Kotzar, M. Freas, P. Abel, A. Fleischman, S. Roy, C. Zorman, J. M. Moran & J. Melzak: *Evaluation of MEMS materials of construction for implantable medical devices*, *Biomaterials* 23 (2002), 2737–2750.
234. E. Koukharenko, M. Kraft, G. J. Ensell & N. Hollinshead: *A comparative study of different thick photoresists for MEMS applications*, *Journal of Materials Science: Materials in Electronics* 16 (2005), 741–747.
235. P. M. Dentinger, W. M. Clift & S. H. Goods: *Removal of SU-8 photoresist for thick film applications*, *Microelectronic Engineering* 61–62 (2002), 993–1000.
236. S. Wegener: *Kontinuierliche Trennung chiraler Objekte ohne chemische Selektoren*, Bachelor-Thesis, Bielefeld University, 2010.
237. I. Roch, P. Bidaud, D. Collard & L. Buchaillot: *Fabrication and characterization of a SU-8 gripper actuated by SMA thin film*, *Journal of Micromechanics and Microengineering* 13 (2003), 330–336.
238. L. P. Faucheux & A. J. Libchaber: *Confined Brownian motion*, *Physical Review E* 49 (1994), 5158–5163.
239. F. J. Lorenz: *Enantioselektive Trennung in einem Mikrofluidiksystem mit asymmetrischem Flussprofil*, Bachelor Thesis, Bielefeld University, 2010.
240. A. Raudino & M. Pannuzzo: *Hydrodynamic-induced enantiomeric enrichment of self-assemblies: Role of the solid-liquid interface in chiral nucleation and seeding*, *Journal of Chemical Physics* 137 (2012), 134902.
241. D. K. Kondepudi, R. J. Kaufman & N. Singh: *Chiral Symmetry Breaking in Sodium Chlorate Crystallization*, *Science* 250 (1990), 975–976.
242. J. M. Ribò, J. Crusats, F. Sagués, J. Claret & R. Rubires: *Chiral Sign Induction by Vortices During the Formation of Mesophases in Stirred Solutions*, *Science* 292 (2001), 2063–2066.
243. J. Regtmeier, R. Eichhorn, L. Bogunovic, A. Ros & D. Anselmetti: *Dielectrophoretic Trapping and Polarizability of DNA: The Role of Spatial Conformation*, *Analytical Chemistry* 82 (2010), 7141–7149.

244. J. Wallbaum: *Partikeltracking in Videoaufnahmen eines Mikrofluidikchips*, Bachelor-Thesis, Bielefeld University, 2011.
245. D. Winston, B. M. Cord, B. Ming, D. C. Bell, W. F. DiNatale, L. A. Stern, A. E. Vladar, M. T. Postek, M. K. Mondol, J. K. W. Yang & K. K. Berggren: *Scanning-helium-ion-beam lithography with hydrogen silsesquioxane resist*, *Journal of Vacuum Science and Technology B* 27 (2009), 2702–2706.
246. S.-M. Lee, Y.-W. Jun, S.-N. Cho & J. Cheon: *Single-Crystalline Star-Shaped Nanocrystals and Their Evolution: Programming the Geometry of Nano-Building Blocks*, *Journal of the American Chemical Society* 124 (2002), 11244–11245.
247. T. Mokari, E. Rothenberg, I. Popov, R. Costi & U. Banin: *Selective Growth of Metal Tips onto Semiconductor Quantum Rods and Tetrapods*, *Science* 304 (2004), 1787–1790.
248. P. D. Cozzoli & L. Manna: *Asymmetric nanoparticles: Tips on growing nanocrystals*, *Nature Materials* 4 (2005), 801–802.
249. S. Kinge, M. Crego-Calama & D. N. Reinhoudt: *Self-Assembling Nanoparticles at Surfaces and Interfaces*, *ChemPhysChem* 9 (2008), 20–42.
250. C. Vosskötter: *Erzeugung dreidimensionaler asymmetrischer Flussprofile in Mikrofluidikkanälen mittels eines zwei-Komponenten Chipsystems*, Bachelorthesis, Bielefeld University, 2011.
251. M. D. Abramoff, P. J. Magalhaes & S. J. Ram: *Image Processing with ImageJ*, *Biophotonics International* 11 (2004), 36–42.

7 ACKNOWLEDGEMENTS

Eine große Zahl von Personen hat zum Gelingen meiner Arbeit beigetragen und mich tatkräftig unterstützt. Zunächst möchte ich mich bei Herrn Prof. Dario Anselmetti für die freundliche Aufnahme in seine Arbeitsgruppe "Experimentelle Biophysik und angewandte Nanowissenschaften" sowie sein Gutachten für die vorliegende Arbeit und die sehr interessanten Vorlesungen über Biophysik bedanken. Die zahlreichen Diskussionen mit ihm waren sehr hilfreich für mich und haben meine Projekte stets gut voran gebracht. Auch war er als Sprecher des Sonderforschungsbereichs 613 maßgeblich für die erfolgreiche Finanzierung der Projekte verantwortlich. Ich freue mich sehr auf die weitere bevorstehende Zusammenarbeit.

Die enge und leistungsstarke Kooperation zwischen experimentell und theoretisch arbeitenden Wissenschaftlern im Rahmen unseres SFB Teilprojektes wurde besonders durch vier Kollegen voran gebracht: Prof. Peter Reimann möchte ich sehr für sein Gutachten zu meiner Arbeit danken. Die zahlreichen Diskussionen mit ihm waren für mich sehr lehrreich und halfen mir bei der Interpretation meiner Daten. Prof. Ralf Eichhorn leistete wichtige Modellierungs- und Simulationsarbeit für das Ratschenprojekt, die automatisierte Polarisationsmessung und die chirale Trennung mit der strukturierten Seitenwand. Während meiner Aufenthalte am NORDITA in Stockholm und der zahlreichen Telefonate nahm er sich immer viel Zeit für mich, um Simulationen und experimentelle Resultate zu diskutieren. Ich möchte ihm auch für die Einladung nach Mariehamn danken, wo ich einer recht außergewöhnlichen Konferenz beiwohnen durfte und für seine Durchsicht meiner Arbeit. Marc Fliedner entwickelte die Simulationssoftware für die chirale Trennung mittels Pfoftenarray und leistete wichtige theoretische Vorarbeiten für dieses Projekt. Auch bei ihm möchte ich mich für die zahlreichen Diskussionen bedanken und denke, dass wir viel voneinander gelernt haben. Mein ganz besonderer Dank gilt Dr. Jan Regtmeier, meinem ehemaligen Teilprojektleiter. Er war es, der mich für dieses faszinierende Arbeitsgebiet der Mikrofluidik begeistert hat. Ich freue mich sehr über die langjährige äußerst produktive und angenehme Zusammenarbeit und seine vorbildliche Betreuung meiner Arbeit bis zu seiner beruflichen Umorientierung.

Ich möchte mich außerdem bei allen Mitgliedern unserer Arbeitsgruppe für das freundliche Arbeitsklima bedanken. Insbesondere sind hier Christoph Pelargus, Gabi Krome, Helene Schellenberg und Karin Lacey, die für reibungslos funktionierende Labortechnik und unkomplizierte Verwaltung gesorgt haben, zu nennen. Christoph danke ich ebenfalls für das

wunderbare Foto auf dem Titelblatt. Weiterhin gilt mein besonderer Dank meinen Bürokollegen Dominik Greif, Lukas Galla und Carina Vosskötter für die angenehme Zusammenarbeit und die ausgezeichnete stetige Versorgung mit Knabbereien.

Die finanziellen Mittel zur Realisierung der Projekte wurden von der Deutschen Forschungsgemeinschaft im Rahmen des Teilprojektes D2 des Sonderforschungsbereichs 613 bereitgestellt. Auch hierfür möchte ich mich herzlich sowohl bei der DFG als auch bei den Projektverantwortlichen und Antragstellern bedanken.

Ein besonderer Dank gilt meinen Eltern Marion und Nikola Bogunovic. Sie waren es, die mir im Alter von sechs Jahren meinen ersten Elektronikbaukasten geschenkt haben und mein Interesse an der Naturwissenschaft geweckt haben. Sie haben mich seitdem konsequent in meinem Interessenschwerpunkt unterstützt und mir das Studium der Physik ermöglicht. Dafür bin ich ihnen zutiefst dankbar. Außerdem möchte ich mich bei Ditmar Kiel, Ralf Prüßmeier und Dr. Bernd-Heinrich Brand, meinen Physik- und Chemielehrern, für die solide und motivierende Ausbildung, die sie mir haben zukommen lassen, bedanken.

Der letzte und damit wichtigste Absatz in dieser Danksagung gebührt der bedeutendsten Person in meinem Leben, meiner lieben Freundin Tabea Pirl. Sie war zur Stelle und fand stets die richtigen motivierenden Worte in schwierigen Arbeitsabschnitten und war immer verständnisvoll und hat sogar oft Kaffee gekocht, wenn die Arbeit mal wieder etwas länger gedauert hat.

APPENDIX

A1 CONSTRUCTION OF A MICROFLUIDIC PRECISION PUMP

The generation of hydrodynamic flows in microfluidic chips requires a highly precise pneumatic pumping device, which was developed within the framework of this thesis (see Figure 64). The requirements are non-pulsating operation, low cost, and very fine control of the applied pressure. Therefore, the established peristaltic pumps were waived.

The self-developed system contains of two independently working control units and can therefore operate microfluidic chips with up to four reservoirs. The two proportional pressure regulators Airfit Tecno PRE-U are the central components, attenuating the inlet pressure of $p_0 = 1.7$ bar nitrogen to values between 0 and 200 mbar proportionally to an applied voltage (see Figure 64 B). They are particularly characterized by low response sensitivities (see Table 15).

Using the pressure regulators, the actual applied pressures p_1 and p_2 can be measured as well. Connected upstream, two digital locking valves interrupt the nitrogen stream in an exceptional case (see Figure 64 A). The flow direction inside the micro channels can be chosen using two arrays consisting of two MHA2-MS1H3/2G-2-k digital valves in each array (see Figure 64 C). Both digital valves are coupled logically inversely resulting in one of letting the nitrogen pass, while the other one blocks the stream and connects the tube to the environmental atmosphere, causing de-aeration.

The whole system is controlled by a self-developed LabView program, which can either be controlled manually with a joystick or in an automated fashion by programming certain

Table 15: Characteristics of the used pressure regulators Airfit Tecno PRE-U according to the technical datasheet.

Parameter	Value	Unit
Inlet pressure	1,5-2,5	bar
Outlet pressure	0-0,2	bar
Nominal flow	200	l/min
Maximum flow	350	l/min
Hysteresis	<0,5	%
Repeatability	<0,5	%
Response sensitivity	<0,5	%
Linearity	<0,5	%

sequences in advance. The exceptional case status where the valves A close can be triggered by pressing joystick button 1. The tubes 1.A, 1.B, 2.A, and 2B are connected to the microfluidic chip using Festo tube connectors screwed into the acrylic glass block that holds the microfluidic chip (see Figure 65). Hence, an air tight macro-micro-interface with extraordinary stability is obtained.

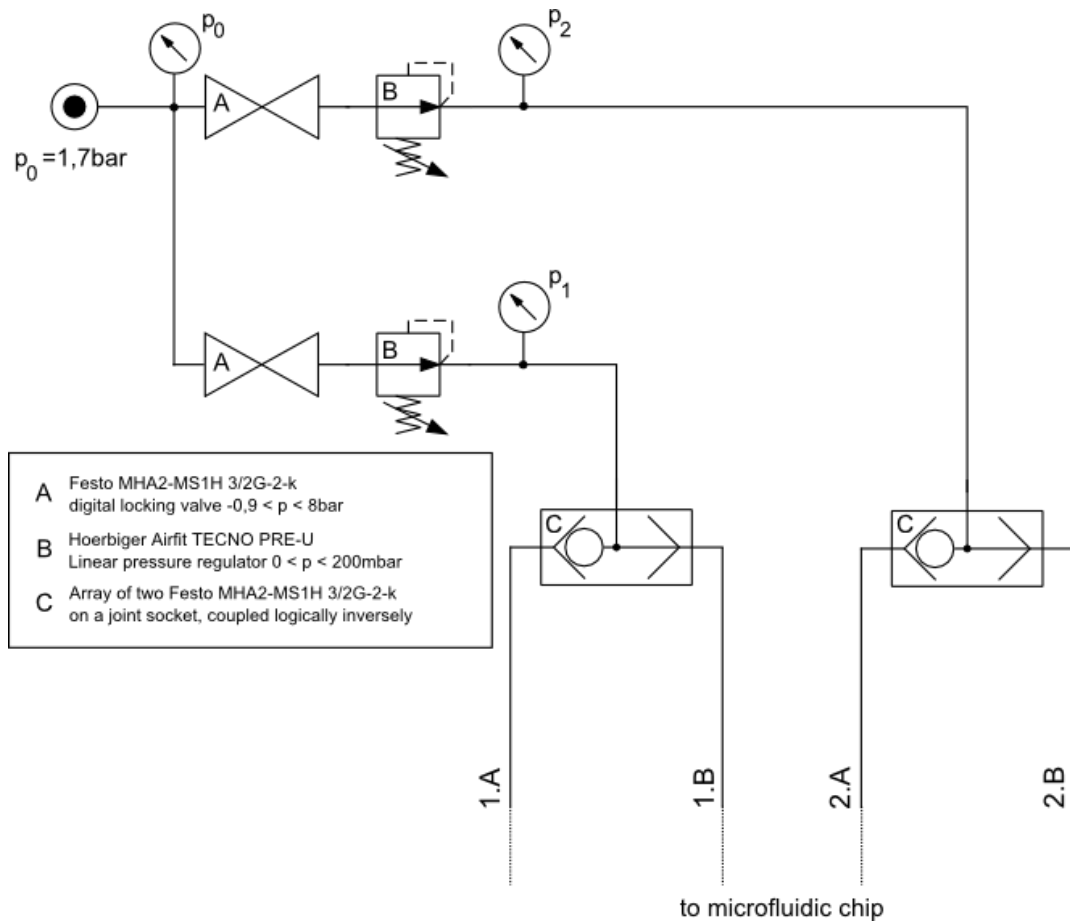


Figure 64: Schematic of the constructed precise pumping system for microfluidic devices. Liquid in two separate channels can be driven at the same time pneumatically. Central components (B) are two electronic linear pressure regulators Airfit Tecno PRE-U which are operated with an inlet pressure of $p_0 = 1.7 \text{ bar}$ from a nitrogen bottle. Two digital locking valves with magnetic triggers stop the nitrogen supply in case of an emergency (A). Depending on the voltages applied to the regulators, pressures between 0 and 200 mbar (p_1, p_2) can be generated, measured and controlled at the same time. Two arrays with two Festo MHA2-MS1H3/2G-2-k digital valves (C) in each array control the flow direction by directing the nitrogen stream to one of the outlets (e.g. 1.A) while the other outlet (1.B) is connected to the environmental pressure due to the logically inverse coupling of the valves.

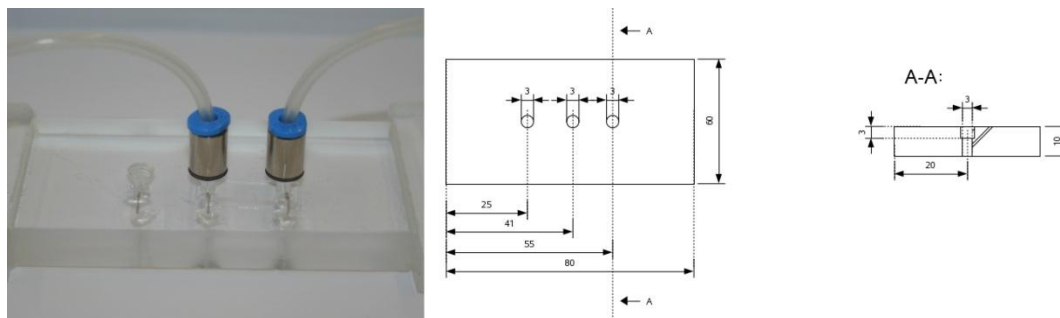


Figure 65: Picture and design drawing of the pump to microchip interface. Chip sticks due to adhesion forces onto the lower side of an acrylic glass block which contains holes placed congruently with the reservoirs. Using Festo tube connectors which are screwed into the holes, an air tight and very stable connection between the tubing of the pump and the microfluidic chip is created. For exploiting electrical driving techniques, platinum wires have been integrated into the chip holder as well. All measures in mm.

A2 SOURCECODES

Software packages were developed to analyze experimental data and operate the laboratory setup. This section lists the corresponding source codes.

A2.1 EVALUATION OF MEAN TRAPPING TIMES

The automated quantification of single molecule polarizabilities is based on an analysis of a time series of fluorescence microscopy images as described in paragraph 4.2.1. The analysis operation is controlled by the perl script 'dna.pl' which controls image analysis via ImageJ²⁵¹ and evaluates the resulting numerical data via the C-program 'bootstrap.c' and readin.h. All sourcecodes are listed below. The evaluation routine is started by launching dna.pl and providing the path to the fluorescence image data.

dna.pl

```
#!/usr/bin/perl -w
###
#Definition of path to ImageJ. Please change if this is wrong.
$ijpath="/home/user/dep";
###

#Prints welcome message and reads path to DNA fluorescence data.

print "\n\nScript zur Auswertung von DNA-Migrationsdaten.\n";
print "Dieses Script geht davon aus, dass sämtliche Messpunkte\nin je einem Ordner in einem
Mutterpfad liegen. Bitte jetzt diesen Mutterpfad eingeben:\n\n";
print "\t >>";
$mutterpfad = <STDIN>;
chomp ($mutterpfad);
@verzeichnis = &getDirEntry($mutterpfad);
$len=@verzeichnis;
```

```

chdir ($mutterpfad);
print "Es wurden $len Datenpunkte (Verzeichnisse) gefunden.\n\n";
print "-----\n";

#Generates ImageJ macro $ijmacro and writes it into every image folder. Launches bootstrapper
and prints results

for ($i=1;$i<=$len;$i++)
{
    $name=shift(@verzeichnis);
    chomp ($name);
    $path= $mutterpfad."/".$name;
    chdir ($path);
    $macro= $path.'/ep-macro.txt';

    $ijmacro="run(\"Clear Results\");
    dir = \"\".$path.\"\"
    list = getFileList(dir);
    run(\"Image Sequence...\", \"open=.$path./img_0001.TIF number=1000
starting=1 increment=1 scale=100 file=\");
    makeRectangle(72, 1, 13, 125);
    run(\"Set Measurements...\", \" mean redirect=None decimal=6\");
    for (i=0; i<list.length; i++)
    {
        run(\"Measure\");
        run(\"Next Slice [>]\");
    }
    run(\"Input/Output...\", \"jpeg=75 file=.dat\");
    saveAs(\"Measurements\", \"\".$path.\".dat\");
    close();
    run(\"Window Closer\");
    run(\"Quit\");";

    &writeFile($ijmacro,$macro);
    chdir ($ijpath);
    system("./jre/bin/java -mx256m -cp ij.jar ij.ImageJ $path/ep-macro.txt");
    system("more +2 $path.dat > $path.dat.temp");
    $ergebnis=`bootstrap $path.dat.temp`;
    print ("\n\nGewichteter Mittelwert beträgt: \n\n$ergebnis\n\n");
    @results[$i]=$ergebnis;
}

print "\n#####\n";
print "\nErgebnisse\n";
print "\n#####\n";
print "Directory\t\t\tGewichtetes Mittel \t Fehler \t Nulllinie\n";

for ($i=1;$i<=$len;$i++)
{
    print @results[$i];
    #&writeFile(@results[$i], $mutterpfad.'/results.dat');
}

print "\n-----\n";
exit (0);

# A subroutine to write a file with given content

sub writeFile
{
    my ($data,$file) = @_;
    open (WRITE,">$file") || die "Kann nicht in $file schreiben.\n\n";
    print WRITE $data;
    close WRITE;
}

# A subroutine to read the content of a given directory

sub getDirEntry
{
    my $dirToDo = shift || '';
    my $temp;
    my @dirEntry ;

```

```

opendir(DIRHANDLE,"$dirToDo") || die "\n\n\n$dirToDo gibt es garnicht!\n\n";
foreach $temp (sort readdir(DIRHANDLE))
{
    if(!grep /\^\.(*)?$/, $temp)
    {
        push(@dirEntry, "$temp");
    }
}
closedir(DIRHANDLE);
return @dirEntry;
}

```

Bootstrap.c

```

#include <stdio.h>
#include <math.h>
#include <sys/types.h>
#include <time.h>
#include <stdlib.h>
#include "readin.h"
#define NMAX 20000

int main(int argc, char **argv )
{
//Definition of variables

    double xin[NMAX] , yin[NMAX];
    double xeval[NMAX], yeval [NMAX];
    double max=0,mittelwert[NMAX], stdawsum=0,stdaw=0,var=0;
    int p=66,n=0;
    int rnd=0,i=0,end=0,ndata=0;
    double mean=0,sumx=0,sum=0;
    double sum_mid=0,nulllinie=0;

//-----

    srand( (unsigned)time( NULL ) );
    ndata=readin(argv[1],xin,yin)-1;
    max=floor(p*ndata/100);
    end=max;

//Calculation of mean value in first 60 frames and generation of baseline to subtract

    sum_mid=0;
    for (i=1;i<=60;i++)
    {
        sum_mid=sum_mid+yin[i];
    }

    nulllinie=sum_mid/60;

//Execution of baseline correction

    for (i=1;i<=ndata;i++)
    {
        yin[i] = yin[i] - nulllinie;
    }

//Calculation of weighted mean value

```

```

for (i=1;i<=ndata;i++)
{
sum=sum+(yin[i]*xin[i]);
sumx=sumx+yin[i];
}
mean=sum/sumx;

//Generation of randomly bootstrapped stacks and calculation of mean values

for (n=1; n<=10000; n++)
{
for (i=1;i<=end;i++)
{
rnd=1+(rand() % (ndata));
xeval[i]=xin[rnd];
yeval[i]=yin[rnd];
}
sum=0;
sumx=0;
for (i=1;i<=end;i++)
{
sum=sum+(xeval[i]*yeval[i]);
sumx=sumx+yeval[i];
}
mittelwert[n]=sum/sumx;
}

//The standard deviation of those values from mean is the final statistical error

for (n=1;n<=10000; n++)
{
stdawsum= stdawsum+pow(abs(mittelwert[n]-mean),2);
}

var=stdawsum/10000;
stdaw=sqrt(var);

printf("%s\t%f\t%f\t%f\n",argv[1],mean,stdaw,nulllinie);
return(0);
}

```

readin.h

```

#include <stdlib.h>
/*****
int readin(char *fname, double x[], double y[])
-----
Reads data pairs x[i] y[i] (i=0...(ndata-1)) from fname. The function returns the number of
aquired data pairs.
*****/

int NMAX=10000;
int readin(char *fname, double x[], double y[])
{
FILE *fin;
int i=1,ndata;
fin = fopen(fname,"r");
do
{
if (i>NMAX)
{
printf("Number of Input lines > NMAX.\n please redefine NMAX in the c-file an in
readin.h\n");
exit(1);
}
}

```

```

        if (fscanf(fin,"%le %le",&x[i],&y[i]) == 2)
            i++;
    }
    while(!feof(fin));
    ndata=i;
    fclose(fin);
    return(ndata);
}

```

A2.2 DSP SOFTWARE

The following software (kindly developed by C. Pelargus) controls the Adwin Gold II digital signal processor and implements a signal generator and the offset feedback loop.

```

#include ADwinGoldII.inc
Dim n, m,
freq,t,e,esum,esummittel,esummittelold,firstcal,delayP,TimeOld,Time2,Time32,diff2,sinus_out_2
,rate,e2 as long
Dim analog_in, analog_in_2,sinus_out,amp,ampDig,w,diff,ampoff,Time,
integriert,efloat,ampDigtmp,ampofftmp,Timetmp as float
Dim multi16, multi24 as float
Dim Data_1[3000],Data_2[3000],Data_3[3000],Data_4[3000] as float

#define pi 3.141592654
#define offset16 32768 '16bit -> 3.051757813E-4
#define offset24 8388608 '24bit -> 1.192092896E-6
#define procfreq 300E+6 'Prozessortakt in Hz --> 300MHz = 3.333333333E-9s

Init:
    delayP = 1500
    Processdelay=delayP ' = Abtastgeschwindigkeit Bsp: 3000*3.3333333E-9 = 10µs --> 100kHz !!
    max 100kHz wegen AD (stabil)!!
    m = 1
    t = 0
    multi16 = 20/65536 '20 -> Messbereich +/-10V
    multi24 = 20/16777216
    e = 0
    diff = 1
    diff2 = 1
    firstcal=0
    esum = 0
    esummittel= 0
    esummittelold=0
    integriert=0
    e2=0
    efloat=0
    ampDigtmp=0
    '-----Eingabe-----
    FPar_19 = 100 'Anzahl der Abtastwerte pro Periode; Dauer einer Periode =
    300E+6/Processdelay/FPar_19 --> 1/DeP=Frequenz in Hz
    FPar_21=0 'Amplitude in Volt
    FPar_22=0 'DC Offset in Volt
    FPar_24=0 'Störampplitude in Volt der Symetrie
    FPar_25=0 'Störampplitude in Volt der Amplitude (wird nicht kompensiert!)
    Par_6 = 1 '1= mit Analogeingang und Regelung --> Processdelay max 2000 --> 150kHz 0 =
    PDmax 600 --> 500kHz
    Par_3=1 '1 = Integration über eine Periode
    FPar_12=0 'Symetriedifferenz durch Integration über eine Periode
    Par_18=10 'Anzahl der Werte die gemittelt werden für Symetrieregung
    Par_60=0 'DIO setzen 1= true
    Par_66=0
    Par_67=0
    Par_68=0
    Par_69=0
    Par_70=0
    Par_71=0
    Par_72=0
    Par_73=0

```

```

Par_74=0
Par_75=0
Par_76=0
Par_77=0
'-----
SET_MUX1 (00 000b)      'Mux 1: Kanal und Verstärkung 1 setzen ; Einschwingzeit gespart max
2µs

CONF_DIO(1100b)        'setzt DIO 0-15 als Eingänge und 16-31 als Ausgänge
DIGOUT_LONG(0b)

event:
'DIO- Ausgänge setzen Par_66-77 --> 12 DIO (16-28) --> Pin 19-7 DGND 37-25
if ((t=Time*2) and (Par_60=1))then
  DIGOUT(16,Par_66)
  DIGOUT(17,Par_67)
  DIGOUT(18,Par_68)
  DIGOUT(19,Par_69)
  DIGOUT(20,Par_70)
  DIGOUT(21,Par_71)
  DIGOUT(22,Par_72)
  DIGOUT(23,Par_73)
  DIGOUT(24,Par_74)
  DIGOUT(25,Par_75)
  DIGOUT(26,Par_76)
  DIGOUT(27,Par_77)
endif

Time = FPar_19/2 ' (procfreq/FPar_19/delayP)/2 '1000/2 'FPar_19/2 '--> Bandbreite =
Abtastgeschwindigkeit x Periodendauer T
FPar_18=procfreq/FPar_19/Processdelay      'Frequenz einer Periode in Hz
FPar_20 = Time      'Abtastwerte einer Periode
ampDig = FPar_21/multi16
ampoff = FPar_22/multi16
Par_1 = m          'Data_1 Analog in zähler
Par_2 = t          'Zähler für eine Periode der Sinus- kurve
Par_4= diff        ' Differenzzähler für Symetrieabweichung: e
Par_8=esummittel
Par_13=esummittelold
FPar_6=Processdelay*3.3333333*10^-6 '--> Abtastrate in ms6

'-----generation of sine function-----

if (Par_6=1)then      'Bei Regler ein:
  if (t=0) then      'Lässt Änderungen der Amplitude, Offset und Frequenz erst nach Ablauf
einer Periode zu
    w = pi/Time
    sinus_out = (ampDig+FPar_25/multi16)*(Sin(w*t))+offset16 -esummittel/2-esummittelold/2
+ampoff +FPar_24/multi16
    ampDigtmp=ampDig
    ampofftmp=ampoff
    Timetmp=Time
  else
    w = pi/Timetmp
    sinus_out = (ampDigtmp+FPar_25/multi16)*(Sin(w*t))+offset16 -esummittel/2-
esummittelold/2 +ampofftmp +FPar_24/multi16
  endif
endif

'Regler aus nur Frequenzgenerator mit offset
if (Par_6=0)then sinus_out = (ampDig+FPar_25/multi16)*(Sin(w*t))+offset16 +ampoff

'-----DA-Output-----

sinus_out_2=sinus_out +0.5
FPar_5 = sinus_out
Par_5 = sinus_out_2
DAC(1,(sinus_out_2))

'-----AD--Input-----
if (Par_6=1)then      'Analog auslesen und Regeln = 1

```

```

Start_Conv(1)          'Start AD-Wandlung ADC1
Wait_EOC(1)           'Wandlungsende des ADC1 abwarten
analog_in = Read_ADC(1)

' analog_in=adc(1)
Data_1[m] = (analog_in-offset16) * multi16      '(Lese AD Wandler - offset)*bit to volt
Data_3[m] = (analog_in)

'-----symmetrische-Abweichung-pos-neg-Flanke-----

Time2=(Time/2)+0.5
FPar_30=Time2
Time32=(Time*3/2)+0.5
FPar_31=Time32

if (Par_3=0)then
  if (t=(Time2)) then
    Par_10=(Data_3[m]-offset16) '* multi16
  endif

  if (t=(Time32)) then
    Par_11=(Data_3[m]- offset16) '* multi16
  endif
  e=Par_10+Par_11-2*ampoff
endif

if (Par_3=1)then
  integriert =(Data_3[m]- offset16)+integriert
  if (t=Time*2-1)then
    efloat = (integriert/(Time*2))
    if (efloat<0)then efloat=efloat-0.5
    if (efloat>0)then efloat=efloat+0.5
    e2 = efloat
    e = e2-ampoff
    integriert=0
  endif
endif

FPar_12=efloat-ampoff
Par_12=e
Data_2[diff2]=e
Data_4[diff2]=e*multi16*1000 'im mV

'-----

FPar_1=analog_in
inc m

if (diff>Par_18) then
  esummittelold=esummittel+esummittelold
  if ((esum/(diff-1))<(0))then esummittel = (esum/(diff-1))-0.5
  if ((esum/(diff-1))>(0))then esummittel = (esum/(diff-1))+0.5
  FPar_9 = esummittel
  esum=0
  diff=1
endif

if (m=3000) then m=1
  if (diff2=3000) then diff2=1
endif

inc t
if (t>=Time*2)then
  esum=e+esum
  t=0
  inc diff
  inc diff2
endif

endif

```

A3 PUBLICATIONS AND CONFERENCE PARTICIPATIONS

A3.1 PEER REVIEWED PUBLICATIONS AND MANUSCRIPTS

1. J. Regtmeier, R. Eichhorn, **L. Bogunovic**, A. Ros, & D. Anselmetti: *Dielectrophoretic Trapping and Polarizability of DNA: The Role of Spatial Conformation*, *Analytical Chemistry* 82 (2010), 7141-7149
2. **L. Bogunovic**, D. Anselmetti & J. Regtmeier: *Photolithographic fabrication of arbitrarily shaped SU-8 microparticles without sacrificial release layers*, *Journal of Micromechanics and Microengineering* 21 (2011), 027003
3. J. Regtmeier, R. Eichhorn, M. Everwand, **L. Bogunovic** & D. Anselmetti: *Electrodeless Dielectrophoresis for bioanalysis: theory, devices and applications*, *Electrophoresis* 32 (2011), 2253-2273 (invited review article)
4. **L. Bogunovic**, R. Eichhorn, J. Regtmeier, D. Anselmetti & P. Reimann: *Particle sorting by a structured microfluidic ratchet device with tunable selectivity: Theory and Experiment*, *Soft Matter* 8 (2012), 3900-3907
5. **L. Bogunovic**, M. Fliedner, R. Eichhorn, S. Wegener, D. Anselmetti, J. Regtmeier & P. Reimann: *Chiral particle separation by a nonchiral micro-lattice*, *Physical Review Letters* 109 (2012), 100603
6. N. Bogunovic, D. Horstkotte, L. Faber, **L. Bogunovic**, D. Kececioglu, C. Piper, C. Prinz & F. van Buuren: *Effective Valve Opening Area in the Detection of Dysfunctional Aortic Valve Prostheses: A Differentiated Statistical Analysis of This Parameter Including the Introduction of Minimal Expected Normal Values as Borderline to Dysfunctional Stenotic Prostheses*, *Echocardiography* 29 (2012), 713-719
7. **L. Bogunovic**, C. Vosskötter & D. Anselmetti: *Fabrication of microfluidic channels with differently modified surfaces via a two component approach*, in preparation
8. **L. Bogunovic**, F. Lorenz, R. Eichhorn, D. Anselmetti, J. Regtmeier & P. Reimann: *Enantioselective Separation of Microparticles in a sawtooth microchannel*, in preparation
9. J. Regtmeier, S. Gerkens, M. Everwand, **L. Bogunovic**, R. Eichhorn & D. Anselmetti: *Valveless pumping with a single actuated PDMS membrane*, in preparation

A3.2 PUBLISHED CONFERENCE PROCEEDINGS

1. **L. Bogunovic**, R. Eichhorn, P. Reimann, J. Regtmeier & D. Anselmetti: *Freely Selectable Direction of Separation for Different Particle Species with a New Microfluidic Separation Device*, *Proceedings of the 14th international conference on miniaturized systems for chemistry and life sciences (MicroTAS)*, 3.10.2010 – 7.10.2010, Groningen, The Netherlands
2. **L. Bogunovic**, R. Eichhorn, S. Wegener, F. Lorenz, J. Regtmeier & D. Anselmetti: *Towards selectorfree separation of chiral molecules: Enantioselective Separation of Microparticles in a microfluidic device*, *Proceedings of the 15th international conference on miniaturized systems for chemistry and life sciences (MicroTAS)*, 2.10.2011 – 6.10.2011, Seattle, Washington, USA

A3.3 Contributions to conferences

- [Poster] **L. Bogunovic**, J. Regtmeier, R. Eichhorn, A. Ros & D. Anselmetti: *DNA-polarizability and separation via electrodeless dielectrophoresis*, German Biophysical Society Meeting, 29.9.2008 – 1.10.2008, Berlin.
- [Poster] **L. Bogunovic**, J. Regtmeier, R. Eichhorn, A. Ros & D. Anselmetti: *Microfluidic device for polarizability-measurements and fast DNA-separation on a single molecule level*, ScienceFair, 13.11.2008, Bielefeld.
- [Talk] **L. Bogunovic**, J. Regtmeier, R. Eichhorn, A. Ros & D. Anselmetti: *A microfluidic device for polarizability-quantification and fast DNA-separation on single molecule scales*, Frühjahrstagung der Deutschen Physikalischen Gesellschaft, 23.3.2009 – 27.3.2009, Dresden
- [Talk] **L. Bogunovic**, J. Regtmeier, R. Eichhorn, A. Ros & D. Anselmetti: *A Versatile Microfluidic Device for the Analysis of Single DNA Polarization: Access to Geometrical and Electrical Scaling Laws*, Workshop des Sonderforschungsbereichs 613, 8.10.2009 – 9.10.2009, Bad Salzdetfurth
- [Talk] **L. Bogunovic**, J. Regtmeier, R. Eichhorn, A. Ros & D. Anselmetti: *A versatile microfluidic device for the analysis of single DNA polarization: Access to geometrical and electrical scaling laws*, Nanobiotech Montreux 2009, 16.11.2009 – 18.11.2009, Montreux, Switzerland
- [Poster] **L. Bogunovic**, J. Regtmeier & D. Anselmetti: *A hazzardfree fabrication process for arbitrarily shaped microparticles*, Frühjahrstagung der Deutschen Physikalischen Gesellschaft, 21.3.2009 – 26.3.2009, Regensburg
- [Poster] **L. Bogunovic**, R. Eichhorn, P. Reimann, J. Regtmeier & D. Anselmetti: *Freely selectable direction of separation for different particle species with a new microfluidic separation device*, The 14th international conference on miniaturized systems for chemistry and life sciences (MicroTAS), 3.10.2010 – 7.10.2010, Groningen, The Netherlands
- [Talk] **L. Bogunovic**, R. Eichhorn, P. Reimann, J. Regtmeier & D. Anselmetti: *A Microfluidic ratchet device for the controlled and tuneable separation of microparticles*, Nanobiotech Montreux 2010, 15.11.2010-17.11.2010, Montreux, Switzerland
- [Talk] **L. Bogunovic**, M. Fliedner, S. Wegener, P. Reimann, D. Anselmetti & J. Regtmeier: *Chiral Separation in a microfluidic chip without chemical selectors*, Jahreshauptversammlung des Sonderforschungsbereichs 613, 10.2.2011, Bielefeld
- [Poster] **L. Bogunovic**, M. Fliedner, S. Wegener, P. Reimann, D. Anselmetti & J. Regtmeier: *Continuous chiral separation in a post array*, Frühjahrstagung der Deutschen Physikalischen Gesellschaft, 13.3.2011 – 18.3.2011, Dresden
- [Talk] F. J. Lorenz, **L. Bogunovic**, R. Eichhorn, D. Anselmetti & J. Regtmeier: *Enantioselective separation by an asymmetric flow profile*, Frühjahrstagung der Deutschen Physikalischen Gesellschaft, 13.3.2011 – 18.3.2011, Dresden
- [Talk] **L. Bogunovic**, R. Eichhorn, J. Regtmeier, D. Anselmetti & P. Reimann: *A microfluidic ratchet device for the controlled and tuneable separation of microparticles*, Frühjahrstagung der Deutschen Physikalischen Gesellschaft, 13.3.2011 – 18.3.2011, Dresden

- [Talk] **L. Bogunovic**, M. Everwand, J. Regtmeier, R. Eichhorn, R. Reimann & D. Anselmetti: *Microfluidic tools for DNA analysis, manipulation and separation*, Statistical Mechanics and Computation of DNA-Self Assembly, 25.5.2011-28.5.2011, Mariehamn, Finland
- [Talk] **L. Bogunovic**: *Das Chemielabor in der Hosentasche – Science oder ScienceFiction?*, Tag der Naturwissenschaften am Immanuel-Kant-Gymnasium, 14.7.2011, Bad Oeynhausen
- [Talk] M. Viefhues, **L. Bogunovic**, R. Eichhorn, P. Reimann & D. Anselmetti: *New non-equilibrium migration mechanisms for microfluidic (bio)analysis*, Workshop des Sonderforschungsbereichs 613, 27.9.2011 – 28.9.2011, Loccum
- [Poster] **L. Bogunovic**, M. Viefhues, R. Eichhorn, P. Reimann & D. Anselmetti: *New migration mechanisms and separation concepts for biomolecules in structured microfluidic systems*, Workshop des Sonderforschungsbereichs 613, 27.9.2011 – 28.9.2011, Loccum
- [Poster] **L. Bogunovic**, R. Eichhorn, S. Wegener, F. Lorenz, J. Regtmeier & D. Anselmetti: *Towards selectorfree separation of chiral molecules: Enantioselective Separation of Microparticles in a microfluidic device*, The 15th international conference on miniaturized systems for chemistry and life sciences (MicroTAS), 2.10.2011 – 6.10.2011, Seattle, Washington, USA
- [Poster] **L. Bogunovic**, R. Eichhorn, S. Wegener, F. J. Lorenz, J. Regtmeier & D. Anselmetti: *Enantioselective Separation of chiral microparticles in a microfluidic device*, Nanobiotech Montreux 2011, 14.11.2011 – 16.11.2011, Montreux, Switzerland
- [Poster] **L. Bogunovic**, M. Fliedner, S. Wegener, F. J. Lorenz, R. Eichhorn, J. Regtmeier, P. Reimann & D. Anselmetti: *Continuous chiral separation in a microfluidic system*, Jahrestagung der Deutschen Gesellschaft für Biophysik, 23.9. – 26.9.2012, Göttingen

A4 CURRICULUM VITAE

Lukas Bogunovic, born August 4th 1984 in Herford, Germany

School Education

- 08/1991 – 06/1995 **Wichern Elementary School, Bad Oeynhausen**
- 08/1995 – 06/2004 **Immanuel-Kant-Gymnasium, Bad Oeynhausen**
Degree: Abitur with commendation by the German Physical Society (DPG)

Civil Service

- 06/2004-02/2005 **Heart- and Diabetes Center of North Rhine Westphalia, Bad Oeynhausen**
Hospital Informatics Department

Studies

- 04/2005 – 04/2007 **Bachelor-Studies in physics at Bielefeld University**
Degree: Bachelor of Science (B.Sc.)
- 04/2007 – 10/2007 **Bachelor-Thesis at Bielefeld University**
Chair of Experimental Biophysics and Applied Nanoscience
Prof. D. Anselmetti
- 10/2007 – 07/2008 **Master-Studies in physics at Bielefeld University**
Degree: Master of Science (M.Sc.)
- 01/2008 – 04/2009 **Master-thesis at Bielefeld University**
Chair of Experimental Biophysics and Applied Nanoscience
Prof. D. Anselmetti

PhD Studies

- Since 05/2009 **PhD studies in experimental physics at Bielefeld University**

Chair of Experimental Biophysics and Applied Nanoscience
Prof. D. Anselmetti

Awarded with the “**Young Investigator Award**” sponsored by the collaborative research center SFB613 and the “**Transferpreis für herausragenden Praxisbezug**” sponsored by Bielefeld University and Stadtwerke Bielefeld GmbH